Rodrigo Freitas

Molecular simulation: methods and applications

Simulações moleculares: métodos e aplicações

Campinas
2013

Universidade Estadual de Campinas
Instituto de Física Gleb Wataghin

Rodrigo Freitas

Molecular simulation: methods and applications

Advisor: Dr. Maurice de Koning

Simulações moleculares: métodos e aplicações

Dissertação de Mestrado apresentada ao Programa de Pós-Graduação em Física do Institudo de Física *Gleb Wataghin* da Universidade Estadual de Campinas para a obtenção do título de Mestre em Física.

Master's degree dissertation presented to the Physics Post-graduation Program of the *Gleb Wataghin* Physics Institute of the State University of Campinas to obtain the Master's degree in Physics.

Este exemplar corresponde à versão final da dissertação de mestrado defendida pelo aluno Rodrigo Freitas e orientada pelo Prof. Dr. Maurice de Koning.

Maurice de Koning

Campinas
2013

Ficha catalográfica
Universidade Estadual de Campinas
Biblioteca do Instituto de Física Gleb Wataghin
Valkíria Succi Vicente - CRB 8/5398

F884m

Freitas, Rodrigo Moura, 1989-
Molecular simulation : methods and applications / Rodrigo Moura Freitas. – Campinas, SP : [s.n.], 2013.

Orientador: Maurice de Koning.
Dissertação (mestrado) – Universidade Estadual de Campinas, Instituto de Física Gleb Wataghin.

1. Cálculo de energia livre. 2. Dinâmica molecular. 3. Eventos raros. 4. Ferro. 5. Gelo. I. Koning, Maurice de,1969-. II. Universidade Estadual de Campinas. Instituto de Física Gleb Wataghin. III. Título.

Informações para Biblioteca Digital

Título em outro idioma: Simulação molecular : métodos e aplicações
Palavras-chave em inglês:
Free-energy calculations
Molecular dynamics
Rare events
Iron
Ice
Área de concentração: Física
Titulação: Mestre em Física
Banca examinadora:
Maurice de Koning [Orientador]
Alex Antonelli
João Francisco Justo Filho
Data de defesa: 29-07-2013
Programa de Pós-Graduação: Física

MEMBROS DA COMISSÃO JULGADORA DA DISSERTAÇÃO DE MESTRADO DE **RODRIGO MOURA FREITAS - RA 072336** APRESENTADA E APROVADA AO INSTITUTO DE FÍSICA "GLEB WATAGHIN", DA UNIVERSIDADE ESTADUAL DE CAMPINAS, EM 29 / 07 / 2013.

COMISSÃO JULGADORA:

Prof. Dr. Maurice de Koning - Orientador do Candidato
DFMC/IFGW/UNICAMP

Prof. Dr. João Francisco Justo Filho – Escola Politécnica / USP

Prof. Dr. Alex Antonelli – DFMC/IFGW/UNICAMP

Abstract

Due to the conceptual and technical advances being made in computational physics and computational materials science we have been able to tackle problems that were inaccessible a few years ago. In this dissertation we study the evolution of some of these techniques, presenting the theory and simulation methods to study first order phase transitions with emphasis on state-of-the-art free-energy calculation (*Reversible Scaling*) and rare event (*Forward Flux Sampling*) methods using the atomistic simulation technique of Molecular Dynamics. The evolution and efficiency improvement of these techniques is presented together with applications to simple systems that allow exact solution as well as the more the complex case of Martensitic phase transitions.

We also present the application of numerical methods to study Pauling's model of ice. We have developed and implemented a new algorithm for efficient generation of disordered ice structures. This ice generator algorithm allows us to create ice Ih cells of sizes not reported before. Using this algorithm we address finite size effects not studied before.

Resumo

Devido aos avanços conceptuais e técnicos feitos em física computacional e ciência dos materiais computacional nós estamos aptos a resolver problemas que eram inacessíveis a alguns anos atrás. Nessa dissertação estudamos a evolução de alguma destas técnicas, apresentando a teoria e técnicas de simulação computacional para estudar transições de fase de primeira ordem com ênfase nas técnicas mais avançadas de cálculo de energia livre (*Reversible Scaling*) e métodos de simulação de eventos raros (*Forward Flux Sampling*) usando a técnica de simulação atomística da Dinâmica Molecular. A evolução e melhora da eficiência destas técnicas é apresentada junto com aplicações a sistemas simples que permitem solução exata e também ao caso mais complexo da transição de fase Martensítica.

Também apresentamos a aplicação de métodos numéricos no estudo do modelo de Pauling para o gelo. Nós desenvolvemos e implementamos um novo algoritmo para a criação eficiente de estruturas de gelo desordenadas. Este algoritmo de geração de cristais de gelo nos permitiu criar células de gelo Ih de tamanhos que não eram possíveis antes. Usando este algoritmo abordamos o problema de efeitos de tamanho finito não estudados anteriormente.

Acknowledgments/Agradecimentos

Primeiramente gostaria de ampliar a abrangência desta seção de agradecimentos. Além de todos que foram importantes durante meu tempo no mestrado eu gostaria de incluir aqui meus agradecimentos a todos que participaram dos meus anos na UNICAMP, desde o início da graduação em 2007.

Partindo dos primeiros princípios começo agradecendo aqueles que muito incentivaram, apoiaram e motivaram meus estudos para entrar na UNICAMP. Minha prima, Maria da Gloria, pelo apoio de sempre e ajuda fundamental nas muitas etapas de preparação para o vestibular. Ao meu tio Cláudio Freitas e ao Renato Acconcia por me explicarem incansavelmente a necessidade de se ter um ensino superior de qualidade. A experiência de vocês três foi fundamental, sou grato por tê-los escutado.

Nos dois primeiros anos como aluno de graduação tive o privilégio de ter quatro cursos ministrados pelo professor Ary O. Chiacchio (paraninfo da nossa turma na formatura). Agradeço pela enorme consideração pelos alunos, coerência sem igual nos cursos e senso de humor ímpar. Aprendi que tipo de professor gostaria de ser nestas aulas.

Durante a graduação eu e muitos colegas encontramos a motivação necessária para seguirmos em frente na carreira científica em conversas com professor Alberto Saa. Sou grato por isso e por ter me apresentado ao meu orientador de iniciação científica. O professor Edison Zacarias foi responsável por me introduzir, ao longo de dois anos de iniciação científica, à área da física computacional. Agradeço por não poupar esforços em me ajudar nesta época tão importante na trajetória de um aluno. O que eu aprendi nestes anos foi o diferencial que precisei em muitos momentos nos anos que se seguiram.

Minha monografia de graduação e esta dissertação de mestrado foram feitas sob orientação do professor Maurice de Koning. Ao longo dos últimos três anos tivemos incontáveis conversas e inúmeros emails foram trocados. Agradeço por todas correções, sugestões e conselhos. Pelos meus poucos momentos de insegurança e teimosia, e os meus muitos momentos de confusão, eu agradeço também a paciência. Sou grato pela sua maneira tranquila, leve e responsável de ser um orientador, sem abrir mão do senso crítico que tanto me fez aprender e melhorar.

Meus pais, Jayme e Mariângela, eu agradeço pelo apoio incondicional em todas as etapas da minha vida. Obrigado por sempre fazerem o seu melhor em todos momentos que eu precisei contar com vocês.

Aos amigos eu devo muito. À todos amigos que fiz no tempo que morei na República Amsterdam, obrigado pelos momentos inesquecíveis. Deles surgiram histórias que eu contarei orgulhosamente (ou não) quando ficar mais velho. Ao Thiago Vaz eu agradeço pela amizade sem igual e por poder contar contigo sempre que necessário. Meu último semestre na UNICAMP tem sido divertidíssimo e devo isso ao Renan, Thiago (Muringa), Ygor (Roque), Rafael (Cursão), meu irmão Leonardo, Carol e todo o pessoal

que conheci em Ribeirão Preto. Por todo companheirismo, animação e amizade eu agradeço a Andrezza, aprendi muito com você. Ao Felipe Santos eu agradeço pela companhia e discussões durante os cursos de mestrado, também por sempre apresentar sua opinião (quase sempre) diametralmente oposta a minha sem receios. Agradeço a Débora Princepe pelo carinho e os momentos, nossas conversas tiveram um valor inestimável. Sua notável competência, dedicação e honestidade foram, e continuam a ser, um exemplo para mim. À todos os colegas da pós-graduação do IFGW eu agradeço à companhia do dia-a-dia. Ao pessoal do capítulo da Optical Society of America na UNICAMP eu agradeço à oportunidade de participar de eventos que muito mudaram a minha visão sobre o ensino de ciência em geral, foi uma experiência incrível.

During these past years I have met a number of people who I owe much gratitude and thanks for their significant impacts on the direction of my studies . I am grateful to all the participants of the SISSA/CECAM Summer School on Atomistic Simulation Techniques with a special thanks to Fernando Gargiulo for his hospitality and kindness. I would also like to thank all the participants and organizers of the Hermes Summer School on Materials Modelling in London for not only changing the way I see science communication but also for opening my eyes to computational techniques at different scales. Beyond this I can not begin to overstate how fun my time was at the Workshop on Computer Programming and Advanced Tools for Scientific Research Work. I would also like to give a special thank you to Ryan for being so upbeat and cheerful aswell as a great tour buddy. It is a sorrowful fact to know that I may never met many of you again.

I had a delightful experience living for six months in Livermore, at the San Francisco Bay Area. I want to thank Fred, Pinky, James, Jeska and Erika for receiving me so well in your house and making my transition to another culture so smooth. Thanks to you, Sara, Eric and Carlene my day-to-day life was happier. I was warmly welcome in Lawrence Livermore National Laboratory by all my colleagues from the Condensed Matter and Materials Science Division. I very much appreciate all the efforts to make me feel as a part of this group. Thank you Karen for sharing a few laughs with me and making sure that everything was running smoothly, even when it was not your job to do so. A very special thank you to Tomas, David, Celia and Sylvain for all the wonderful experiences traveling we had the pleasure of sharing. My days in California would not have been what they were without you guys.

I also owe a very special thank you to Vasily for helping me since the very beginning of my time in Livermore, for receiving me so well in LLNL, for the beers in Ale House and for so much more. I have learned very much from our conversations and from your unique personality. My research time at LLNL was incredibly intense and involving and it would not be possible without both my advisors at LLNL, Vasily and Babak. Thanks for all conversations and time devoted to my project. The active discussion

of ideas, your patience with my ideas and being able to see how you both work and think were all very beneficial, instructive, and insightful.

I want to thank Professor Mark Asta for the amazing opportunity to join your group in UC Berkeley and for trusting in my capacities too.

To Vasily, Babak and Maurice I am deeply in debt with. Your help opened so many doors that I cannot even count anymore. What you guys did was invaluable. My most humble and sincere thank you.

Gostaria de agradecer à presença dos professores Amir Caldeira e José Brum no meu seminário do Exame de Qualificação do Mestrado. Também agradeço aos professores Alex Antonelli e Marcus Bonança pela presença no Seminário de Pré-Requisito de Mestrado e às sugestões apresentadas ao final do mesmo. Meu muito obrigado aos professores Alex Antonelli e João Francisco Justo Filho por participarem da banca da minha Defesa de Mestrado e as sugestões e correções feitas a essa dissertação. Agradeço ao Oswaldo e a Emília da Secretaria do DFMC pela eterna boa vontade em ajudar e a competência sem igual com que realizam seu trabalho.

Quanto ao apoio financeiro, agradeço ao CNPq pela bolsa de iniciação científica durante a graduação. Agradeço à FAPESP pela bolsa de mestrado e também pela Bolsa Estágio de Pesquisa no Exterior. Ao LLNL eu agradeço aos recursos fornecidos para que esse trabalho fosse possível.

State University of Campinas, UNICAMP

Campinas, SP - Brazil *Rodrigo Freitas*

July, 2013

Contents

Abstract/Resumo **vii**

Acknowledgments/Agradecimentos **ix**

1 Computational Physics and Materials Science **1**

1.1 Why Simulations? . . . 1

1.2 Moore's law and Computational Methods . . . 3

1.3 The Fermi-Pasta-Ulam Work and Solitons . . . 3

1.4 Quantum Effects in Materials Deformations . . . 4

1.5 Scope of the Dissertation . . . 5

2 Molecular Dynamics **7**

2.1 The Many Body Problem . . . 8

2.2 Integration of the Equations of Motion . . . 12

2.3 Molecular Dynamics and Statistical Mechanics . . . 17

2.4 MD in Different Ensembles: Anderson barostat . . . 19

2.5 Canonical Ensemble: Nosé-Hoover Chain thermostat . . . 22

2.6 Nosé-Hoover Chain Thermostat and Harmonic Oscillators . . . 25

2.7 Nosé-Hoover Chain Thermostat and the Harmonic Approximation . . . 28

2.8 Canonical Ensemble: Langevin Thermostat . . . 32

2.9 Langevin Thermostat Applied to Harmonic Systems . . . 34

3 Phase Transitions and Free-Energy Calculation **39**

3.1 Phase Stability . . . 39

3.2 MD and Free Energy Calculation: λ-integration method . . . 41

3.3 Adiabatic Switching . . . 44

3.4 Frenkel-Ladd Method . . . 46

3.5 Frenkel-Ladd: Harmonic Oscillators . . . 48
3.6 Reversible-Scaling Method . . . 51
3.7 Reversible Scaling: Harmonic Oscillators . . . 53
3.8 First Order Phase Transitions and Classical Nucleation Theory . . . 55
3.9 Thermodynamics of Martensitic Phase Transitions using RS . . . 61
3.10 Kinetics of Martensitic Phase Transitions . . . 71

4 Pauling's Model of Ice **79**
4.1 Ice Ih and Pauling's Model . . . 79
4.2 Ice Network Generator: Algorithm . . . 81
4.3 Ice Network Generator: Technical Details . . . 84
4.4 L_{path} effects . . . 84
4.5 Dipole-Dipole Correlations . . . 87
4.6 Exact Results for the Square Ice . . . 90
4.7 Simulations for the Square Ice . . . 91
4.8 Ice Ih Structure and Polarization Factor . . . 95

5 Conclusions and Outlook **97**
5.1 Molecular Dynamics . . . 97
5.2 Ice Network Generator . . . 98

A Switching Functions **99**
A.1 Reversible Scaling . . . 99
A.2 Frenkel-Ladd . . . 100

Bibliography **101**

"The first principle is that you must not fool yourself, and you are the easiest person to fool."

Richard P. Feynman
"What is and What Should be the Role of Scientific Culture in Modern Society", 1964.

To my brother, Leonardo. My sister, Camila. Carol and Ariel.

Chapter 1

Computational Physics and Materials Science

In physics and science in general there exists a well defined line that creates an idea at the very root of the scientific method: the theory/experiment dichotomy. Each of these parts is fundamental to the existence of science as something meaninful. Richard P. Feynman summarized in a very simple sentence the dynamics between theory and experiment:

> "*First you guess. Don't laugh, this is the most important step. Then you compute the consequences. Compare the consequences to experience. If it disagrees with experience, the guess is wrong. In that simple statement is the key to science. It doesn't matter how beautiful your guess is or how smart you are or what your name is. If it disagrees with experiment, it's wrong. That's all there is to it.*"

In this chapter I will introduce ideas about computational physics and computational materials science and illustrate the role of this new tool in the old and well stabilished notions of theory and experiment. Much of what will be said was inspired by the texts *Simulations: the Dark Side* by Frenkel (2013), *Synergistic Science* by Yip (2003) and the many answers I have got from collegues and friends to the question: *Why do we do simulations?*

1.1 Why Simulations?

A simulation must answer a question. There is absolutely no meaning in running a simulation that does not help to answer any question. It is like the most famous passage in the comic science fiction book series *Hitchhikers Guide to the Galaxy* by Adams (1979-1992) where the supercomputer Deep Thought

completes a huge calculation to answer the question of the book *Life, the Universe and Everything* and the final answer is 42. The problem is that nobody actually remembers what the question was.

Unlike **experiments** we cannot use simulations as a tool to discover fundamental laws of nature. Strictly speaking it is not even completely correct to use the word 'simulation'. Most of the time what we are actually doing is 'modeling': every simulation starts with the choice of a model (*e.g.* interatomic potential for a Molecular Dynamics simulation) that describes the real system we want to study. If this model is good enough it will include all physical features necessary to reproduce and study a certain *phenomenon* present in our system. Although we can always refine our model as much as we wish, we will never actually *simulate* that specific real system present in a true experiment by computer: either because we do not have computing power to include all the details or because our knowledge of all details of nature is incomplete, or both.

Unlike **theories** we cannot use simulations as a tool to summarize our understanding of nature. Nevertheless simulations are still useful as a powerful tool to provide important insights. For example, we can use modeling of a system to test if it captures the essential physics of a phenomenon or if there is something missing. We can therefore use simulations as a 'discovery tool' and obtain predictions of approximate theories that could not be obtained analytically. In fact, it can be a very powerful discovery tool since in a simulation you typically have control over all parameters to be simulated and therefore can avoid the interference of any external agent. Furthermore one also has access to all microscopic details of the system, something unimaginable experimentally.

Experiment and theory have a two-way relationship: experiments provide a test for theories and theories make predictions for experiments. Theories also help us to better understand the physics of an experiment and experiments help us to better define the limitations of a theory. Computer simulations are dependent of both, theory and experiment. Theories provide the model for simulations and also analytical results that help us to test and verify the correctness of our simulation. Frequently this is vital to a computer code due to the complexity of numerical procedures involved and even because of the limitations of computers. Therefore exact results from theories are one of the few methods to make sure that we are not fooling ourselves. Experiments provide the final test to verify if our model captures the physics of a phenomenon, in addition they may point at certain phenomena and systems unaccessible to the current experimental techniques. Here computer simulations can become useful as a guide to what is happening and how to approach such a system.

With this discussion we have seen that *there is* space for simulations and that theory or experiment can hardly fill this space. Thus we can conclude that there is also a *need* for simulations.

1.2 Moore's law and Computational Methods

For the sake of keeping computational simulations useful there is a need for the continuous development of better method and computers. Over the last 60 years the continuous speed-up of processors following the Moore's law (Moore et al., 1965), jointly with the creation and development of parallel computing[1] have increased the speed at which computers perform elementary calculations by a factor of almost 10^{15}. Such an astonishing evolution allowed us to perform simulations that were totally inaccessible a decade before. This makes us wonder if it is necessary to "waste" our efforts on further developing more efficient computational methods or if it would be better to focus on other problems and just wait for a faster computer to become available so that we can simulate a bigger system.

New algorithms and techniques allowed us to simulate systems and phenomena not possible before such as rare events, quantum systems, free-energy calculations and many others. Many of the algorithm improvements are concerned with a better performance. Later in this dissertation we will present an example of this kind of improvement, namely the development of free-energy calculation techniques by computer simulations that involves a significant gain of performance. Also important were the algorithms that enabled new types of calculations. For example, we had the development of the Density Functional Theory (DFT) by Kohn et al. (1965) that allowed the study of many different systems in which the electronic structure is important, particularly in chemistry and solid state physics. This last type of improvement cannot be achieved by the development of better computers. It results directly in a new kind of information that can be extracted from a simulation. This was not possible before because we did not know how, even though we already had sufficient computer power.

We now present a few examples of how the combination of good algorithms with adequate computing power turned computer simulations into a useful tool and resulted in scientific discoveries and new insights in different areas of physics and materials science.

1.3 The Fermi-Pasta-Ulam Work and Solitons

In 1955 Enrico Fermi, John Pasta and Stanislaw Ulam used the then new computer technology (the famous MANIAC I computer) to solve an important problem at that time and observed for the first time a phenomenon that would later be named *solitons*. Nowadays solitons are found to be present in different areas of physics like optics, fluids and Bose-Einstein condensates. They initially intended to study a problem of nonlinearity. The simulation followed the motion of 64 unidimensional masses connected by

[1] The largest supercomputer ever created is the Sequoia, located in the *Lawrence Livermore National Laboratory, LLNL*. This supercomputer has more than 1.5 million cores and capacity to operate at 16.3 petaflops (flop = floating point operations per second). An usual personal computer operates at 10 gigaflops, that is a difference by a factor of 10^5.

springs on a horizontal line. The initial configuration of the system was such that the displacement of each mass followed a half sine wave pattern. If the springs were strictly linear the sine wave pattern would be maintained. The intention of the simulation was to add a small degree of nonlinearity to the springs and check if, in time, the nonlinearity would break the sine pattern and distribute the energy equally between all masses. What actually happened was that, although the sine wave pattern evolved in a more complex form, it would periodically return to the initial configuration. This problem is now known as the Fermi-Pasta-Ulam (FPU) problem (Fermi, Pasta, and Ulam, 1955).

A few years later the FPU work was revisited by Zabusky and Kruskal (1965). They transformed the discrete problem of harmonic oscillators into one for a continuous system. Using the same initial condition of a half sine wave they observed the same result as FPU: the system would evolve into a complex pattern but, given enough time, it would return to the initial state and repeat the cycle, although in a different way. In these cycles they could observe something new: the growth of individual waves that moved independently and with velocities dependent on they height. When these new waves collided they would pass through each other almost unscattered and eventually these waves would align to reproduce the initial state before separating again and repeating. They decided to give a name to that remarkably result, the solitary waves *solitons*. This discovery was received with a certain skepticism but, in time, physicists started to encounter solitons solutions in their wave equations. This work is a classical example of how computer simulations can "*provide insight into deep and fundamental properties of a mathematical model and lead to the discovery of completely new phenomena*", (Zabusky, 2005).

1.4 Quantum Effects in Materials Deformations

Quantum effects such as tunneling and energy discretization are known to become noticeable in solid state physics at low temperatures when the thermal fluctuations are so low that the quantum fluctuations become relevant. Proville et al. (2012) have analyzed, for the first time, the role of quantum effects in the deformation of metals and obtained new insights using computer simulations.

When metals deform they do so by the movement of linear defects know as dislocations through the crystal. The resistance of a metal to deform is therefore linked to the resistance of the dislocations to move. The stress necessary for the dislocation to start moving and deform the metal is known as Peierls stress. As we increase the temperature the crystal loses its hardness, meaning that thermal fluctuations have influence on the motion of dislocations. It is believed that the motion of the dislocation occurs by the creation of a kink-pair (Ackland, 2012): two steps in the dislocation line that, once created, can propagate easily along the defect, moving it forward. This process is also believed to be the rate-limiting step in the dislocation motion. Despite this insight there has been a long-standing discrepancy between theory and

experiments regarding the behavior of dislocations at low temperatures in iron and other BCC metals.

Proville et al. (2012) have performed calculations on dislocations movement in iron that suggest that it is necessary to invoke quantum effects to describe the system. They found that the effect of quantum statistics and zero-point motion are important up to about half the Debye temperature of iron ($\approx$ 470K). The inclusion of these effects reduces the Peierls stress for dislocations motion in iron at the low temperature limit by a factor of approximately two. The computational efforts of this simulation "*cannot be underestimated, and would have been impossible a few years ago*", (Ackland, 2012).

1.5 Scope of the Dissertation

This dissertation starts with a discussion on the use of the atomistic simulation technique of *Molecular Dynamics* to study first-order phase transitions. After this brief introduction to computational simulations and the driving force motivating their use, we start chapter 2 by presenting the *Molecular Dynamics* methods. The discussion is centered about how we can link the many different algorithms of this technique with physical ideas that motivate it. A more detailed description of the implementation of these algorithms and other technical details are left to many different text books about this area (Tuckerman, 2010; Frenkel and Smit, 2001).

In chapter 3 we approach specific methods to study first-order phase transitions. We introduce the *Reversible Scaling* (de Koning et al., 1999b) method for free-energy calculations and the *Forward Flux Sampling* (Allen et al., 2005) method to study rare events. Subsequently we apply these methods to the problem of the Martensitic phase transition is pure iron (Porter and Easterling, 1992). Before doing so we study the application of these methods to systems for which exact results are available so that we can test our implementation and gain insights about how these methods work.

Unless explicitly stated otherwise, the results presented in this dissertation were obtained with our own implementation of these techniques in the parallel and large scale Molecular Dynamics simulator LAMMPS. Many different new commands and functionalities were programmed to obtain these results. All of the code was written in such a way that they can be used within the LAMMPS scripting language.

In chapter 4 we present a new algorithm to created disordered ice structure in accordance with the Bernal and Fowler (1933) ice rules. We start by introducing the Ih phase of ice and the Pauling's model of ice (Pauling, 1935). Then the ice network generator algorithm is presented and we show how we can use it to study Pauling's model. This is the first algorithm reported capable to created large ice cells. Because of this emphasis is given in the study of finite size effects on the ice structures.

Chapter 2

Molecular Dynamics

Molecular Dynamics (MD) is a technique for atomistic simulation of classical many-body systems. The system model considers atoms interacting through an interatomic potential $V(\mathbf{r})$ and numerically integrates the Newtonian equations of motion to obtain the atomic trajectories and resolve the dynamics of the system. The first MD simulations were perfomed by Alder and Wainwright (1957, 1959) at the *Lawrence Livermore National Laboratory* on the study of phase transitions in a sytem of rigid spheres. Simulations of realistic systems took place a few years later when Rahman (1964) studied a system of 864 Argon atoms using a continuous potential and later Stillinger and Rahman (1974) investigated liquid water. The development and implementation of an efficient computational code to perform MD simulations is not a trivial task, in particular for parallel codes (Plimpton et al., 1995). Nevertheless, due to the wide spectrum of problems that can be tackled using MD, different research groups developed efficient and parallel MD codes. Examples of open source computational codes are LAMMPS and MD++, largely used for the study of materials and mechanical properties of solids.

To get an idea of the colossal amount of work involved in the creation of such codes we only need to report a few numbers: the source code of LAMMPS has more than 620,000 lines, resulting in more than 145MB of code files developed along 18 years. The paper (Plimpton et al., 1995) that describes much of the technical problems of the implementation of this code has more than 3600 citations and the website of the distribution lists more than 4900 articles published using the code. It is possible to get a glimpse of the wide applicability of a code like this from the following sentences, quoted from the distribution homepage:

> *LAMMPS has potentials for soft materials (biomolecules, polymers) and solid-state materials (metals, semiconductors) and coarse-grained or mesoscopic systems. It can be used to model atoms or, more generically, as a parallel particle simulator at the atomic, meso, or continuum scale.*

In this chapter I present the physics behind an MD code. Although classical mechanics and statistical physics are undoubtedly the pillars of the MD theory, many of the algorithms and simulation techniques are rooted in different areas, namely: stochastic processes, classical electromagnetism, quantum mechanics, elasticity theory and thermodynamics of non-equilibrium systems. Fundamentally, all these methods were created to solve the same problem, the dynamics of many-body systems.

2.1 The Many Body Problem

The understanding and quantification of the dynamics of a many-body system is a fundamental and recurring problem in condensed matter physics. The fact that emergent phenomena arise when systems of many particles are considered has been recognized since a long time ago (Anderson, 1972). Given the Hamiltonian operator $\mathcal{H}$ of a system then, at a time t_0, the complete description of the state of the system is given by a wave function $|\Psi(t_0)\rangle$. The solution for the dynamics of this state, assuming that no measurement is made, comes from the Schrödinger's equation

$$-i\hbar\frac{\partial}{\partial t}|\Psi(t)\rangle = \mathcal{H}|\Psi(t)\rangle\,. \tag{2.1}$$

Due to the linear character of eq.(2.1) the possible solutions are frequently written as a linear combination of the stationary states of the system, which are the eigenstates of the Hamiltonian operator

$$\mathcal{H}|\psi_n\rangle = E_n|\psi_n\rangle\,.$$

Therefore, the identification of these eigenstates is an important part of the process of solving the dynamics of the system.

In an atomistic system with N electrons and M nuclei the Hamiltonian is written as

$$\mathcal{H} = \sum_{i=1}^{N}\frac{\mathbf{p}_i^2}{2m_e} + \sum_{i=1}^{M}\frac{\mathbf{P}_i^2}{2M_i} + \sum_{i=1}^{N}\sum_{j>i}^{N}\frac{e^2}{|\mathbf{r}_i-\mathbf{r}_j|} + \sum_{i=1}^{M}\sum_{j>i}^{M}\frac{Z_iZ_je^2}{|\mathbf{R}_i-\mathbf{R}_j|} - \sum_{i=1}^{N}\sum_{j=1}^{M}\frac{Z_je^2}{|\mathbf{r}_i-\mathbf{R}_j|} \tag{2.2}$$

where capital letters refer to nucleus variables and lowercase variables to electrons. Also, N and M are $\sim 10^{23}$. Already at this point we can notice the great mathematical difficulty that arises when we try to tackle this Hamiltonian. We can increase it even more by adding the spin degrees of freedom and the terms of spin-orbit and spin-spin coupling . Thus the solution of the dynamics of a many-body system via Schrödinger's equation is impracticable, computationally or analytically. It is clear that any method that solves a system described by eq.(2.2) must include approximations with elements of the classical mechanics.

The first step towards the solution of the full many-body Hamiltonian of eq.(2.2) is the Born-Oppenheimer approximation (Born and Oppenheimer, 1927). In this approximation the kinetic energy of

the nuclei

$$T_n = \sum_{i=1}^{M} \frac{\mathbf{P}_i^2}{2M_i}$$

is removed from the Hamiltonian of eq.(2.2). We justify this approximation by the fact that the mass of the nuclei is approximately 10^4 greater than the mass of a electron, hence if the momentum of both have the same order of magnitude then the kinetic energy of an electron is $\sim 10^4$ times greater than the kinetic energy of one of the nuclei. The resulting Hamiltonian is

$$\mathcal{H}_e = \sum_{i=1}^{N} \frac{\mathbf{p}_i^2}{2m_e} + \sum_{i=1}^{N}\sum_{j>i}^{N} \frac{e^2}{|\mathbf{r}_i - \mathbf{r}_j|} + \sum_{i=1}^{M}\sum_{j>i}^{M} \frac{Z_i Z_j e^2}{|\mathbf{R}_i - \mathbf{R}_j|} - \sum_{i=1}^{N}\sum_{j=1}^{M} \frac{Z_j e^2}{|\mathbf{r}_i - \mathbf{R}_j|}.$$

Notice that this is an electronic Hamiltonian, *i.e.* the position of the nuclei is only a parameter. This means that, although the electrons are still interacting with the nuclei by means of the Coulombian potential, the nuclei have fixed positions and do not move. This approximated Hamiltonian is still too complex to be handled analytically (*i.e.*, compute the complete set of eigenstates and the eigenenergy spectrum). Nevertheless the electronic Hamiltonian is of fundamental importance in the approximate solution of the system's dynamics.

The electronic energy of the system is a functional of its state

$$E[\psi] = \langle\psi|\, \mathcal{H}_e \,|\psi\rangle\,.$$

Thus, given the nuclei positions $\mathbf{R} = \{\mathbf{R}_i\}$, the energy of the ground state of this specific configuration is

$$E_0 = \min_{\psi} \langle\psi|\, \mathcal{H}_e \,|\psi\rangle\,, \tag{2.3}$$

where the right-hand side of eq.(2.3) is minimized by the wave function of the ground electronic state $|\psi_0\rangle$. It is possible to obtain the exact solution of eq.(2.3) using *Density Functional Theory* (DFT) (Hohenberg and Kohn, 1964; Kohn et al., 1965), that receives this name because the energy minimization is carried out using the electronic density $n(\mathbf{r})$ as the fundamental variable instead of the electronic wave function. In real problems, many different approximations are necessary in order to perform the minimization computationally.

Once the electronic density $n(\mathbf{r})$ has been obtained, we solve the dynamics of the system by means of a connection with classical mechanics. To introduce this connection we use the Hellman-Feynman theorem (Feynman, 1939). Suppose that the Hamiltonian of the system depends on a parameter λ. Hence the wave function of a steady state of this system and its corresponding eigenenergies also depend on this parameter

$$\mathcal{H}(\lambda)\,|\psi(\lambda)\rangle = E_\lambda\,|\psi(\lambda)\rangle \qquad \Rightarrow \qquad E_\lambda = \langle\psi(\lambda)|\,\mathcal{H}(\lambda)\,|\psi(\lambda)\rangle\,.$$

We assume that the state is normalized, *i.e.*, $\langle\psi(\lambda)|\,\psi(\lambda)\rangle = 1$. Differentiating with respect to λ we obtain

$$\begin{aligned}
\frac{\partial E_\lambda}{\partial\lambda} &= \left\langle\psi(\lambda)\right| \frac{\partial\mathcal{H}(\lambda)}{\partial\lambda} \left|\psi(\lambda)\right\rangle + \left\langle\frac{\partial\psi(\lambda)}{\partial\lambda}\right| \mathcal{H}(\lambda) \left|\psi(\lambda)\right\rangle + \left\langle\psi(\lambda)\right| \mathcal{H}(\lambda) \left|\frac{\partial\psi(\lambda)}{\partial\lambda}\right\rangle \\
&= \left\langle\psi(\lambda)\right| \frac{\partial\mathcal{H}(\lambda)}{\partial\lambda} \left|\psi(\lambda)\right\rangle + E_\lambda \left[\left\langle\frac{\partial\psi(\lambda)}{\partial\lambda}\right| \psi(\lambda)\right\rangle + \left\langle\psi(\lambda)\right| \frac{\partial\psi(\lambda)}{\partial\lambda}\right\rangle\Big] \\
&= \left\langle\psi(\lambda)\right| \frac{\partial\mathcal{H}(\lambda)}{\partial\lambda} \left|\psi(\lambda)\right\rangle + E_\lambda \frac{\partial}{\partial\lambda} \langle\psi(\lambda)|\,\psi(\lambda)\rangle \\
&= \left\langle\psi(\lambda)\right| \frac{\partial\mathcal{H}(\lambda)}{\partial\lambda} \left|\psi(\lambda)\right\rangle .
\end{aligned}$$

Therefore the Hellman-Feynman theorem gives us

$$\frac{\partial E_\lambda}{\partial\lambda} = \left\langle\psi(\lambda)\right| \frac{\partial\mathcal{H}(\lambda)}{\partial\lambda} \left|\psi(\lambda)\right\rangle . \tag{2.4}$$

We are going to apply the Hellman-Feynman theorem using the nuclei position $\mathbf{R}$ as the λ parameter. The force on each nucleus is related to the gradient of the total energy, because the nuclei position $\mathbf{R}$ are the only parameters in the electronic Hamiltonian, $\mathcal{H}_e$. Applying eq.(2.4) with $\lambda = \mathbf{R}$, and considering coordinate x of the k-th nucleus we have

$$F_{X,k} = -\frac{\partial E}{\partial X_k} = -\left\langle\psi\right| \frac{\partial\mathcal{H}_e}{\partial X_k} \left|\psi\right\rangle$$

differentiating $\mathcal{H}_e$ we obtain

$$\begin{aligned}
\frac{\partial\mathcal{H}_e}{\partial X_k} &= \frac{\partial}{\partial X_k} \left(\sum_{i=1}^{M}\sum_{j>i}^{M} \frac{Z_i Z_j e^2}{|\mathbf{R}_i - \mathbf{R}_j|} - \sum_{i=1}^{N}\sum_{j=1}^{M} \frac{Z_j e^2}{|\mathbf{r}_i - \mathbf{R}_j|} \right) \\
&= -Z_k e^2 \sum_{i\neq k}^{M} Z_i \frac{X_i - X_k}{|\mathbf{R}_i - \mathbf{R}_k|^3} + Z_k e^2 \sum_{i=1}^{N} \frac{x_i - X_k}{|\mathbf{r}_i - \mathbf{R}_k|^3} .
\end{aligned}$$

Thus

$$\begin{aligned}
\left\langle\psi\right| \frac{\partial\mathcal{H}_e}{\partial X_k} \left|\psi\right\rangle &= -Z_k e^2 \sum_{i\neq k}^{M} Z_i \frac{X_i - X_k}{|\mathbf{R}_i - \mathbf{R}_k|^3} + \left\langle\psi\right| Z_k e^2 \sum_{i=1}^{N} \frac{x_i - X_k}{|\mathbf{r}_i - \mathbf{R}_k|^3} \left|\psi\right\rangle \\
&= -Z_k e^2 \sum_{i\neq k}^{M} Z_i \frac{X_i - X_k}{|\mathbf{R}_i - \mathbf{R}_k|^3} + \int d^3\mathbf{r}\, |\psi(\mathbf{r})|^2\, N Z_k e^2 \frac{x - X_k}{|\mathbf{r} - \mathbf{R}_k|^3} \\
&= -Z_k \left[\sum_{i\neq k}^{M} Z_i e^2 \frac{X_i - X_k}{|\mathbf{R}_i - \mathbf{R}_k|^3} - Z_k \int d^3\mathbf{r}\, n(\mathbf{r}) \frac{x - X_k}{|\mathbf{r} - \mathbf{R}_k|^3} \right] ,
\end{aligned}$$

and the force on nucleus k is given by

$$\mathbf{F}_k = -\boldsymbol{\nabla} E = Z_k \left[\sum_{i\neq k}^{M} Z_i e^2 \frac{\mathbf{R}_i - \mathbf{R}_k}{|\mathbf{R}_i - \mathbf{R}_k|^3} - \int d^3\mathbf{r}\, n(\mathbf{r}) \frac{\mathbf{r} - \mathbf{R}_k}{|\mathbf{r} - \mathbf{R}_k|^3} \right] . \tag{2.5}$$

Given the nuclear configuration $\mathbf{R}$ we can obtain the associated electronic density $n(\mathbf{r})$ using eq.(2.3) and compute the total force $\mathbf{F} = \{\mathbf{F}_i\}$ on each nucleus using eq.(2.5). Therefore we have found an

algorithm to compute a fundamental element of the classical dynamics, namely the total force. We can now write a classical equation of motion for atom k

$$\frac{d^2\mathbf{r}_k(t)}{dt^2} = \frac{1}{m_k}\mathbf{F}_k.$$

By integrating this equation numerically, we solve the dynamics of the system (within the performed approximations). In the next section we are going to discuss the physical aspects of this integration, first we want the general overview of the algorithm that we have just found. In a general manner we can write the algorithm as a series of instructions:

1. Given $\mathbf{R}(t) = \{\mathbf{R}_i(t)\}$ compute the electronic density $n(\mathbf{r})$ using eq.(2.3).
2. Use $n(\mathbf{r})$ and eq.(2.5) to obtain $\mathbf{F}(t) = \{\mathbf{F}_k(t)\}$
3. Compute $\mathbf{R}(t+\delta t) = \{\mathbf{R}_i(t+\delta t)\}$ from the numerical integration of Newton's equations of motion using $\mathbf{F}(t) = \{\mathbf{F}_k(t)\}$.
4. Go back to 1 using $\mathbf{R}(t) \equiv \mathbf{R}(t+\delta t)$.

There is an implicit assumption in this algorithm that we can consider as the second part of the Born-Oppenheimer approximation, namely the adiabatic approximation. Notice that at each iteration of this algorithm the nuclear configuration $\mathbf{R}$ is altered and at each new configuration the electronic ground state corresponding to the Hamiltonian $\mathcal{H}_e$ is computed. Thus, during the nuclear motion we consider that the electrons are always in their ground state. Between each step δt the electrons have enough time to follow the motion of the nuclei and find the new ground state for this new configuration.

Intuitively the adiabatic approximation included in the Born-Oppenheimer approximation is plausible, as we have shown before, due to the mass difference between an electron and a nucleus. The kinetic energy of the electrons is much higher than that of the nuclei and therefore it is reasonable that the degrees of freedom related to the electrons have a much faster time evolution than those related to the nuclei. This approximation is a direct consequence of the adiabatic theorem:

> *If a perturbation acts slowly on the Hamiltonian of a certain system, then the system stays always in its instantaneous eigenstate.*

In the Born-Oppenheimer approximation the system is given by the electronic Hamiltonian $\mathcal{H}_e$ and the perturbation is the slow motion of the nuclei, changing the parameters $\mathbf{R}$ and $\mathcal{H}_e$.

Although the described formulation fulfills the objective of obtaining an approximate dynamics of a many-body system, in practice this formulation is computationally expensive due the need of performing the minimization of eq.(2.3) at each step to find the ground electronic state. The size of the system is

therefore limited to only a few hundred of atoms and still requires a high performance computer. The time scale is also limited to a few picoseconds.

The solution to avoid the computation of the electronic density at each step is to substitute the force of eq.(2.5) by the force derived from an effective interatomic potential $V(\mathbf{R})$. This potential implicitly mimics the effect of the electronic density and other degrees of freedom, as the electronic spin, and generates the force that acts on the nuclei in a computationally cheaper manner. This is done using analytical expressions specifically developed to capture the physics present in the atomic interactions of the materials to be simulated with this interatomic potential. Once the analytical equations for $V(\mathbf{R})$ are developed, the different parameters of this model are adjusted to reproduce specific characteristics of the substance under investigation. Frequently this fit is achieved with the help of experimental data. Because of this $V(\mathbf{R})$ is also known as an empirical potential.

Often it is not possible to capture all characteristics with an empirical potential. In this case it becomes necessary to obtain a compromise between a good description of certain properties at the cost of a poor description of others. For example, an empirical potential can describe very well the behavior of the liquid phase of a certain metal but it can have a poor description of the formation energy of certain crystal defects. In general no empirical potential will reproduce correctly the behavior of materials at conditions where quantum effects are important, *e.g.* specific heat at low temperatures. Therefore it is necessary to choose carefully a potential that correctly describes the physical quantities that are important for the physical phenomenon to be studied.

In order to differentiate between both algorithms we shall call "Molecular Dynamics" the algorithm that uses the empirical potentials $V(\mathbf{R})$ to compute the forces on the nuclei and "*ab initio* Molecular Dynamics" the algorithm that computes the electronic density "on-the-fly". The *ab initio* MD is a first-principles method, which means that it is not necessary to provide any external information (*e.g.* the potential $V(\mathbf{R})$ or the type of bond between the atoms of the material) to perform the simulation. As opposed to the first-principles methods there are the force-field methods in which the dynamics of the atoms is generated from an empirical potential. In the next chapters of this dissertation we are going to develop further aspects of MD, although much of what is going to be described is also applicable to *ab initio* MD.

2.2 Integration of the Equations of Motion

An important part of MD is related to the numerical integration of the classical equations of motion. The development of an algorithm that performs this integration carries a unique perspective of the deep connection between classical mechanics and MD. At first sight it may seem that the procedure of the

numerical integration is noting but a mathematical artifact, but let us further develop this idea and construct a simple method to integrate the Newtonian equations of motion.

We can write the equations to be solved as a set of coupled first order differential equation

$$\frac{d\mathbf{v}}{dt} = \frac{\mathbf{F}}{m}$$
$$\frac{d\mathbf{x}}{dt} = \mathbf{v}.$$

Applying the method of finite differences to first order in the time step Δt (Euler's method) to these equations yields

$$\mathbf{v}(t + \Delta t) = \mathbf{v}(t) + \frac{\mathbf{F}(t)}{m}\Delta t \tag{2.6}$$
$$\mathbf{x}(t + \Delta t) = \mathbf{x}(t) + \mathbf{v}(t)\Delta t.$$

It seems that we could finish this discussion now because we have just obtained a numerical recipe for integration. We only need to use a Δt that is sufficiently small so that the linear approximation to the differential equations is valid and by successively applications of the above equations we could evolve the trajectory of the system.

Let us apply eq.(2.6) to the unidimensional harmonic oscillator. To simplify the discussion we are going to use $m = k = 1$, initial conditions $x(t = 0) = 0$ and $v(t = 0) = 1$ and $\Delta t = 0.01$. With these parameters the phase space volume accessible to the system should be a circle with radius equal to 1 centered at the origin. Fig.2.1 (right) shows the trajectory of the system after 20000 steps. This result clearly shows that there is something wrong with the integrator. We can use the quantity

$$\Delta E = \frac{E(t) - E(0)}{E(0)}$$

as a measure for energy conservation. The result for the same simulation the result is shown in fig.2.1 (left) where we can see that the Euler integrator does not conserve energy. Although it is a valid numerical method for solving differential equations in general it fails when applied to Newton's equations of motion Giordano (1996). The problem is that these differential equations are specific: they possess certain symmetries and conservation laws that make them special. For example, from Hamilton's formulation of classical mechanics we know that the equations of motion can all be derived from a Hamiltonian $\mathcal{H}$. This is a very specific property of this set of equations since not all differential equations can be derived from a Hamiltonian. Thus, if we want solutions that possess physical meaning we need to incorporate these specific properties of the classical equations of motion into the numerical solution. Tuckerman et al. (1992) were the first to show how to systematically derive integration methods that contain all necessary physical properties. The analysis that follows is based on their work.

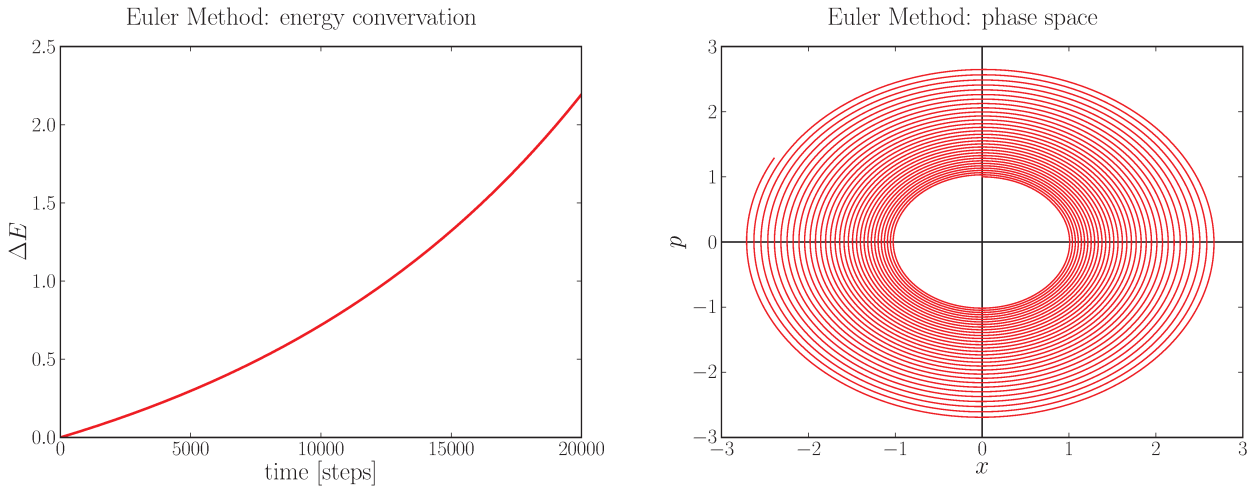

Figure 2.1: Energy conservation (**left**) and phase space (**right**) of a harmonic oscillator solved with Euler's integration method.

Before showing how to derive such algorithms let us highlight two properties that we want these algorithms to incorporate. The first property comes from the substitution of $t \to -t$ in Newton's second law:

$$\mathbf{F}_{tot} = m\frac{d^2\mathbf{x}}{dt^2} \qquad \Rightarrow \qquad \frac{d^2\mathbf{x}}{d(-t)^2} = \frac{d^2\mathbf{x}}{dt^2} = \mathbf{F}_{tot}$$

which reflects the fact that the equations of motion are time-reversible (we are assuming no time-dependent forces). The second property comes from the fact that an area $d\Gamma$ of the phase space is constant under canonical transformations: because the time evolution from t to $t + \Delta t$ has Jacobian equal to 1 (Landau, 1972), the Newtonian dynamics is a canonical transformation (generated by the Hamiltonian $\mathcal{H}$ itself) and therefore it is area-preserving. Thus we want an algorithm that is time-reversible and also conserves the phase space area under time evolution. To achieve this objective we are going to use as starting point Liouville's formulation of classical mechanics. Although all formulations of classical mechanics are equivalent it will become clear that Liouville's formulation is particularly useful for our purposes. It is worth to remember that all formulations of classical mechanics result in Newton's equations of motion and all others properties of classical mechanics, including its simplectic structure (time-reversible and area-preserving).

Consider now a function $f(\mathbf{r}, \mathbf{p})$ of the position $\mathbf{r}^N \equiv \mathbf{r}$ and momenta $\mathbf{p}^N = \mathbf{p}$ of all N particles of the system. The time derivative of this function is

$$\frac{df(\mathbf{r},\mathbf{p})}{dt} = \dot{f}(\mathbf{r},\mathbf{p}) = \dot{\mathbf{r}}.\frac{\partial f}{\partial \mathbf{r}} + \dot{\mathbf{p}}.\frac{\partial f}{\partial \mathbf{p}} \equiv iLf(\mathbf{r},\mathbf{p}) \tag{2.7}$$

where we have defined the Liouville's operator

$$iL \equiv \dot{\mathbf{r}}.\frac{\partial}{\partial \mathbf{r}} + \dot{\mathbf{p}}.\frac{\partial}{\partial \mathbf{p}} = \frac{\partial \mathcal{H}}{\partial \mathbf{p}}.\frac{\partial}{\partial \mathbf{r}} - \frac{\partial \mathcal{H}}{\partial \mathbf{r}}.\frac{\partial}{\partial \mathbf{p}} = \{\quad, \mathcal{H}\}$$

and $\{\quad,\quad\}$ are Poisson's brackets. We can formally integrate eq.(2.7) to

$$f\left[\mathbf{r}(t),\mathbf{p}(t)\right]=e^{iLt}f\left[\mathbf{r}(0),\mathbf{p}(0)\right], \tag{2.8}$$

which led us to define $U=e^{iLt}$ as the classical propagator. Notice that the Liouville's operator is compatible with the time-reversibility because it is unitary

$$U^{-1}(t)=U^{\dagger}(t)=U(-t).$$

Now we want to solve eq.(2.8) analytically. In order to do so we decompose Liouville's operator as $iL=iL_r+iL_p$ where $iL_r\equiv\dot{\mathbf{r}}(0).\frac{\partial}{\partial\mathbf{r}}$ and $iL_r=\dot{\mathbf{p}}(0).\frac{\partial}{\partial\mathbf{p}}$ and apply each part separately, leading to

$$\begin{aligned}
e^{iL_rt}f\left[\mathbf{r}(0),\mathbf{p}(0)\right]&=\sum_{n=0}^{\infty}\frac{1}{n!}\left[\dot{\mathbf{r}}(0).\frac{\partial}{\partial\mathbf{r}}t\right]^n f\left[\mathbf{r}(0),\mathbf{p}(0)\right]\\
&=\sum_{n=0}^{\infty}\frac{1}{n!}\left[\dot{\mathbf{r}}(0)t\right]^n.\frac{\partial^n}{\partial\mathbf{r}^n}f\left[\mathbf{r}(0),\mathbf{p}(0)\right]\\
&=f\left[\mathbf{r}(0)+\dot{\mathbf{r}}(0)t,\mathbf{p}(0)\right],
\end{aligned}$$

and

$$e^{iL_pt}f\left[\mathbf{r}(0),\mathbf{p}(0)\right]=f\left[\mathbf{r}(0),\mathbf{p}(0)+\dot{\mathbf{p}}(0)t\right].$$

Now, from the individual action of iL_r and iL_p we could try to compute the effect of iL but because iL_r and iL_p do not commute $\exp(iL_r+iL_p)\neq\exp(iL_r)\exp(iL_p)$. Therefore we cannot apply the equations for iL_r and iL_p separately. To solve this problem we use the Trotter's expansion Tuckerman (2010):

$$e^{A+B}=\lim_{P\to\infty}\left[e^{A/2P}e^{B/P}e^{A/2P}\right]^P$$

where A and B are non-commuting operators. For finite but large P we have

$$e^{A+B}=\left[e^{A/2P}e^{B/P}e^{A/2P}\right]^P e^{\mathcal{O}(1/P^2)},$$

choosing $A=iL_pt$, $B=iL_rt$ and $\Delta t=t/P$ we obtain

$$e^{(iL_r+iL_p)t}=\left[e^{iL_p\Delta t/2}e^{iL_r\Delta t}e^{iL_p\Delta t/2}\right]^P e^{\mathcal{O}(1/P^2)}.$$

Therefore we can define

$$G(\Delta t)=e^{iL_p\Delta t/2}e^{iL_r\Delta t}e^{iL_p\Delta t/2} \tag{2.9}$$

as the discrete classical propagator. Because each term of the discrete propagator is unitary and the time dependency is symmetrical in this equation it is easy to show that the whole propagation is time-reversible too. More than that, we can notice that the Jacobian of each term is equal to 1 thus the Jacobian of the

entire propagator (the product of the three Jacobian) is unity too. As we have seen before this means that the propagator is area-conserving.

Let us understand how the application of eq.(2.9) works in practice. Given the initial configuration $\mathbf{r}(t)$ and $\mathbf{p}(t)$ the algorithm is like reading eq.(2.9) from right to the left:

1. $\mathbf{p}(t + \frac{\Delta t}{2}) = \mathbf{p}(t) + \frac{\mathbf{F}(t)}{m}\frac{\Delta t}{2}$
2. $\mathbf{r}(t + \Delta t) = \mathbf{r}(t) + \mathbf{p}\left(\frac{\Delta t}{2}\right)\Delta t$
3. Compute $\mathbf{F}(t + \Delta t)$ using $\mathbf{r}(t + \Delta t)$.
4. $\mathbf{p}(t + \Delta t) = \mathbf{p}(t + \frac{\Delta t}{2}) + \frac{\mathbf{F}(t+\Delta t)}{m}\frac{\Delta t}{2}$
5. Go back to (1) with $t \equiv t + \Delta t$.

The algorithm above is known as *Velocity Verlet*. Although Tuckerman et al. (1992) were the first ones to derive this algorithm using the tools of classical mechanics, Verlet (1967) was the first to present the algorithm in this form.

We have formally derived an area-preserving and time-reversible algorithm. We now apply it to the same harmonic oscillator of fig.2.1, using the same initial conditions and parameters. The results are shown in fig.2.2 where we can see that the phase-space (right) is a circle and the energy is conserved (left). Notice the time-scale difference between the figs.2.1 and 2.2, the velocity Verlet simulation is 50 times longer than the Euler method and it still has a better energy conservation than Euler's algorithm.

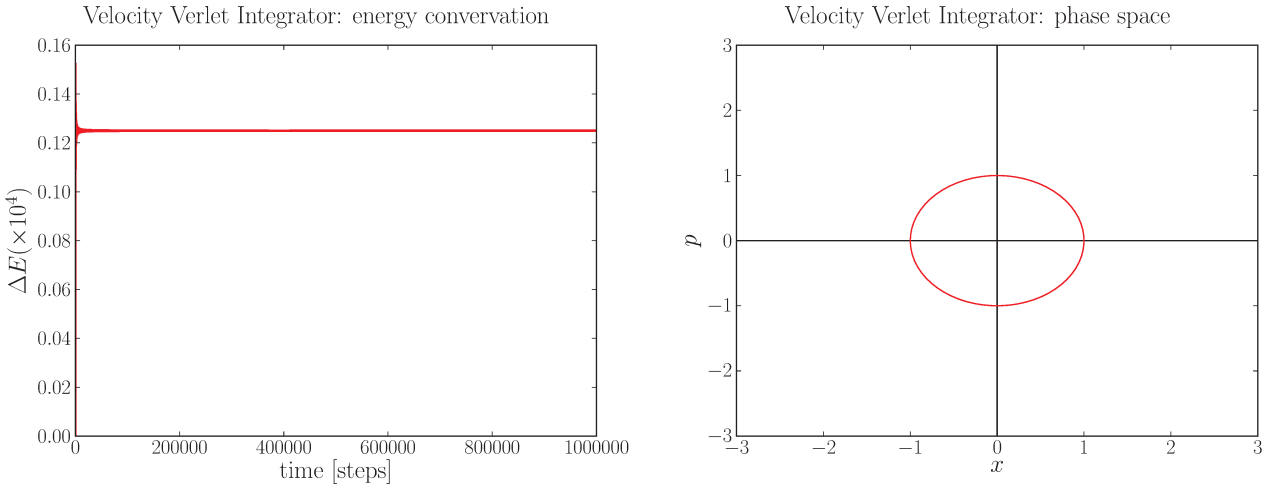

Figure 2.2: Energy conservation (**left**) and phase space (**right**) of a harmonic oscillator solved with the Velocity Verlet integration method.

Now that we know how to numerically integrate the classical equations of motion we can in fact perform an MD simulation and obtain useful data about the system from our simulations. Now comes

the time to analyze such data and understand what they mean physically. In the following section we discuss the connection between MD and statistical mechanics.

2.3 Molecular Dynamics and Statistical Mechanics

Our ultimate goal in running an MD simulation is to obtain useful information about our system capable of helping us to understand and gain insights about it. Because of the atomistic character of MD simulations we deal with a large number of degrees of freedom (positions and velocities of all atoms). Although it seems good to have such a detailed information about the system, frequently we need to convert it into something amenable to brain. There are two different ways of processing the "crude" data from the trajectory generated by our simulation. One of them is to generate smart graphical visualizations of the system. This is a powerful method that allows us, with the help of the correct analysis, to rapidly understand what is happening with our system. For instance the visualization package OVITO (Stukowski, 2010) allows us to perform neighbor analysis of the atoms and distinguish between atoms in different phases. This, for instance, allows us to observe the phenomena of crystallization from a melt.

The second type of processing of the trajectory data is to extract from the huge number of degrees of freedom a small number of specific degrees of freedom that give us important information about our system but are manageable to our limited processing capacity. This task is performed through the use of the connection between statistical mechanics and thermodynamics. The state of a classical system is completely described by the set of position and velocity of all atoms $\Gamma = \{\mathbf{r}^N, \mathbf{v}^N\}$. A given thermodynamical observable $\mathcal{A}$ is computed by taking the thermodynamical limit of averages obtained using statistical mechanics

$$\frac{\mathcal{A}}{N} \equiv \lim_{N,V\to\infty} \frac{\langle A(\Gamma)\rangle}{N} = \lim_{N,V\to\infty} \frac{1}{N} \int \rho(\Gamma) A(\Gamma) d\Gamma$$

where $v = V/N$ is kept constant. $A(\Gamma)$ is the observable variable computed using the microscopic state of the system and $\rho(\Gamma)$ is the probability density of the statistical ensemble compatible with the thermodynamic boundary conditions. The thermodynamical limit is necessary to close the link between statistical mechanics and thermodynamics.

There is a small but important subtlety in the calculation of $\mathcal{A}$ from an MD trajectory. The quantity that we need to compute is

$$\langle A(\Gamma)\rangle = \int \rho(\Gamma) A(\Gamma) d\Gamma. \tag{2.10}$$

Unfortunately, this is not the quantity that we have direct access to in a simulation. During the simulation we collect a set of instantaneous configurations of our system $\Gamma(t) = \{\mathbf{r}^N(t), \mathbf{v}^N(t)\}$ with $0 < t < T$. If we

collect M of these configurations in intervals longer than the correlation time of the system[1] $t_{i+1} - t_i \geq \tau$ then we can form the estimate

$$\overline{A(\Gamma)} \equiv \lim_{t\to\infty} \frac{1}{t} \int_0^t A\left[\Gamma(t)\right] dt \approx \frac{1}{M} \sum_{i=1}^{M} A\left[\Gamma(t_i)\right] \tag{2.11}$$

which is fundamentally different from eq.(2.10). The important link between these two quantities comes from the so called *Ergodic Hypothesis*, which assumes that the simulation time T is long enough so that the system has the necessary time to visit all the phase space states accessible to it. In this condition and further assuming that the dynamics of the system is such that it does not get trapped and locked in a small region of the phase space we can assume that both averages converge to the same value. Therefore, invoking the ergodic hypothesis, an MD simulation computes the ensemble average of eq.(2.10) by the temporal average of eq.(2.11):

$$\boxed{\langle A(\Gamma)\rangle \equiv \overline{A(\Gamma)}} \tag{2.12}$$

thus obtaining an estimate of the thermodynamic observable.

Before finishing the discussion about the statistical-mechanical treatment of the MD trajectories it is worth mentioning a remarkable interaction between modern concepts of classical mechanics and technical aspects of MD simulations by which we can fully appreciate the importance of statistical mechanics in order to obtain significant information from MD simulation.

Consider fig.2.3, in which the system initially at a state $\Gamma(0) = \{\mathbf{r}^N(0), \mathbf{v}^N(0)\}$ is shown as a red dot. Through the natural Hamiltonian evolution of this initial condition the system follows the green trajectory and after a time t it reaches the final state $\Gamma(t) = \{\mathbf{r}^N(t), \mathbf{v}^N(t)\}$. Now suppose that we evolve the system again from $\Gamma(0)$ but at a time $0 < t' < t$ we introduce a small perturbation. For instance it could be a small increment $\delta\mathbf{v}$ in the velocity of one of the particles of the system. Before t' both trajectories (blue and green) coincide but after the small perturbation they diverge such that the final state of the blue trajectory $\Gamma(t) = \{\mathbf{r}'^N(t), \mathbf{v}'^N(t)\}$ is completely different from the final state of the green trajectory. This divergence of trajectories is known to be exponential such that in a small amount of time the state of both trajectories is completely different. This feature of the evolution of classical system is know as *"Lyapunov instability of trajectories"* (Goldstein, 1980).

Now, why is the Lyapunov instability important in MD? At each time step Δt we are storing the state of the system $\Gamma(t) = \{\mathbf{r}^N(t), \mathbf{v}^N(t)\}$ and using it in the next step of the Velocity Verlet integrator.

[1] The correlation time is a measure time necessary for the system to forget about its initial configuration. It can be estimated necessary time for a correlation function

$$C_A(t) = \frac{\langle A(t)A(0)\rangle}{\langle A(0)^2\rangle}$$

to first decay to zero (it can oscillates afterwards).

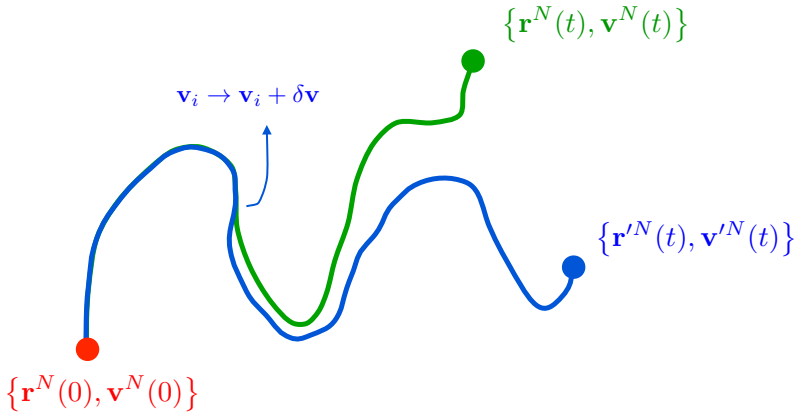

Figure 2.3: *Hamiltonian evolution of a initial state (red dot). The green trajectory is the natural evolution through the Hamiltonian dynamics of the system, the blue trajectory contains a small perturbation during the evolution. The exponentially diverging character of the trajectories is know as Lyapunov instability.*

Because of the limited amount of memory of our computer we cannot save the exact value of, for example, the position of an atom. What we do in practice is to truncate the real value at some point and store the truncated value. In 64-bit machines we usually have about 15 digits of precision plus the exponent. Therefore at each timestep of our MD simulation we are performing some kind of (small) perturbation to our system such way that we can expect that in a short period of time the trajectory of our system will no longer resemble the true trajectory, generated by the true Hamiltonian evolution of the initial conditions.

One may think that this feature might completely destroy the usability of MD simulations, but it is at this point that the statistical mechanics works at its best. Although the collected states of eq.(2.11) do not reflect the states of an actual trajectory they, are statistically uncorrelated collection of states compatible with the simulated ensemble and therefore they are just as good as any other collection of uncorrelated states to compute the average of eq.(2.11). Thus MD is still a safe method to compute averages for thermodynamic observables.

We now turn to the important task of imposing different thermodynamic conditions (temperature, pressure, volume, etc...) on an MD simulation.

2.4 MD in Different Ensembles: Anderson barostat

In the previous section we have shown how to correctly integrate the equations of motion in order to perform an MD simulation. Using the Velocity Verlet integrator one will obtain a trajectory that is compatible with the Hamiltonian dynamics of the system, which means that we are sampling from an ensemble of constant energy E, constant volume V and constant number of particles N, *i.e.* the

microcanonical ensemble. Assuming that the dynamics is ergodic the equilibrium distribution of the system should be the distribution of the microcanonical ensemble

$$\rho_{NVE}(\Gamma) = \frac{\delta[\mathcal{H}(\Gamma) - E]}{\int d\Gamma \delta[\mathcal{H}(\Gamma) - E]},$$

and according to the ergodic hypothesis the long-time average of a observable A is equal to the ensemble average

$$\langle A(\Gamma)\rangle_{NVE} \equiv \overline{A(\Gamma)}.$$

Although there is nothing wrong with this approach it is still clear that there are many applications of MD where one might find it convenient to sample from other ensembles or to have control over thermodynamic parameters other than E, V and N. This section and the next few will be devoted to the discussion of methods often used to implement different ensembles sampling.

We start by considering that our system is coupled to an environment that exerts pressure P on the system and therefore can perform work $W = -P\Delta V$ if the volume V of the system changes. Under these conditions we know that the internal energy E of the system is not conserved, but rather the enthalpy

$$H = E + PV.$$

This condition is described by the NPH ensemble (*isobaric-isenthalpic*). If we consider the system and the barostat together we recover the microcanonical ensemble for a closed system whose total energy $E + PV$ is conserved. This means that the equilibrium distribution should satisfy the microcanonical ensemble

$$\rho_{NPH}(\Gamma, V) = \frac{\delta[E + PV - \mathcal{H}(\Gamma)]}{\int d\Gamma \delta[E + PV - \mathcal{H}(\Gamma)]}.$$

To implement the NPH ensemble in an MD simulation one can use the method known as Andersen's Extended Lagrangian (Andersen, 1980). We follow the approach by Cai (2007). First we describe the volume of the system through three vectors $\mathbf{c}_1$, $\mathbf{c}_2$ and $\mathbf{c}_3$ such that

$$V = (\mathbf{c_1} \times \mathbf{c_2}).\mathbf{c_3} = \det(\mathbf{h})$$

where $\mathbf{h}$ is the matrix composed of the three column vectors $\mathbf{h} = (\mathbf{c_1}|\mathbf{c_2}|\mathbf{c_3})$. Now we define scaled coordinates $\mathbf{s}_i$ for the atoms of the system in such a way that

$$\mathbf{r}_i = \mathbf{h}.\mathbf{s}_i \qquad \Rightarrow \qquad \mathbf{s}_i = \mathbf{h}^{-1}.\mathbf{r}_i.$$

We assume that the simulation cell is a cube, so that $\mathbf{h} = V^{1/3}\mathbb{I}_3$ is diagonal and $\mathbf{r}_i = V^{1/3}\mathbf{s}_i$. Andersen (1980) proposed to include the volume of the system V in the equations of motion allowing it to fluctuate during the dynamics. For this purpose he introduced the Lagrangian for an extended system

$$\mathcal{L}_A = \frac{1}{2}\sum_{i=1}^{N} m_i \left|V^{1/3}\dot{\mathbf{s}}_i\right|^2 - U(V\mathbf{s}) + \frac{1}{2}M\dot{V}^2 - PV \tag{2.13}$$

where $\mathbf{s} = \{\mathbf{s}_i\}$ and M is fictitious mass associated with the simulation box.

To solve the Lagrange's equations of motion

$$\frac{d}{dt}\left(\frac{\partial \mathcal{L}_A}{\partial \dot{\mathbf{s}}_i}\right) = \frac{\partial \mathcal{L}_A}{\partial \mathbf{s}_i}$$
$$\frac{d}{dt}\left(\frac{\partial \mathcal{L}_A}{\partial \dot{V}}\right) = \frac{\partial \mathcal{L}_A}{\partial V}$$

we need to compute

$$\frac{\partial \mathcal{L}_A}{\partial V} = \frac{1}{3V^{1/3}} \sum_{i=1}^{N} m_i \left|\mathbf{s}_i\right|^2 - \frac{\partial U}{\partial V} - P$$
$$\frac{\partial \mathcal{L}_A}{\partial \mathbf{s}_i} = -\frac{\partial U}{\partial \mathbf{s}_i}$$
$$\frac{\partial \mathcal{L}_A}{\partial \dot{V}} = M\dot{V}$$
$$\frac{\partial \mathcal{L}_A}{\partial \dot{\mathbf{s}}_i} = m_i V^{2/3} \dot{\mathbf{s}}_i.$$

Accordingly the modified equations of motion are

$$\ddot{\mathbf{s}}_i = -\frac{2}{3}\frac{\dot{V}}{V}\mathbf{s}_i - \frac{1}{m_i V^{2/3}}\frac{\partial U}{\partial \mathbf{s}_i}$$

and

$$\ddot{V} = \frac{1}{M}\left(P_{\text{Virial}} - P\right) \tag{2.14}$$

where

$$P_{\text{virial}} = \frac{1}{M}\left(\frac{1}{3V}\sum_{i=1}^{N} m_i \left|V^{1/3}\mathbf{s}_i\right|^2 - \frac{\partial U}{\partial V}\right)$$

is the virial pressure of the system (Allen and Tildesley, 1989). Analyzing eq.(2.14), it shows that Andersen's barostat controls the volume of the system by means of a comparison between the virial pressure and the external pressure P. In this way the virial pressure fluctuates around the external imposed pressure P.

Using the Andersen's Lagrangian eq.(2.13) we can obtain the Hamiltonian $\mathcal{H}_A$ of the system, which is given by

$$\mathcal{H}_A = \frac{1}{2}\sum_{i=1}^{N} m_i \left|V^{1/3}\dot{\mathbf{s}}_i\right|^2 + U\left(V\mathbf{s}\right) + \frac{1}{2}M\dot{V}^2 + PV. \tag{2.15}$$

Therefore, along a dynamical trajectory, it is this Hamiltonian that is conserved instead of the enthalpy $H = E + PV$. Although Andersen's equations of motion do not exactly sample the NPH ensemble, Andersen (1980) has shown that the sampling becomes exactly NPH in the limit of large number of particles N such that, for a large enough system, we can compute averages like

$$\overline{A(\Gamma)} \equiv \langle A(\Gamma)\rangle_{NPH} = \frac{\int_0^\infty dV \int d\Gamma A(\Gamma)\delta\left[E + PV - \mathcal{H}(\Gamma)\right]}{\int_0^\infty dV \int d\Gamma \delta\left[E + PV - \mathcal{H}(\Gamma)\right]}$$

and therefore have control over the pressure of the system.

2.5 Canonical Ensemble: Nosé-Hoover Chain thermostat

Now we consider the problem of controlling the temperature of the system. In statistical mechanics when we want to keep our system at a temperature T we couple our system to a heat reservoir at constant temperature T. Although the composed system formed by the system of interest plus the reservoir is still a closed system we assume that the reservoir is large enough that when it transfers or receives heat from the system its temperature does not change. In MD simulations the approach is similar, using the method of the extended Lagrangian introduced by Andersen (1980). We will now show how to obtain the equations of motion for a system at constant temperature T, volume V and number of particles N. If we also wish to control the pressure of the system all we need to do is to include the modifications presented in the last section together with the ones that we present in this section.

If we want to control the temperature T of our MD simulation the first question we need answer is how to compute the temperature in first place. The answer comes from a result from classical statistical mechanics know as *equipartition theorem* which states the following: a classical system described by a Hamiltonian $\mathcal{H}$ in equilibrium at temperature T has average value of $\frac{1}{2}k_BT$ for each harmonic term in $\mathcal{H}$. The reason why this theorem is useful is because the kinetic energy of a classical system

$$K = \frac{1}{2}\sum_{i=1}^{N} m_i \mathbf{v}_i^2$$

is a sum of $3N$ harmonic degrees of freedom, therefore

$$\langle K \rangle = \frac{3N}{2}k_BT \qquad \Rightarrow \qquad T = \frac{1}{3Nk_B}\sum_{i=1}^{N} m_i \left\langle \mathbf{v}_i^2 \right\rangle .$$

We can also use this last relation to obtain a instantaneous kinetic temperature $T(t)$ of the system

$$T(t) = \frac{1}{3Nk_B}\sum_{i=1}^{N} m_i \mathbf{v}_i(t)^2. \tag{2.16}$$

Using the Extended Lagrangian method of Andersen (1980), Nosé (1984) introduced a Lagrangian that results in a set of equations of motion that sample the canonical (NVT) ensemble. To introduce the thermal reservoir that exchanges heat with the system we introduce a new degree of freedom given by the variable s that exchanges heat with the system by scaling its velocities. The extended Lagrangian is

$$\mathcal{L}_N = \frac{1}{2}\sum_{i=1}^{N} m_i s^2 \dot{\mathbf{r}}_i^2 - U(\mathbf{r}^N) + \frac{Q}{2}\dot{s}^2 - g k_B T_{obj} \ln s \tag{2.17}$$

where Q is a mass associated with the thermostat, $g = f + 1$ where $f = 3N$ is the number of degrees of freedom of the system and T_{obj} is the temperature of the heat reservoir that we want impose on our system.

From eq.(2.17) we can obtain the momenta conjugate to $\mathbf{r}_i$ and s

$$\mathbf{p}_i \equiv \frac{\partial \mathcal{L}_N}{\partial \dot{\mathbf{r}}_i} = m_i s^2 \dot{\mathbf{r}}_i$$

and

$$p_s \equiv \frac{\partial \mathcal{L}_N}{\partial \dot{s}} = Q\dot{s}.$$

Then we can construct the Hamiltonian of the system $\mathcal{H}_N$:

$$\mathcal{H}_N = \sum_{i=1}^{N} \mathbf{p}_i.\dot{\mathbf{r}}_i + p_s\dot{s} - \mathcal{L}_N \qquad \Rightarrow \qquad \mathcal{H}_N = \frac{1}{2}\sum_{i=1}^{N} \frac{\dot{\mathbf{p}}_i^2}{m_i s^2} + U(\mathbf{r}^N) + \frac{p_s^2}{2Q} + gk_BT_{obj}\ln s$$

and introducing $\mathbf{p'}_i = \mathbf{p}_i/s$ we obtain

$$\mathcal{H}_N = \sum_{i=1}^{N} \frac{\dot{\mathbf{p}'}_i^2}{2m_i} + U(\mathbf{r}^N) + \frac{p_s^2}{2Q} + gk_BT_{obj}\ln s$$

or

$$\mathcal{H}_N = \mathcal{H}(\mathbf{p'}^N, \mathbf{r}^N) + \frac{p_s^2}{2Q} + gk_BT_{obj}\ln s \tag{2.18}$$

where $\mathcal{H}(\mathbf{p'}^N, \mathbf{r}^N) = \sum_{i=1}^{N} \frac{\dot{\mathbf{p}'}_i^2}{2m_i} + U(\mathbf{r}^N)$. If we perform a simulation using the extended Hamiltonian of eq.(2.18) we will sample the microcanonical ensemble given by the partition function

$$\begin{aligned} Q_N(E) &= \frac{1}{h^{3N}N!}\int d\mathbf{r}^N d\mathbf{p}^N dp_s ds\, \delta(\mathcal{H}_N - E) \\ &= \frac{1}{h^{3N}N!}\int d\mathbf{r}^N d\mathbf{p'}^N dp_s ds\, s^{3N}\delta(\mathcal{H}_N - E) \\ &= \frac{1}{h^{3N}N!}\int d\mathbf{r}^N d\mathbf{p'}^N dp_s ds\, s^{3N}\delta\left[\mathcal{H}(\mathbf{p'}^N, \mathbf{r}^N) + \frac{p_s^2}{2Q} + gk_BT_{obj}\ln s - E\right]. \end{aligned}$$

Using the following property of the delta function

$$\delta\left[f(x)\right] = \frac{\delta(x - x_0)}{|f'(x_0)|},$$

where x_0 is the single root of $f(x)$, we can choose $x \equiv s$ and

$$f(s) \equiv \mathcal{H}(\mathbf{p'}^N, \mathbf{r}^N) + \frac{p_s^2}{2Q} + gk_BT_{obj}\ln s - E.$$

Hence

$$s_0 = e^{-\frac{\beta}{g}\left[\mathcal{H}(\mathbf{p'}^N, \mathbf{r}^N) + \frac{p_s^2}{2Q} - E\right]}$$

with $\beta = k_BT_{obj}$ and

$$f'(x_0) = \frac{g}{\beta}e^{\frac{\beta}{g}\left[\mathcal{H}(\mathbf{p'}^N, \mathbf{r}^N) + \frac{p_s^2}{2Q} - E\right]}.$$

Then the partition functions becomes

$$\begin{aligned}
Q_N(E) &= \frac{1}{h^{3N}N!}\int d\mathbf{r}^N d\mathbf{p'}^N dp_s ds\, s^{3N}\delta\left[\mathcal{H}(\mathbf{p'}^N,\mathbf{r}^N)+\frac{p_s^2}{2Q}+gk_BT_{obj}\ln s - E\right] \\
&= \frac{1}{h^{3N}N!}\int d\mathbf{r}^N d\mathbf{p'}^N dp_s ds\, s^{3N}\delta\left\{s - e^{-\frac{\beta}{g}\left[\mathcal{H}(\mathbf{p'}^N,\mathbf{r}^N)+\frac{p_s^2}{2Q}-E\right]}\right\}\frac{\beta}{g}e^{-\frac{\beta}{g}\left[\mathcal{H}(\mathbf{p'}^N,\mathbf{r}^N)+\frac{p_s^2}{2Q}-E\right]} \\
&= \frac{1}{h^{3N}N!}\int d\mathbf{r}^N d\mathbf{p'}^N dp_s\,\frac{\beta}{g}e^{-\frac{(3N+1)\beta}{g}\left[\mathcal{H}(\mathbf{p'}^N,\mathbf{r}^N)+\frac{p_s^2}{2Q}-E\right]} \\
&= \frac{1}{h^{3N}N!}\int d\mathbf{r}^N d\mathbf{p'}^N\,\frac{\beta}{g}e^{-\frac{(3N+1)\beta}{g}\left[\mathcal{H}(\mathbf{p'}^N,\mathbf{r}^N)-E\right]}\int dp_s e^{-\frac{(3N+1)\beta}{g}\left(\frac{p_s^2}{2Q}\right)} \\
&= C\frac{1}{h^{3N}N!}\int d\mathbf{r}^N d\mathbf{p'}^N\, e^{-\beta\left[\mathcal{H}(\mathbf{p'}^N,\mathbf{r}^N)\right]} \\
&= CQ_{NVT},
\end{aligned}$$

where in the last passage we have used the relation $g = f + 1 = 3N + 1$ and we have also included in C everything that does not depend of $\mathbf{p'}$ or $\mathbf{r}$.

Therefore, if we perform an MD simulation using the Hamiltonian of eq.(2.18) and measure the average value of observables of the form $A(\mathbf{p'}^N,\mathbf{r}^N)$ we obtain:

$$\overline{A(\mathbf{p'}^N,\mathbf{r}^N)} \equiv \left\langle A(\mathbf{p'}^N,\mathbf{r}^N)\right\rangle_{Nose}.$$

However because $A(\mathbf{p'}^N,\mathbf{r}^N)$ does not depend on s or p_s the average resumes to

$$\left\langle A(\mathbf{p'}^N,\mathbf{r}^N)\right\rangle_{Nose} = \left\langle A(\mathbf{p'}^N,\mathbf{r}^N)\right\rangle_{NVT}.$$

Thus we have obtained a method to compute average values of observables $A(\mathbf{p'}^N,\mathbf{r}^N)$ in the canonical ensemble.

Finishing the presentation of the Nosé-Hoover thermostat we introduce a simplification introduced by Hoover (1985). We perform the change of variables $\xi = sp'_s/Q$ in eq.(2.18) and compute the equations of motion for $\mathbf{p}_i$, $\mathbf{r}_i$, ξ and s:

$$\begin{aligned}
\dot{\mathbf{r}}_i &= \frac{\mathbf{p}_i}{m_i} \\
\dot{\mathbf{p}}_i &= -\frac{\partial U}{\partial \mathbf{r}_i} - \xi\mathbf{p}_i \\
\dot{\xi} &= \left(\sum_{i=1}^{N}\frac{\mathbf{p}_i^2}{m_i} - 3Nk_BT_{obj}\right)/Q \\
\frac{\dot{s}}{s} &= \xi
\end{aligned}$$

where in the third equation we can substitute the value of the instantaneous temperature eq.(2.16) and obtain

$$\dot{\xi} = \frac{3Nk_B}{Q}\left[T(t) - T_{obj}\right].$$

This equation shows that the Nosé-Hoover thermostat has a feedback mechanism similar to that for the volume in the Andersen thermostat, eq.(2.14). Measuring the difference between $T(t)$ and T_{obj} the variable ξ change in a way such as to modify the intensity of the viscous drag applied to the particles. In this manner the value of $T(t)$ fluctuates around T_{obj}.

Often the Nosé-Hoover is substituted by a similar thermostat known as Nosé-Hover Chain (Martyna et al., 1992), where instead of one thermostat variable ξ there is a chain of M coupled thermostats ξ_k. The equations of motion then become

$$\begin{aligned}
\dot{\mathbf{r}}_i &= \frac{\mathbf{p}_i}{m_i} \\
\dot{\mathbf{p}}_i &= -\frac{\partial U}{\partial \mathbf{r}_i} - \frac{p_{\xi_1}}{Q_1}\mathbf{p}_i \\
\dot{\xi}_k &= \frac{p_{\xi_k}}{Q_k} \\
\dot{p}_{\xi_1} &= \left(\sum_{i=1}^{N} \frac{\mathbf{p}_i^2}{m_i} - 3Nk_BT_{obj}\right) - \frac{p_{\xi_2}}{Q_2}p_{\xi_1} \\
\dot{p}_{\xi_k} &= \left(\frac{p_{\xi_{k-1}}}{Q_{k-1}} - k_BT\right) - \frac{p_{\xi_{k+1}}}{Q_{k+1}}p_{\xi_k} \\
\dot{p}_{\xi_M} &= \left(\frac{p_{\xi_{M-1}}}{Q_{M-1}} - k_BT\right).
\end{aligned}$$

Then the conserved Hamiltonian is

$$\mathcal{H}_N = \mathcal{H}(\mathbf{p}'^N, \mathbf{r}^N) + \sum_{k=1}^{N} \frac{p_{\xi_k}^2}{2Q_k} + gk_BT_{obj}\xi_1 + \sum_{k=2}^{M} k_BT\xi_k.$$

The reason why this chain is necessary is to reduce the ergodicity problem (Tuckerman, 2010) present when the Nosé-Hoover thermostat is applied to stiff systems like harmonic oscillators. In the next section we will further explore this kind of problem.

2.6 Nosé-Hoover Chain Thermostat and Harmonic Oscillators

Let us now consider the application of the Nosé-Hoover thermostat to a system composed of N identical non-interacting tridimensional harmonic oscillators with spring constant $k = m\omega^2$. Such system is also known as an Einstein crystal because of the interpretation that each harmonic oscillator is an atom of the crystal vibrating harmonically around its equilibrium position.

We can obtain the partition function of the Einstein crystal analytically:

$$\begin{aligned} Z_N &= \frac{1}{(2\pi\hbar)^{3N}} \int e^{-\beta \mathcal{H}(\mathbf{r}^N,\, \mathbf{p}^N)} d\Gamma = \frac{1}{(2\pi\hbar)^{3N}} \left(\int \int e^{-p^2/2mk_BT} e^{-m\omega^2 r^2/2k_BT} d^3r d^3p \right)^N \\ &= \frac{1}{(2\pi\hbar)^{3N}} \left(\sqrt{2m\pi k_BT} \sqrt{\frac{2\pi k_BT}{m\omega^2}} \right)^{3N} = \frac{1}{(2\pi\hbar)^{3N}} \left(\frac{2\pi k_BT}{\omega} \right)^{3N} \\ &= \left(\frac{k_BT}{\hbar\omega} \right)^{3N}. \end{aligned} \tag{2.19}$$

Using this equation we can compute the average of the potential energy and recover the equipartition theorem result:

$$\begin{aligned} \langle U \rangle &= \frac{1}{Z_N} \left[\frac{1}{(2\pi\hbar)^{3N}} \int U(\mathbf{r}^N) e^{-\beta \mathcal{H}(\mathbf{r}^N,\, \mathbf{p}^N)} d\Gamma \right] \\ &= -\left(\frac{k_BT}{\hbar\omega} \right)^{-3N} \left(\frac{k_BT}{\hbar\omega} \right)^{3N/2} \left[\frac{1}{(2\pi\hbar)^{3N/2}} \frac{\partial}{\partial\beta} \int e^{-\beta U} d^{3N}\mathbf{r} \right] \\ &= -\left(\frac{k_BT}{\hbar\omega} \right)^{-3N/2} \left[\frac{\partial}{\partial\beta} \left(\frac{k_BT}{\hbar\omega} \right)^{3N/2} \right] = -\left(\frac{k_BT}{\hbar\omega} \right)^{-3N/2} \left[\frac{\partial}{\partial\beta} \left(\frac{1}{\beta\hbar\omega} \right)^{3N/2} \right] \\ &= \left(\frac{k_BT}{\hbar\omega} \right)^{-3N/2} \left[\frac{3Nk_BT}{2} \left(\frac{1}{\beta\hbar\omega} \right)^{3N/2} \right] \\ &= \frac{3}{2} N k_B T. \end{aligned} \tag{2.20}$$

By a similar calculation we can also obtain the average value of the kinetic energy $\langle K \rangle = \frac{3}{2} N k_B T$. This result is a specific case of the equipartition theorem and it only assumes that the system is in thermal equilibrium at a temperature T. Accordingly, a system of harmonic oscillators provides a good test to check the consistency of the thermostat.

Aside from verifying the equipartition theorem, we can also check if the thermostat correctly samples the canonical ensemble by computing the probability distributions of $(\mathbf{r}^N - \mathbf{r}_0^N)$ (displacement from the equilibrium position) and $\mathbf{p}^N$ (momenta) and compare them to the analytical result. To obtain the analytical results we consider a single harmonic oscillator, because the Einstein crystal is composed of N non-interacting oscillators.

Because the probability distribution of the canonical ensemble is proportional to the Boltzmann factor $e^{-\beta E}$ all we need to do is to correctly normalize the result, therefore

$$\int_{-\infty}^{+\infty} \rho(x) dx = \int_{-\infty}^{+\infty} A e^{-\frac{kx^2}{2k_BT}} dx = A \sqrt{\frac{2\pi k_BT}{k}} = 1 \quad \Rightarrow \quad A = \sqrt{\frac{k}{2\pi k_BT}},$$

and

$$\int_{-\infty}^{+\infty} \rho(v) dv = \int_{-\infty}^{+\infty} B e^{-\frac{mv^2}{2k_BT}} dx = B \sqrt{\frac{2\pi k_BT}{m}} = 1 \quad \Rightarrow \quad B = \sqrt{\frac{m}{2\pi k_BT}}.$$

The final results are

$$\rho(x) = \frac{1}{\sqrt{2\pi k_BT/k}} e^{-\frac{kx^2}{2k_BT}} \quad \text{and} \quad \rho(v) = \frac{1}{\sqrt{2\pi k_BT/m}} e^{-\frac{mv^2}{2k_BT}}. \tag{2.21}$$

We computed the relevant averages using different lengths for the thermostat chain and statistical the errors were computed using the method of block averaging (Krauth, 2006). The system was composed of 1728 tridimensional harmonic oscillators at $T = 700K$. The timestep was chosen $\Delta t = 0.5ps$ and the averages were calculated in a simulation of 10^6 timesteps.

The probability distribution of eqs.(2.21) are shown in fig.2.4. None of the chains lengths correctly sample the exact results. The generated probability distributions assumes a double spiked shape instead of the required Gaussian.

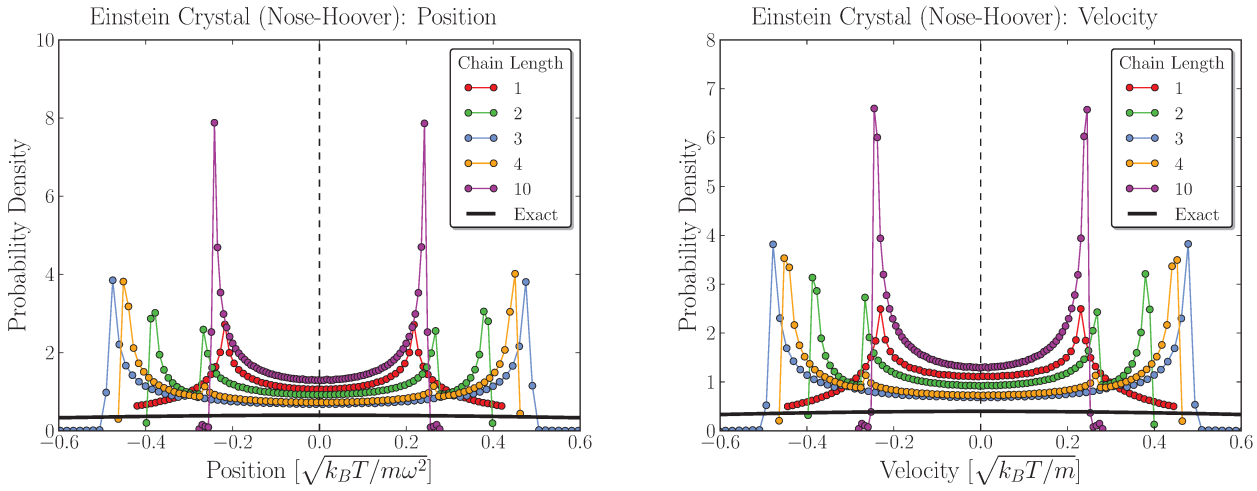

Figure 2.4: Histogram of momentum (**left**) and position (**right**) of particles in a system of harmonic oscillators at constant temperature controlled by a Nosé-Hoover chain thermostat. Different chain lengths were used but none of them agree with the exact result.

The behavior of the probability distribution of position and velocity are also apparent in the probability distributions for the potential and kinetic energy as shown in fig.2.5. None of them correctly reproduces the Gaussian behavior expected, although, for a length of 3 or greater the correct average value of the distribution is obtained.

The results presented here are all well documented in the literature (Tuckerman, 2010; Martyna et al., 1992). One solution to this problem, caused by the stiff nature of the dynamics, it so couple one Nosé-Hoover chain to each degree of freedom of the system, known as *Massive Nosé-Hoover Thermostat* (MNH). Although the MNH solves the problem for stiff systems like harmonic oscillators, it includes the negative consequence of adding many more degrees of freedom to the system. An alternative solution for this problem is to use the Langevin thermostat, to be presented later in this chapter.

During the development of this dissertation we encountered the necessity of thermostatting a system with many similarities to the Einstein crystal, the so called harmonic approximation of a crystal. In next section we present this approximation and show how the Nosé-Hoover thermostat performs in this case.

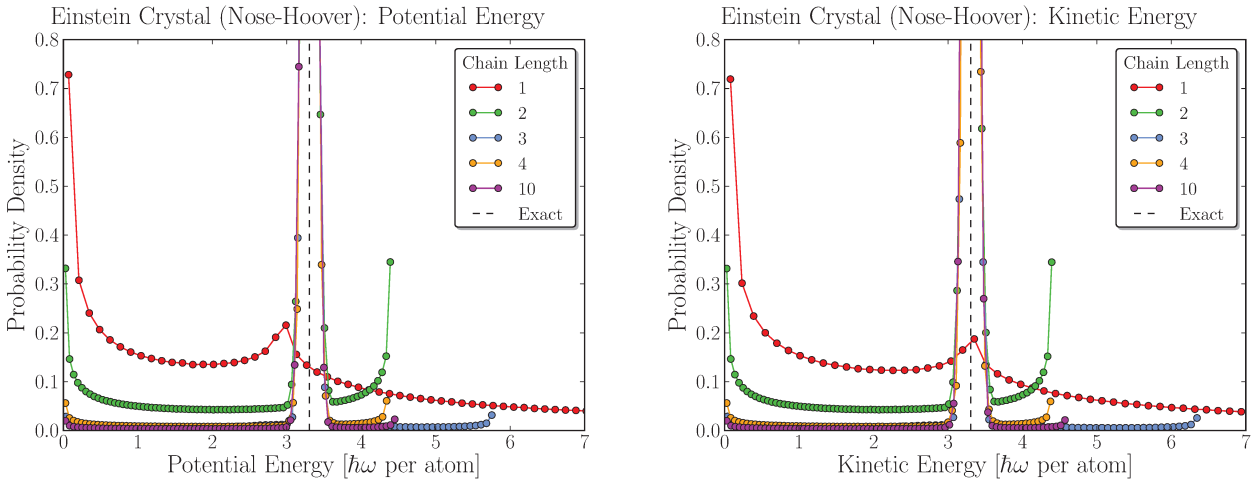

Figure 2.5: Histogram of kinetic (**left**) and potential (**right**) energy of a system of harmonic oscillators at constant temperature controlled by a Nosé-Hoover chain thermostat. Different chain lengths were used but none of them resulted in a Gaussian-like distribution with the correct average.

2.7 Nosé-Hoover Chain Thermostat and the Harmonic Approximation

In this section we discuss the thermostating of an interacting crystal within the harmonic approximation. First, we introduce in detail how to perform the harmonic approximation of a crystal and then we discuss the implications of applying the Nosé-Hoover thermostat to control its temperature.

Consider a crystal composed of N atoms in their equilibrium positions (the total force on each atom is zero) where the interaction between the atoms is described by some interatomic potential. If this crystal is mechanically stable then for small displacements (compared to the first neighbor distance) there will be restoration forces proportional to the displacement. To verify this property we have computed the force on an atom of the system when we apply small displacements to it while keeping all the others in their equilibrium positions. The result for the Meyer and Entel (1998) EAM potential is show in fig.2.6 (left) where we can verify the spring-like behavior (Hooke's law) for small displacements. If we make the approximation that the force acting on this atom is linear in the displacement no matter how large it is then the complete dynamics of the crystal could be described by the spring constants of each atom (in each direction) with respect to displacements of all others. Of course this is only an approximation and it breaks down for large displacements. Indeed, note that if we increase the displacement we can see that for large displacements the behavior diverges from the spring-like, fig.2.6 (right).

We mentioned that if we consider the behavior for small displacements for all atoms we can describe the dynamics of the crystal using only the spring constants of each atom in each direction. For this purpose we start by organizing the forces and spring constants in a matrix form. If F_i are the forces on

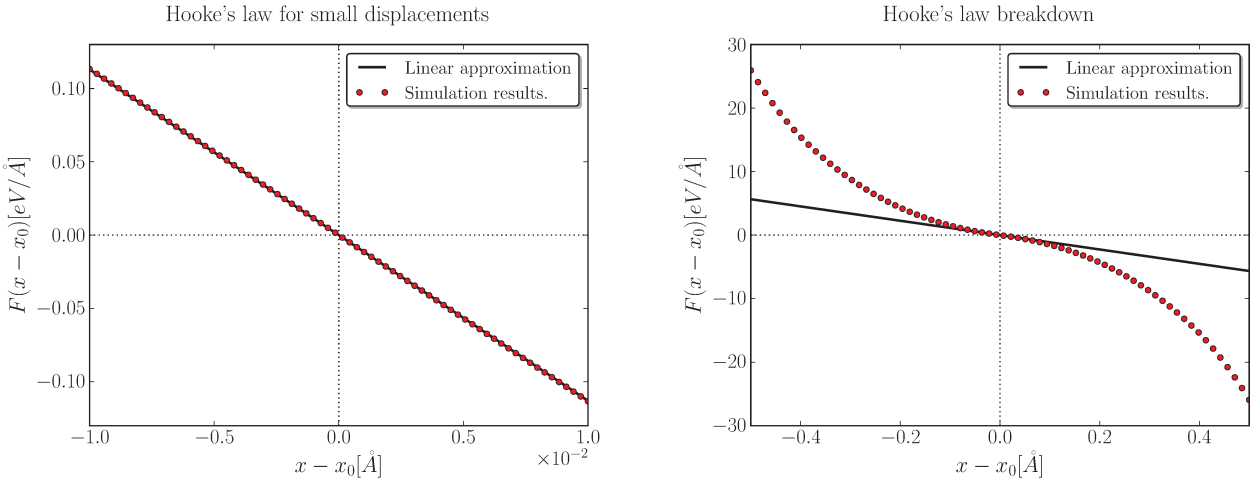

Figure 2.6: Force in one atom for many different displacements from its equilibrium position (all other atoms are keep in their equilibrium position). **Left:** the spring-like behavior (Hooke's law). **Right:** the divergence from this linear behavior for large displacements.

the atoms and q_i are their displacements then we can organize these variables using the spring constant matrix k_{ij}:

$$\begin{bmatrix} F_1 \\ F_2 \\ F_3 \\ F_4 \\ \vdots \\ F_{3N} \end{bmatrix} = - \begin{bmatrix} k_{11} & k_{12} & \dots & k_{1\,3N} \\ k_{21} & k_{22} & \dots & k_{2\,3N} \\ & & & \\ \vdots & \ddots & & \vdots \\ & & & \\ k_{N1} & k_{3N\,2} & \dots & k_{3N\,3N} \end{bmatrix} \begin{bmatrix} q_1 \\ q_2 \\ q_3 \\ q_4 \\ \vdots \\ q_{3N} \end{bmatrix} \quad \Rightarrow \quad \mathbf{F} = -\mathbb{k}.\mathbf{r}, \tag{2.22}$$

where $D_{ij} = k_{ij}/m$ is the dynamical matrix of the system. This matrix completely describes the system within the harmonic approximation. For example, the potential energy $V(\mathbf{r}^N)$ of the crystal in this approximation is given by

$$V(\mathbf{r}^N) = V_0 + \sum_{i,j=1}^{3N} k_{ij}(q_i - q_i^0)(q_j - q_j^0) + \mathcal{O}[(q_i - q_i^0)^3],$$

where q_i^0 are the equilibrium position of the atoms and V_0 is the equilibrium lattice energy. A different way of obtaining the $\mathbf{D}$ matrix is to truncate the Taylor expansion of the potential energy at terms of order 2 in the displacements of the atoms from its equilibrium positions. Then we notice that $\mathbf{D}$ is a Hessian matrix, *i.e.* it can be written as the second order partial derivatives of the potential energy

$$D_{ij} = k_{ij}/m = \frac{1}{m_i}\left(\frac{\partial^2 V}{\partial q_i \partial q_j}\right)_{\{\mathbf{r}_i^0\}}.$$

Because D_{ij} is symmetric we can diagonalize it writing $\mathbf{D} = \mathbf{U}\mathbf{\Omega}\mathbf{U}^T$where $\mathbf{\Omega}$ is the diagonal matrix with the eigenvalues of $\mathbf{D}$ and $\mathbf{U}$ is an unitary matrix ($\mathbf{U}\mathbf{U}^T = \mathbb{I}_{3N\times 3N}$) the columns of which are eigenvectors of $\mathbf{D}$. The eigenvectors and eigenvalues of this matrix are such that $\mathbf{D}.\boldsymbol{\epsilon}_i = \omega_i^2\boldsymbol{\epsilon}_i$, where ω_i are the eigenfrequencies and ϵ_i are the polarization vectors of the corresponding normal mode. Since $\mathbf{D}$ is a $3N \times 3N$ matrix we have $i = 1, 2, \ldots, 3N$. Notice that if we apply a displacement proportional to one of the polarization vectors we have

$$\mathbf{F} = -\mathbb{k}.\boldsymbol{\epsilon}_i = -m\mathbf{D}.\boldsymbol{\epsilon}_i = -m\omega_i^2\boldsymbol{\epsilon}_i \qquad \Rightarrow \qquad \mathbf{F} = -m\omega_i^2\boldsymbol{\epsilon}_i.$$

Therefore the polarization vectors (eigenvectors of the dynamic matrix) are the directions in which the restoration forces point exactly in the opposite direction of the given displacement and has magnitude $m\omega_i^2$.

The dynamic matrix $\mathbf{D}$ is real, symmetric (this result follows directly from the symmetry of Newton's third law) and has dimensions $3N \times 3N$. Hence all its eigenvalues (square of the frequencies of the normal modes) are real and its associated eigenvectors (polarization vectors) form a complete basis of this $3N$-dimensional vector space. Thus if we normalize the eigenvectors properly such that $\boldsymbol{\epsilon}_i^T.\boldsymbol{\epsilon}_j = \delta_{ij}$, we can write any position vector $\mathbf{r}$ of the N atoms as a linear combination of the polarization vectors of the dynamical matrix:

$$\mathbf{r} = \sum_{i=1}^{3N} a_i\boldsymbol{\epsilon}_i \qquad \Rightarrow \qquad \boldsymbol{\epsilon}_j^T.\mathbf{r} = \sum_{i=1}^{3N} a_i\delta_{ij} \quad \Rightarrow \quad a_i = \boldsymbol{\epsilon}_i^T.\mathbf{r}.$$

In this manner the force acting on the atoms in the configuration $\mathbf{r}$ is given by

$$\mathbf{F} = -m\mathbf{D}.\mathbf{r} = -m\mathbf{D}.\sum_{i=1}^{N} a_i\boldsymbol{\epsilon}_i = \sum_{i=1}^{N}(-ma_i\omega_i^2)\boldsymbol{\epsilon}_i \tag{2.23}$$

and the harmonic potential energy of the system is

$$\begin{aligned} V(\mathbf{r}) &= V_0 + \sum_{i,j=1}^{3N} k_{ij}(q_i - q_i^0)(q_j - q_j^0) = V_0 + \frac{1}{2}m\mathbf{r}^T\mathbf{D}\mathbf{r} \\ &= V_0 + \frac{1}{2}m\left(\sum_{i=1}^{3N} a_i\boldsymbol{\epsilon}_i\right)^T \mathbf{D}\left(\sum_{j=1}^{3N} a_j\boldsymbol{\epsilon}_j\right) = V_0 + \frac{1}{2}m\sum_{i,j=1}^{3N} a_ia_j\boldsymbol{\epsilon}_i^T\mathbf{D}\boldsymbol{\epsilon}_j \\ &= V_0 + \frac{1}{2}m\sum_{i,j=1}^{3N} a_ia_j\omega_j^2\boldsymbol{\epsilon}_i^T.\boldsymbol{\epsilon}_j \\ &= V_0 + \sum_{i=1}^{3N}\frac{1}{2}m\omega_i^2a_i^2. \end{aligned} \tag{2.24}$$

In the same way we can write the velocity of the atoms as

$$\mathbf{v} = \frac{d\mathbf{r}}{dt} = \dot{\mathbf{r}} = \sum_{i=1}^{3N}\dot{a}_i\boldsymbol{\epsilon}_i$$

and therefore the kinetic energy of the crystal is given by

$$K(\mathbf{v}) = \frac{m}{2}\mathbf{v}^T.\mathbf{v} = \sum_{i,j=1}^{3N} \frac{m}{2}\dot{a}_i\dot{a}_j\boldsymbol{\epsilon}_i^T.\boldsymbol{\epsilon}_j \quad \Rightarrow \quad K(\mathbf{v}) = \sum_{i=1}^{3N} \frac{m}{2}\dot{a}_i^2. \tag{2.25}$$

With the equations (2.23), (2.24) and (2.25) we can verify that the basis constructed from the polarization vectors of the dynamical matrix gives us harmonic equations for the kinetic and potential energy. Hence the equipartition theorem holds for each normal mode of the crystal in the harmonic approximation. Using a chain of length 4 for the Nosé-Hoover chain thermostat we have performed MD simulations to verify whether it gives us the equipartition of energy between the normal modes of the crystal. The results for the total kinetic and potential energy are shown in fig.2.7. The average values are

$$\text{Equipartition} = 38.740\ meV/atom$$

$$\boxed{\frac{\langle U\rangle_4}{N} = (38.738 \pm 0.034)\ meV/atom \qquad \frac{\langle K\rangle_4}{N} = (38.739 \pm 0.034)\ meV/atom}$$

so at first sight there is nothing wrong with the Nosé-Hoover chain thermostat given that the average value of the potential and kinetic energy seem to respect the equipartition theorem.

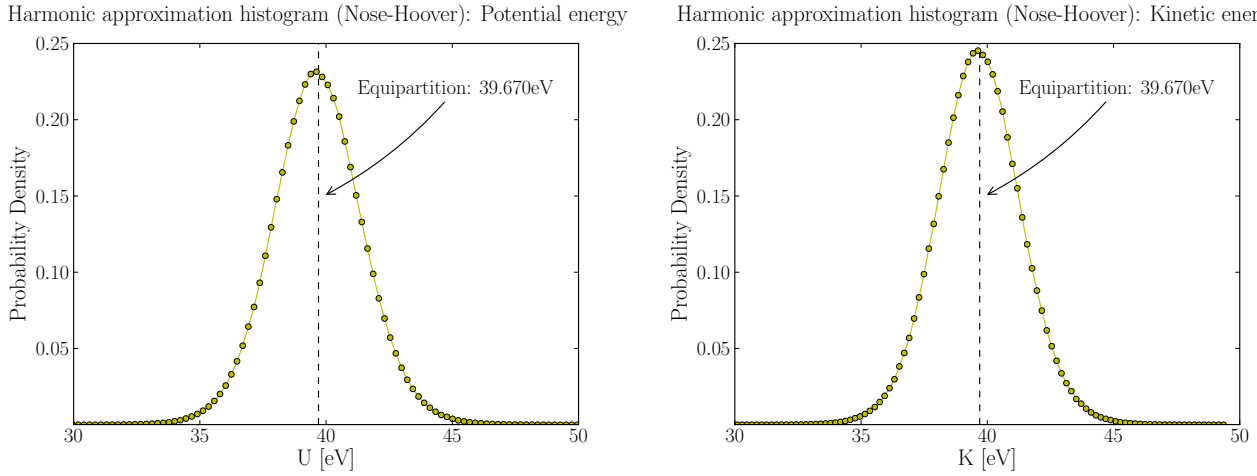

Figure 2.7: Exact probability density of the potential (**left**) and kinetic energy (**right**) of an atom of a crystal under the harmonic approximation, the dotted line is the exact result for the average values predicted by the equipartition theorem.

Let us now analyze the density distribution of position and velocity and compare with eq.(2.21). Fig.2.8 shows the distribution for this system generated by the Nosé-Hoover thermostat. For the case of the velocity we can compare with the exact result and it is clear that the simulation does not agree with the equipartition theorem, for the position all we can say is that it at least presents an Gaussian shape.

To identify the root of the problem we recall that the equipartition theorem is stronger than the version we are using. It asserts that the equipartition of the energy works for *each* harmonic degree of

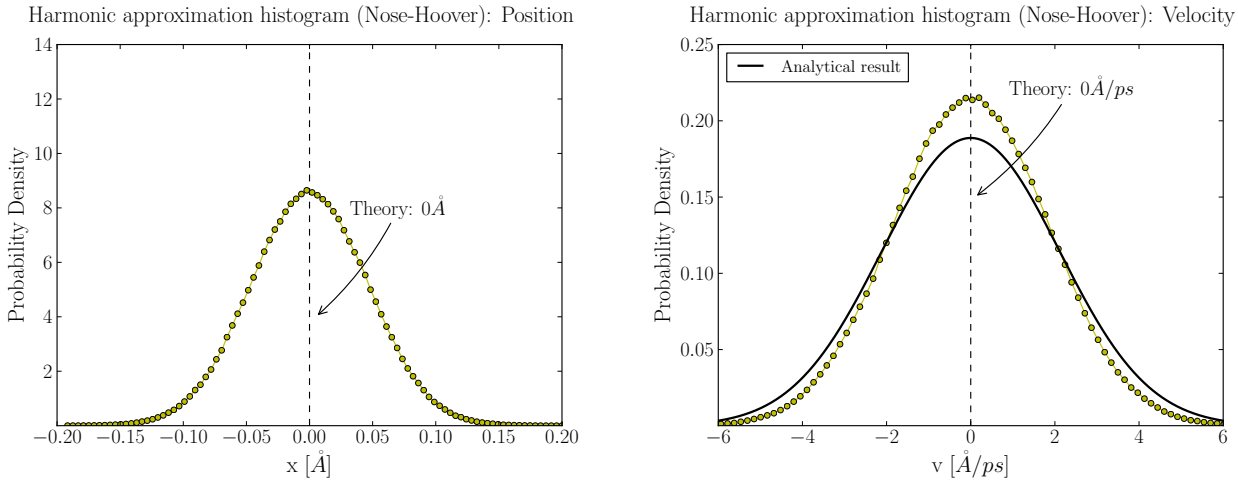

Figure 2.8: Probability density of the position (**left**) and velocity (**right**) of an atom of a crystal under the harmonic approximation, the solid line is the exact result.

freedom of the Hamiltonian, so that the average value of each normal mode (kinetic and potential energy) should have the average value described by the equipartition theorem, eq.(2.20). In fig.2.9 we shown the average value of the kinetic(left) and potential (right) energy for each normal mode of a crystal with 1024 atoms. The yellow solid line shows the expected value according to the equipartition theorem. These two figures demostrate that the Nosé-Hoover chain thermostat does not divide the energy equally between each normal mode. A few of the normal modes are extremely "hot", with an average value of potential and kinetic energy larger than the expected by more than a order of magnitude, while many other modes are almost "frozen", with a mean value of the energy much smaller than expected.

We conclude that the Nosé-Hoover chain thermostat cannot be used to thermostat system with a high degree of harmonicity. This is a problem in many situations, for example when dealing with the harmonic approximation or the Einstein crystal, which are two systems frequently used in the free-energy calculation of solids. Hence we shall look for a thermostat than can correctly equilibrate such stiff systems at a constant temperature.

2.8 Canonical Ensemble: Langevin Thermostat

The Langevin thermostat has a simple interpretation based on Brownian motion. Consider a pollen particle embedded in a fluid (water). The pollen is a large particle $\mathcal{O}(\mu m)$ if compared with the water molecules $\mathcal{O}(nm)$. The collision of a single water molecule does not change the velocity (magnitude and direction) of the pollen particle considerably, but due to the fact that the pollen particle is surrounded by many water molecules it is suffering many collisions in a small time interval. From these incessant

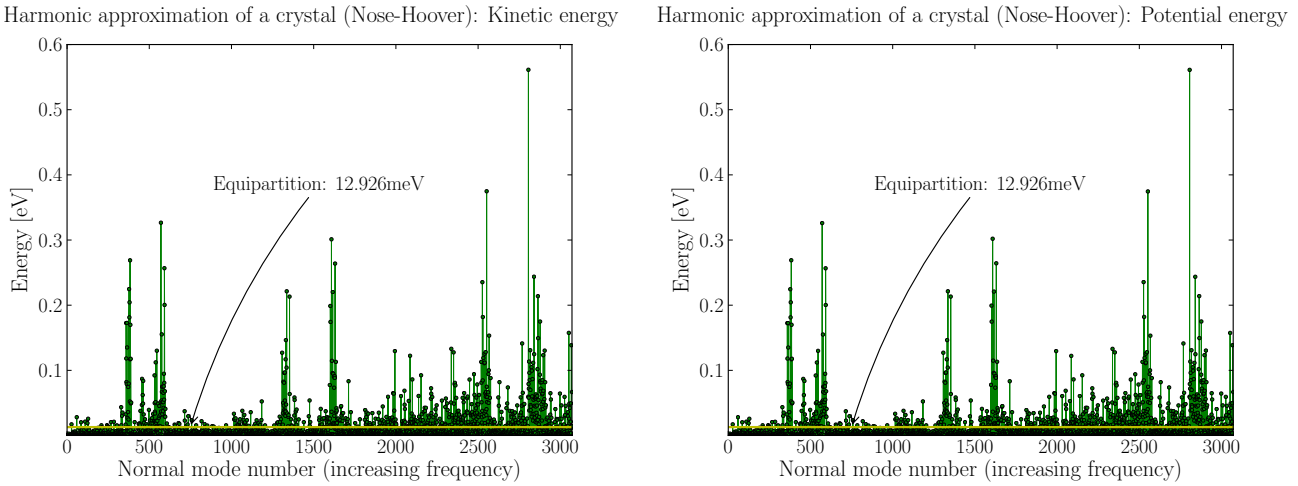

Figure 2.9: Average kinetic (**left**) and potential (**right**) energy of each one of the normal modes of a crystal of 1024 particles. The Nosé-Hoover thermostat does not result in an equally partition of the energy between the normal modes.

collisions the pollen particle changes its velocity and slowly acquires the same temperature of the water, *i.e.* $\langle m_p v^2/2 \rangle = k_B T/2$. The water solution act as a thermal bath to the pollen particle, hitting it all the time in a different directions and with a different intensity such that it sometimes absorbs some of its kinetic energy (acting as a friction force) and sometimes it transfer some kinetic energy to the pollen particle (acting as an impulsive force).

The idea of the Langevin thermostat is to mimic the water solution and keep the system at a constant temperature using random collisions and a viscous force. In order to keep the notation simple we are going to consider the one dimensional case. We introduce two new forces to the equations of motion of the particles of the system

$$f_{fric} = -m\gamma v(t)$$

is the friction force where m is the mass of a atom of the system, $v(t)$ is its velocity and γ is the friction coefficient. In order to balance the friction force we introduce the random impulsive force

$$f_{rand} = R(t)$$

that has the following properties

$$\langle R(t) \rangle = 0$$

and

$$\langle R(t' + t)R(t) \rangle = 2mk_B T\gamma\delta(t) \tag{2.26}$$

where T is the temperature that we wish to impose to our system. This random force is also called a

white noise due to the Dirac's delta correlation and the zero average. This means that the force acting at a time t has no correlation to the force acting at any other time t'. In other words, it has no memory.

The best way to understand why we choose this specific correlation function is to verify that it results in the correct temperature for our system. To simplify the calculations we consider a case where there is no external potential, $U(r) = 0$. The equations of motion are then

$$\begin{aligned} \dot{x}(t) &= v(t) \\ m\dot{v}(t) &= -m\gamma v(t) + R(t). \end{aligned} \tag{2.27}$$

Eq.(2.27) can be multiplied by the integrating factor $e^{\gamma t}$ and integrated, resulting in

$$v(t) = v(0)e^{-\gamma t} + e^{-\gamma t}\int_0^t e^{\gamma t'}\frac{R(t')}{m}dt'.$$

Now if we square this result and take the ensemble average we obtain

$$\left\langle |v(t)|^2 \right\rangle = \left\langle |v(0)|^2 \right\rangle e^{-2\gamma t} + \left(\frac{k_B T}{m}\right)\left(1 - e^{-2\gamma t}\right).$$

Hence in the limit of $t \to \infty$ we obtain

$$\lim_{t\to\infty}\left\langle \frac{1}{2}m\,|v(t)|^2 \right\rangle = \frac{k_B T}{2}.$$

Accordingly this choice the correlation function is justified by the fact that it results in the correct temperature predicted by the equipartition theorem. Notice in eq.(2.26) that the random force magnitude is related to the dissipative force parameter γ, which is a manifestation of the fluctuation dissipation theorem (Cai, 2007).

2.9 Langevin Thermostat Applied to Harmonic Systems

We have already confirmed that the Nosé-Hoover thermostat does not correctly sample the canonical ensemble for stiff (harmonic) systems. Lets now apply the same tests to verify if the Langevin thermostat suffers from the same problem.

First we are going to analyze an Einstein crystal, a system composed of N non-interacting harmonic oscillators. For the same system studied using the Nosé-Hoover thermostat we compute the averages values using a Langevin thermostat coupled to the system now. In fig.2.10 we see that the kinetic and potential energy distributions are Gaussians centered around the value predicted by the equipartition theorem. The average results are

$$\text{Equipartition} = 3.3053\ \hbar\omega/atom$$

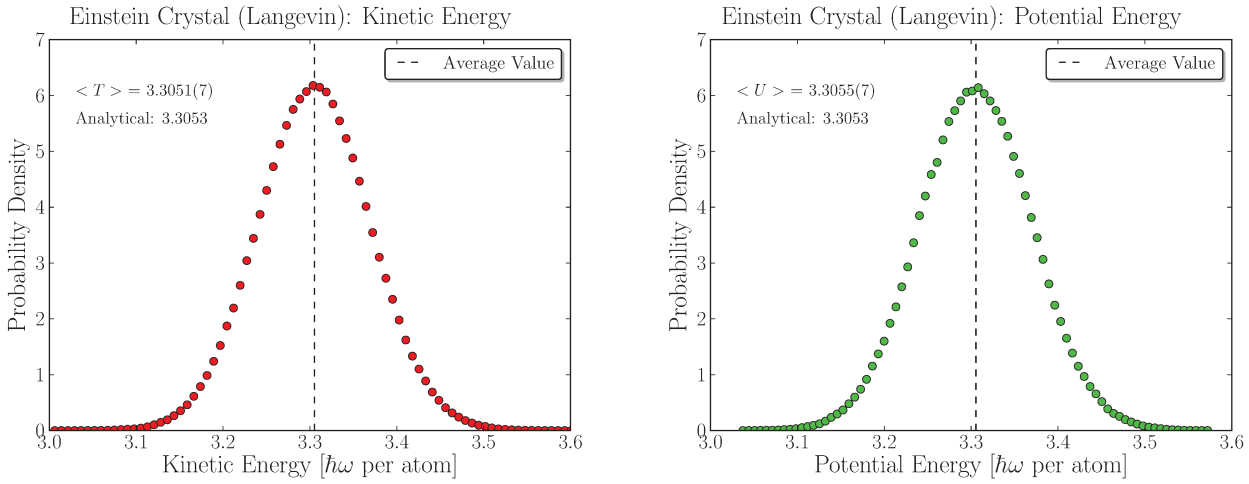

Figure 2.10: Kinetic (**left**) and potential (**right**) energy distribution for an Einstein crystal, the Langevin thermostat does predict average values compatible with the equipartition theorem.

$$\frac{\langle U \rangle}{N} = (3.3055 \pm 0.0007)\ \hbar\omega/atom \qquad \frac{\langle K \rangle}{N} = (3.3051 \pm 0.0007)\ \hbar\omega/atom$$

and we can verify that the Langevin thermostat does obey the equipartition theorem.

In fig.2.11 we verify that the probability density of the position and velocity of a particle agrees with eq.(2.21). The black solid lines describe the analytical distributions and they agree with the distribution computed in the MD simulation. Thus, the Langevin thermostat correctly samples the canonical ensemble for a system of independent harmonic oscillators.

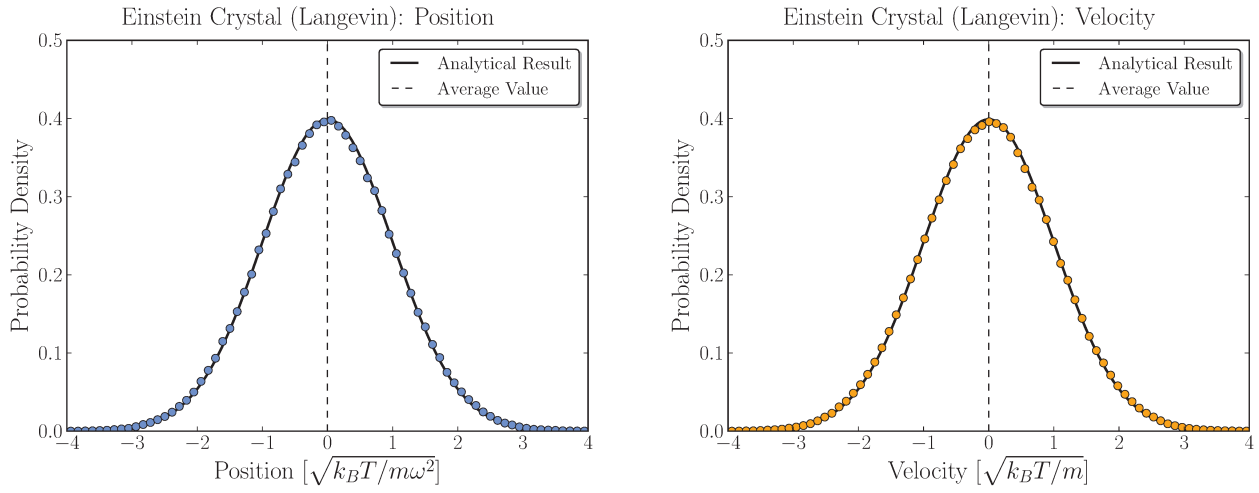

Figure 2.11: Position (**left**) and velocity (**right**) density distribution for an atom of a system composed of harmonic oscillators (Einstein crystal). The black solid line is the analytical result and the dots are the results from the MD simulation, we can verify that the Langevin thermostat correctly sample the canonical ensemble.

Now we turn to the problem of correctly sampling a system given by the harmonic approximation of a crystal. In fig. 2.12 we check the values of the kinetic and potential energy of the system. These are Gaussian distributions with mean values in agreement with the equipartition theorem (within the error bar). The numerical results are

$$\text{Equipartition} = 38.740\ meV/atom$$

$$\boxed{\frac{\langle U\rangle}{N} = (38.730 \pm 0.014)\ meV/atom \qquad \frac{\langle K\rangle}{N} = (38.735 \pm 0.012)\ meV/atom}.$$

In fig.2.13 we show the position and momentum distributions of an atom of this system. The simulation

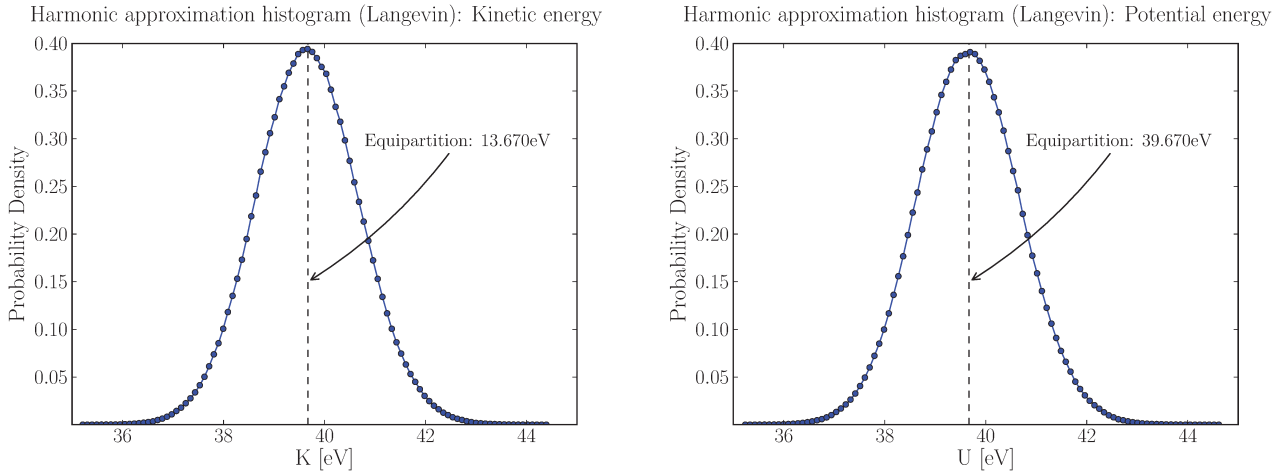

Figure 2.12: Potential (**right**) and kinetics (**left**) energy distribution for the harmonic approximation of a crystal, the Langevin thermostat predicts average values compatible with the equipartition theorem.

results are in agreement with the analytical result (solid black line) for the case of the velocity. Although we do not have the exact result for the position we can see that the distribution is Gaussian.

Finally we turn to the problem of the energy distribution between the normal modes of the crystal. In fig.2.14 we have plotted the average value of the kinetic and potential energy for each normal mode of a crystal with 1024 atoms. Although the error bars had to be estimated because of the difficulty of performing the block average analysis for each point, we can compare this figure with fig.2.9 and verify that the Langevin performs at least one order of magnitude better than the Nosé-Hoover thermostat for all the normal modes. This shows that the Langevin thermostat does correctly distributes the energy between all normal modes.

We conclude that the Langevin thermostat performs better than the Nosé-Hoover chain thermostat for stiff (harmonic) systems. Indeed, it has passed every test we performed to check the correct canonical sampling and we will use it for all further simulations reported in this dissertation.

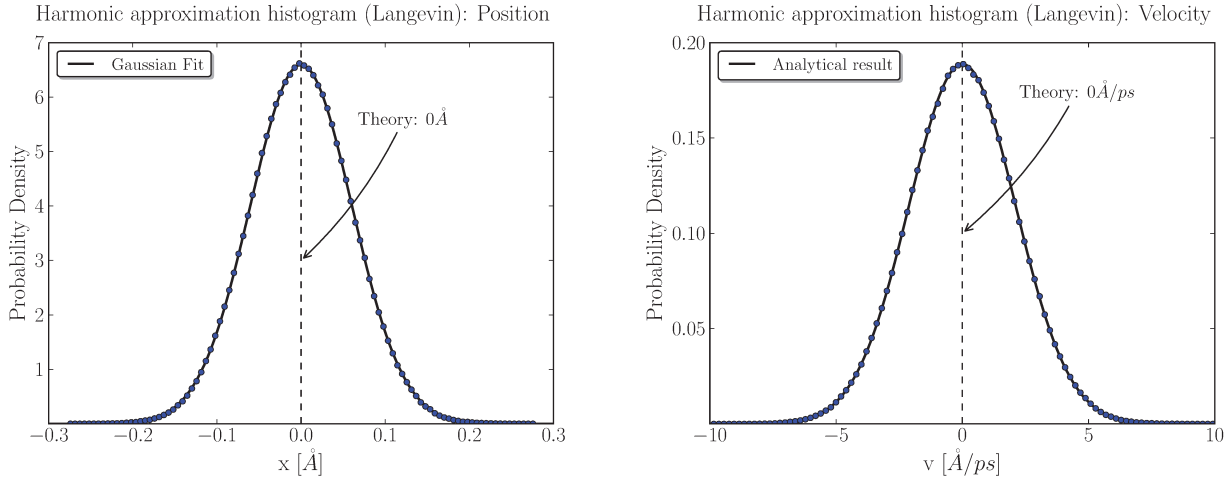

Figure 2.13: Position (**left**) and velocity (**right**) density distribution for an atom of a system that is the harmonic approximation of a crystal. The black solid line is the analytical result in the case of the velocity and a Gaussian fit for the position (there is not analytical result in this case). The dots are the results from the MD simulation, we can verify that the Langevin thermostat correctly sample the canonical ensemble.

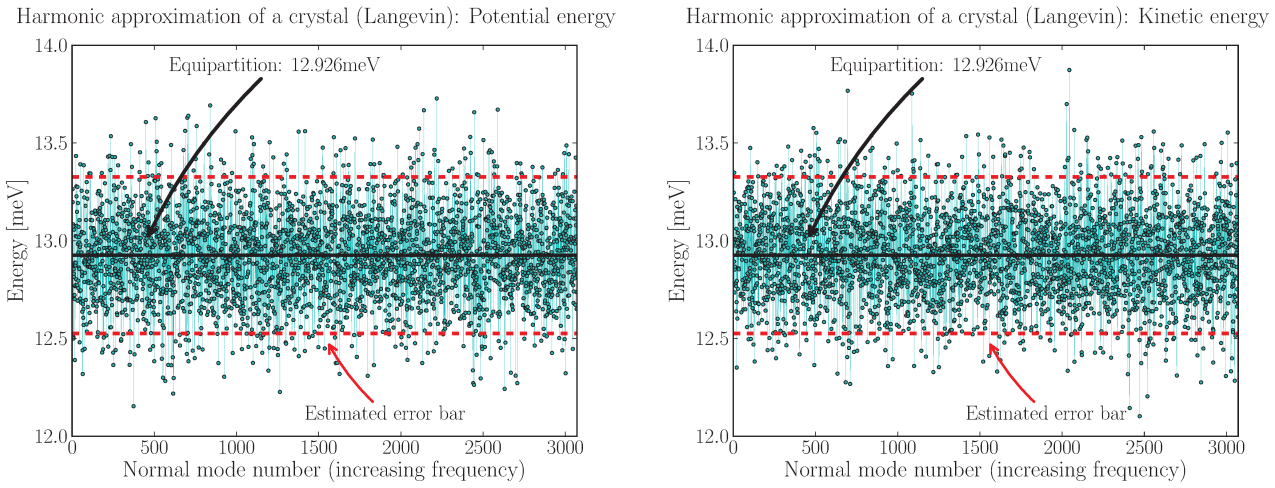

Figure 2.14: Average potential (**left**) and kinetic (**right**) energy of each normal mode of the harmonic approximation of a crystal. The Langevin thermostat results in the correct energy equipartition for each normal mode.

Chapter 3

Phase Transitions and Free-Energy Calculation

In this chapter we present applications of the Molecular Dynamics method to the study of first-order phase transformations. We start by introducing the role of the free energy in the question of the thermodynamic phase stability of a system. Then we present different methods to perform the calculation of free energy using MD. The final objective is to apply these methods to the case of the Martensitic phase transition in iron. Besides the study of the thermodynamics of first-order phase transformations we also want to approach the difficult problem of the kinetics of this phase transformation. We present here a few attempts to study the kinetics using the rare event method know as Forward-Flux Sampling.

3.1 Phase Stability

We start this chapter with a discussion of the phase stability of materials. The problem of phase stability can be stated as follows:

> Given the microscopic description of a material (constituents particles, atoms, molecules and chemical composition) and the thermodynamic conditions under which the material is submitted, what are the characteristics of the spatial arrangement this material will assume? Or, what is the stable phase of this material under these conditions?

This question is at the very core of materials science since the phase of a material define many of its properties and provides profound insights into the behavior of the material. For example, a very specific property of the solid phase is its shear resistance, absent in other phases. A liquid possesses surface tension, a property that controls the wetting characteristics and many other interesting phenomena. Crystalline

translational symmetry gives crystals specific behaviors under X-Ray diffraction that allows studying the atomic arrangements in a crystal and distinguish it from an amorphous solid.

What we need now is a measure for the thermodynamic stability of different phases, *i.e.* given two possible phases of a material and the thermodynamic conditions, how do we measure which one is the "best" phase? What is the property that, when measured, gives us the answer?

We start by analyzing a very simple case, depicted in fig.3.1. In A we have a system surrounded by fixed adiabatic walls, meaning that the system is kept isolated and its internal energy E, volume V and number of particles N are kept constant.

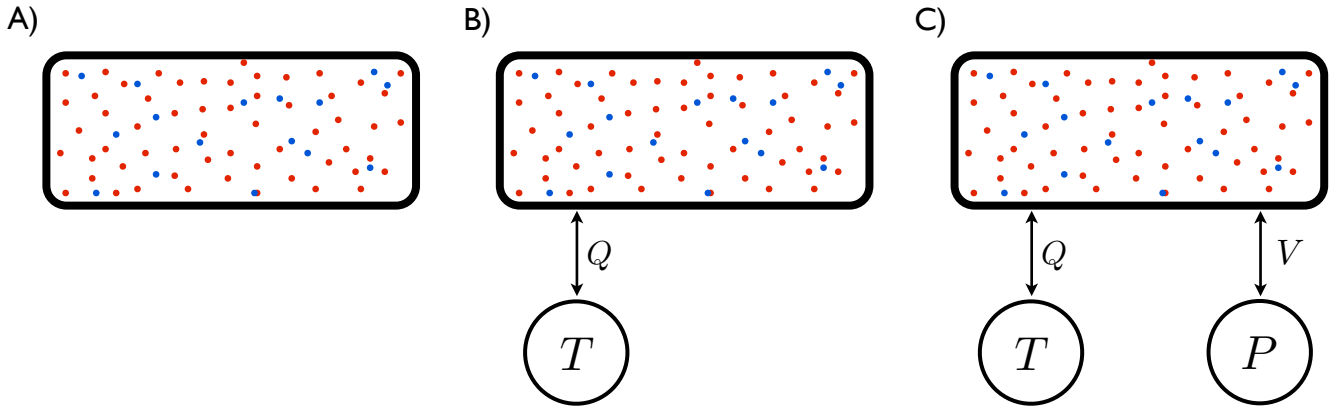

Figure 3.1: A system kept at different thermodynamic conditions. **A)** is isolated and therefore is kept at constant N, V and E. **B)** is in contact with a heat reservoir and therefore has constant N, V and T. **C)** is in contact with a heat reservoir and a "volume" reservoir and thus has constant N, P and T.

We choose a random initial configuration for the material of this system and then we allow it to evolve. From thermodynamics (Callen, 2006) we know that, given enough time, the (Hamiltonian) evolution of the system will naturally lead it to the thermodynamic state of maximum entropy $S(N, V, E)$. Therefore, the most stable phase of this material under the thermodynamic conditions of (N, V, E) constant is the one with maximum entropy:

$$(N, V, E) \qquad \Rightarrow \qquad \max\{S(N, V, E)\}.$$

If we choose as initial condition a different phase with a lower entropy then, given enough time, the system is going to evolve to the phase with maximum entropy. Similarly, if we impose the conditions of (N, V, S) constant, then the most stable phase is the one which minimizes the internal energy.

$$(N, V, S) \qquad \Rightarrow \qquad \min\{E(N, V, S)\}.$$

In this way we have defined functions of thermodynamic variables that are capable of measuring the relative stability of different phases. Although the entropy $S(N, V, E)$ and the internal energy $E(N, V, S)$

are perfectly fine for this process, frequently we are faced with situations where this specific choice of thermodynamic variables is not the most suitable. Often we have situations like fig.3.1 (B) where the system is attached to a heat reservoir that keeps the temperature T of the system constant by exchanging heat Q with it. In this situation the entropy S of the system is not constant due to the heat transfer between the system and reservoir. Therefore, the internal energy is not suitable anymore to measure the relative stability of the phases.

In order to solve this problem we need to perform a Legendre transformation (Callen, 2006) of the function $E(N, V, S)$ to change the dependency from S to T. The result is the so-called Helmholtz free energy

$$F(N, V, T) = E - S\left(\frac{\partial E}{\partial S}\right)_{N,V} = E - TS \qquad \Rightarrow \qquad \min\{F(N, V, T)\}$$

that can be used to measure the relative stability between two different phases subject to a specific temperature T. Now to bring the discussion one step closer to the most frequently encountered conditions of an experiment we also introduce a barostat ("volume" reservoir) that controls the pressure P of the system, as shown in fig.3.1 (C). Performing once again a Legendre transformation we can change the volume variable V of the Helmholtz free energy and obtain the Gibbs free energy

$$G(N, P, T) = F - V\left(\frac{\partial F}{\partial V}\right)_{N,T} = F + PV = E - TS + PV \qquad \Rightarrow \qquad \min\{G(N, P, T)\}$$

Now, given the conditions of constant pressure P, temperature T and number of particles N we know that the most stable phase of a given material is the one that minimizes the Gibbs free energy $G(N, P, T)$. Often we are not able to directly minimize $G(N, P, T)$ due to the huge number of degrees of freedom of atomistic systems, but we still can define different phases and compute the free energy of all of them, the one with the smaller free energy is the most stable.

3.2 MD and Free Energy Calculation: λ-integration method

Now we turn to the problem of computing free energies using MD simulations. In the previous chapter we saw that an MD simulation gives us access to average values of functions of the coordinates and velocities of all particles $(\mathbf{r}^N, \mathbf{v}^N)$ (*e.g.* potential energy, kinetic energy, pressure, correlation functions, radial distribution function, etc...). With the help of the Ergodic assumption these averages can be written as

$$\langle A(\Gamma)\rangle \equiv \overline{A(\Gamma)} = \lim_{t\to\infty} \frac{1}{t} \int_0^t A\left[\Gamma(t')\right] dt'. \tag{3.1}$$

It is clear that from MD simulations one only has access to microscopic variables (coordinates and velocities). Therefore if we want to compute free energies by MD simulations we need to express them as

a function of these variables. This is a case where we need to link thermodynamics with a microscopic theory of matter. This connection is made with the help of statistical mechanics, which asserts that, in the thermodynamical limit, we have

$$F(N,V,T) = -k_B T \ln Z(N,V,T) \tag{3.2}$$

with

$$Z(N,V,T) = \frac{1}{h^{3N}} \int d\Gamma e^{-\beta H(\Gamma)}. \tag{3.3}$$

The partition function for the conditions of fixed N, V and T. Assuming an atomistic system of N particles with Hamiltonian

$$H = \sum_{i=1}^{N} \frac{p_i^2}{2m} + U(\mathbf{r}^N),$$

the kinetic part of the partition function can be solved analytically:

$$\int d^{3N}p \, \exp\left(-\beta \sum_{i=1}^{N} p_i^2/2m\right) = (2\pi m k_B T)^{3N/2} = \left(\frac{h}{\Lambda}\right)^{3N}$$

with $\Lambda = \sqrt{h^2/2\pi m k_B T}$ the thermal de Broglie wavelength. Hence eq.(3.3) becomes

$$Z(N,V,T) = \frac{1}{\Lambda^{3N}} \int d^{3N}r \, e^{-\beta U(\mathbf{r}^N)} = \frac{1}{\Lambda^{3N}} Q(N,V,T),$$

where

$$Q(N,V,T) = \int d^{3N}r \, e^{-\beta U(\mathbf{r}^N)} \tag{3.4}$$

is known as the configurational part of the partition function and does not depend on the velocities of the particles. From eq.(3.2) we obtain for the Helmholtz free energy

$$F(N,V,T) = 3Nk_BT \, \ln\Lambda - k_BT \, \ln Q(N,V,T).$$

Thus in order to compute the free energy we only need to determine is the configurational part of the partition function, eq.(3.4).

Comparing the equation for the configurational part of the partition function, eq.(3.4), to the average values that we can obtain from an MD simulation, eq.(3.1), we see that $Q(N,V,T)$ cannot be written as an average value obtainable from MD. Such quantities, which depend on the total phase-space volume accessible to the system, are known as *thermal properties*. For this reason, we need special techniques to compute free energies from MD simulations.

For this purpose we now introduce a technique known as **Thermodynamical Integration** (TI) or **λ-integration** (Frenkel and Smit, 2001). We start by describing the fundamental idea behind TI. Consider a thermodynamic system with N particles, volume V and temperature T at a state A. If we perform

work W_{AB} on this system (it can be positive or negative) in such a way that its final state is B then, by the second law of thermodynamics, we know that

$$W_{AB} \geq \Delta F \tag{3.5}$$

where ΔF is the Helmholtz free-energy difference between states A and B. The equality in this relation holds only if the work is done in a reversible manner. One way of doing this is to carry out a quasi-static process in which the work is performed slow enough so that that the system follows a path of equilibrium states linking A and B. Now if we can perform work in a controllable manner on our system then we can measure the free-energy difference between the states before and after the work is performed by computing the work done. This is the fundamental idea behind the TI method.

To perform work in a controllable manner we introduce a Hamiltonian that depends on a dimensionless parameter λ: $H \equiv H(\lambda)$. For this system the free energy now has an explicit dependence on λ

$$H \equiv H(\lambda) \qquad \Rightarrow \qquad F(N,V,T;\lambda) = -k_B T \ln\left[\frac{1}{h^{3N}}\int d\Gamma e^{-\beta H(\Gamma;\lambda)}\right].$$

If we compute the derivative of $F(N,V,T;\lambda)$ with respect to λ we obtain

$$\left(\frac{\partial F}{\partial \lambda}\right)_{N,V,T} = \frac{\int d\Gamma \left(\frac{\partial H}{\partial \lambda}\right) e^{-\beta H(\Gamma;\lambda)}}{\int d\Gamma e^{-\beta H(\Gamma;\lambda)}} = \left\langle \frac{\partial H}{\partial \lambda} \right\rangle_{\lambda}$$

where we have used the notation $\langle \ldots \rangle_{\lambda}$ to denote that the average is to be taken in the canonical ensemble at temperature T with Hamiltonian $H(\lambda)$. For brevity we are going to omit the dependency of the free energy on the variables N, V and T in the notation. Now if we integrate both sides of last equation in λ, from λ_A to λ_B where these values of λ characterize the states A and B respectively, we obtain

$$\boxed{F(\lambda_B) - F(\lambda_A) = \int_{\lambda_A}^{\lambda_B} \left\langle \frac{\partial H}{\partial \lambda} \right\rangle_{\lambda} d\lambda}, \tag{3.6}$$

which is the fundamental equation of TI. It expresses the free-energy difference between states A and B in terms of an integral of a quantity that is written as the average value of an observable. This type of average can be easily computed from an MD simulation.

Before finishing this section we would like to present an interpretation of last equation that provides us further insight into TI. If we compare eq.(3.6) with the relation of the second law of thermodynamics, eq.(3.5), we see clearly that the TI equation has exactly the same form as the equality in the second law: it relates a free-energy difference to reversible work. This observation leads us to interpret the right-hand side of eq.(3.6) as the quasi-static work necessary to bring the system from state A to B

$$W_{AB}^{qs} = \int_{\lambda_A}^{\lambda_B} \left\langle \frac{\partial H}{\partial \lambda} \right\rangle_{\lambda} d\lambda = \int_{\lambda_A}^{\lambda_B} f_{\lambda} d\lambda \tag{3.7}$$

where we have associated a generalized force f_λ due to the change in λ

$$f_\lambda \equiv \left\langle \frac{\partial H}{\partial \lambda} \right\rangle_\lambda .$$

Another way to see why eq.(3.7) represents the quasi-static work done by f_λ between states A and B is to analyze how we use MD to compute W_{AB}^{qs}. What we need to do is to compute numerically the integral in eq.(3.7). In order to do that it is necessary to obtain the value of the average $\langle \ldots \rangle_\lambda$ for a certain number of intermediate λ_i values between λ_A and λ_B, as shown in fig.3.2. This number should be large enough so that the integral convergence is satisfactory. At each value of λ_i we have to run one MD

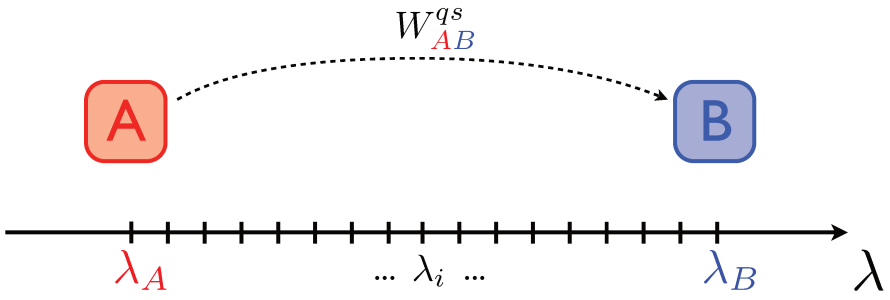

Figure 3.2: Illustration of the Thermodynamic Integration method. States A and B are characterized by the values λ_A and λ_B of the λ parameter. Intermediate values λ_i have to be numerous enough so that the integral convergence is satisfactory.

simulation, equilibrate the system and only then compute the average $\langle \ldots \rangle_\lambda$. This means that each value of the generalized force f_λ is computed in a state of thermodynamic equilibrium and therefore the work of eq.(3.7) is computed using a succession of equilibrium states. This characterizes a quasi-static process and therefore eq.(3.7) represents the quasi-static work done, which, by definition, is reversible.

3.3 Adiabatic Switching

In this section we present a more efficient approach to the implementation of the TI method. Although the method works just fine as we have stated, it can be computationally expensive in practice because of the need to perform one MD simulation for each value of λ_i intermediate between λ_A and λ_B. By means of the Adiabatic Switching (AS) method, proposed by Watanabe and Reinhardt (1990), we eliminate the necessity of one equilibrium MD simulation for each λ_i and obtain an estimate of W_{AB}^{qs} from only a few non-equilibrium MD simulations, increasing the efficiency of the TI significantly.

Instead of doing one equilibrium MD simulation for each intermediate value of λ_i we carry out a single MD simulation in which $\lambda \equiv \lambda(t)$ varies with time. If we start the simulation at a time $t = 0$ and finish

it at $t = t_{sim}$ we choose $\lambda(t = 0) = \lambda_A$ and $\lambda(t = t_{sim}) = \lambda_B$. With the introduction of this temporal dependency we compute the dynamical work done during the simulation as

$$W_{AB}^{dyn} = \int_0^{t_{sim}} \dot{\lambda}(t) \frac{\partial H}{\partial \lambda}\bigg|_{\lambda(t)} dt \tag{3.8}$$

where $\frac{\partial H}{\partial \lambda}$ is the instantaneous value evaluated at t and not an average. Notice that we have introduced the notation W_{AB}^{dyn}, which is the *dynamical* work performed between A and B and differs fundamentally from W_{AB}^{qs}. Now that the process is not performed in equilibrium at each step, the equality of the second law, eq.(3.5), no longer holds. Due to the intrinsic non-equilibrium nature of this process we have dissipative entropy production characteristic of irreversible processes. This means that our estimate for ΔF will have a systematic error besides the statistical error associated with the limited sampling. The systematic error is not associated with the statistical nature of our measurements. Instead it is associated with the dissipation of the irreversible process. We can write it as

$$W_{AB}^{dyn} = W_{AB}^{qs} + Q_{AB} \tag{3.9}$$

where Q_{AB} is the dissipation in the process that goes from state A to state B. Furthermore, according to the second law $Q_{AB} \geq 0$.

To eliminate the systematic bias Q_{AB} we would have to set $t_{sim} \to \infty$, in which case eq.(3.8) becomes exactly equivalent to eq.(3.7) and we recover the quasi-static nature of the reversible process. Because this limit is always unattainable in practice due to the limited amount of computational time we present here a different solution (de Koning and Antonelli, 1997) to eliminate or at least reduce the effect of the dissipation drastically. Consider the work done during the inverse process of bringing the system from state B back to state A. In this case, the dynamical work is given by

$$W_{BA}^{dyn} = W_{BA}^{qs} + Q_{BA} = -W_{AB}^{qs} + Q_{BA}. \tag{3.10}$$

If we perform the forward, eq.(3.9), and the backward, eq.(3.10), processes slow enough that linear-response theory is valid we have that $Q_{AB} = Q_{BA}$, which allows eliminating the systematic error by combining the forward and backward results:

$$W_{AB}^{qs} = \frac{W_{AB}^{dyn} - W_{BA}^{dyn}}{2}. \tag{3.11}$$

In fig.3.2 we illustrate this procedure. We start with our system equilibrated at the state A (λ_A). Then, by defining a function $\lambda(t)$ we compute the forward work W_{AB}^{dyn} to bring the system to state B. After that, we equilibrate the system at the state B (λ_B) and using the same function in the reverse order to compute the backward work W_{AB}^{dyn}. The equilibrium free-energy difference is then computed using eq.(3.11)

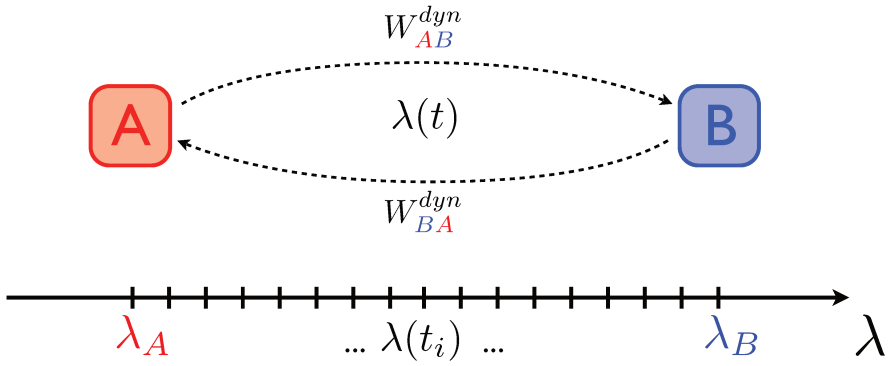

Figure 3.3: Illustration of the Adiabatic Switching method. States A and B are characterized by the values λ_A and λ_B respectively of the $\lambda(t)$ parameter.

Now that we have described the method for computing free energies we are going to present a few applications to specific cases.

3.4 Frenkel-Ladd Method

The Frenkel-Ladd method (Frenkel and Ladd, 1987) is a specific application of the TI method, eq.(3.6), suited to compute free-energy of crystals. Assume we want to compute the free-energy of a crystal in which the atoms interact through a Hamiltonian

$$H_{int} = \sum_{i=1}^{N} \frac{p_i^2}{2m} + U_{int}(\mathbf{r}^N).$$

Now we define another Hamiltonian describing a set of N tridimensional harmonic oscillators of angular frequency ω and spring constant $k = m\omega^2$

$$H_{harm} = \sum_{i=1}^{N} \frac{p_i^2}{2m} + U_{harm}(\mathbf{r}^N) = \sum_{i=1}^{N} \frac{p_i^2}{2m} + \sum_{i=1}^{N} \frac{m\omega^2}{2}(\mathbf{r}_i - \mathbf{r}_i^0)^2 \tag{3.12}$$

where $\mathbf{r}_i^0$ is the equilibrium position of the ith atom of the crystal given by H_{int}. In other words, H_{harm} defines a set of independent harmonic oscillators that have equilibrium positions equal to those of the crystal that we are considering.

The Frenkel-Ladd method consists, basically, of defining the $H(\lambda)$ Hamiltonian used in the TI method as a linear interpolation between the two presented Hamiltonians:

$$H(\lambda) = (1 - \lambda)H_{harm} + \lambda H_{int}.$$

Then if $\lambda_A = 0$ and $\lambda_B = 1$ we have

$$H(\lambda_A) = H_{harm} \qquad \text{and} \qquad H(\lambda_B) = H_{int}.$$

To complete eq.(3.6) we need to compute the derivative of $H(\lambda)$,

$$\frac{\partial H}{\partial \lambda} = H_{int} - H_{harm} = U_{int}(\mathbf{r}^N) - U_{harm}(\mathbf{r}^N) \equiv U_{int} - U_{harm}.$$

Then from eq.(3.6) we have

$$F_{int}(N,V,T) = F_{harm}(N,V,T) + \int_0^1 \langle U_{int} - U_{harm}\rangle_\lambda \, d\lambda. \tag{3.13}$$

$F_{harm}(N,V,T)$ is the free energy of a set of N independent tridimensional harmonic oscillators and we can compute it analytically. The partition function is

$$\begin{aligned}
Z_{harm}(N,V,T) &= \frac{1}{(2\pi\hbar)^{3N}} \int d\Gamma \exp\left(-\beta H_{harm}\right) \\
&= \frac{1}{(2\pi\hbar)^{3N}} \left[\int_{-\infty}^{+\infty} \exp\left(-\beta p^2/2m\right) dp \int_{-\infty}^{+\infty} \exp\left(-\beta k x^2/2\right) dx\right]^{3N} \\
&= \frac{1}{(2\pi\hbar)^{3N}} \left[\sqrt{2\pi m k_B T}\sqrt{\frac{2\pi k_B T}{m\omega^2}}\right]^{3N} \\
&= \left(\frac{k_B T}{\hbar\omega}\right)^{3N},
\end{aligned}$$

giving a Helmholtz free energy

$$F_{harm}(N,V,T) = 3N k_B T \ln\left(\frac{\hbar\omega}{k_B T}\right). \tag{3.14}$$

The desired free energy then

$$\boxed{F_{int}(N,V,T) = 3N k_B T \ln\left(\frac{\hbar\omega}{k_B T}\right) + \int_0^1 \langle U_{int} - U_{harm}\rangle_\lambda \, d\lambda}. \tag{3.15}$$

In eq.(3.15) we recognize the work computed using an MD simulation as $W_{AB}^{qs} = \int_0^1 \langle U_{int} - U_{harm}\rangle_\lambda \, d\lambda$. To improve the precision of the result obtained it is important to compute this value as accurately as we can. If we want to reduce the statistical error of the $\langle \ldots \rangle_\lambda$ present in this integral we can choose the spring constant (or the angular frequency) of the springs in such a way that both systems, the crystal of interest and the set of harmonic oscillators, have values of U_{int} and U_{harm} that are always close. This means that we are choosing the system of reference (harmonic oscillators) as close as possible to the system of interest (crystal). One way to do that proposed by Frenkel and Ladd (1987) is to impose that the root-mean square displacements of the atoms in both systems are equal. Using the theorem of the equipartition of energy we have

$$\frac{m\omega^2}{2}\left\langle \Delta r^2 \right\rangle = \frac{3}{2} k_B T \qquad \Rightarrow \qquad \omega = \sqrt{\frac{3k_B T}{m\left\langle \Delta r^2 \right\rangle}}. \tag{3.16}$$

There is one small technical detail with eq.(3.15), although it is correct when we perform an MD simulation in which we naturally constrain the center of mass of the system of harmonic oscillators. In

order to not find a divergence in the integral to be computed we should also constrain the center of mass of the crystal. We have to account for this constrain in the final result because in practice we are measuring $\langle \ldots \rangle_\lambda^{CM}$ instead of $\langle \ldots \rangle_\lambda$. Polson et al. (2000) have shown how to perform this correction, which is fundamentally a finite-size correction (in the thermodynamical limit the correction vanishes). Here we only state the final result:

$$F_{int}(N,V,T) = 3Nk_BT \ln\left(\frac{\hbar\omega}{k_BT}\right) + \int_0^1 \langle U_{int} - U_{harm}\rangle_\lambda^{CM}\, d\lambda + k_BT \ln\left[\frac{N}{V}\left(\frac{2\pi k_BT}{Nm\omega^2}\right)^{3/2}\right].$$

All results using the Frenkel-Ladd method presented here include this correction.

3.5 Frenkel-Ladd: Harmonic Oscillators

We apply the Frenkel-Ladd method to an Einstein crystal (de Koning and Antonelli, 1996): a crystal in which all atoms vibrate with the same frequency around their equilibrium positions. The vibrations are those of independent harmonic oscillators. In practice we are performing a TI between two sets of harmonic oscillators with different angular frequencies ω_A and ω_B. Because of the possibility of comparing our results to the exact values this allow us to show how the TI and the AS work in practice.

Our Einstein crystal is prepared in a $12 \times 12 \times 12$ simple cubic crystalline structure, this results in 1728 atoms or 5184 independent unidimensional harmonic oscillators. The initial state A is defined as the one with $k_A = m\omega_A^2 = 10\, eV/\mathring{A}$ and B is $k_B = m\omega_B^2 = 50\, eV/\mathring{A}$ where the mass is chosen as $m = 55.847\, g/mol$. We have used the iron atomic mass in order to bring the frequencies closer to the real ones in iron. Technically this is only important to keep an idea of the order of magnitude of the involved numbers. The $\lambda(t)$ variation with t is chosen to be linear. Because of the thermostatting problem encountered in Chapter 2 we use Langevin thermostat. The timestep used was $\Delta t = 0.5 fs$.

First of all we are going to check the convergence of the AS method. According to eq.(3.9) we should expect the dynamical work to have a systematic error associated with the dissipative entropy production. Thus we have performed several AS simulations between the two sets of harmonic oscillators using the arbitrary value of $N_{sim} = t_{sim}/\Delta t = 5000$ steps and a temperature of $T = 100K$, each one with a different initial condition. From these simulations we have computed the estimative for W_{AB}^{qs}, the dynamical work W_{AB}^{dyn}. The exact value of the quasi-static work, given by eq.(3.14) is

$$W_{AB}^{qs} = \Delta F = 3k_BT \ln\left(\frac{\omega_B}{\omega_A}\right) \approx 20.79\, meV/atom. \tag{3.17}$$

In fig.3.4 (left) we confirm that indeed our estimate contains a systematic error $Q_{AB} = 0.46 \pm 0.01\, meV$, showing that the dynamical work converges to a wrong value of W_{AB}^{qs} even when the statistical error is suppressed to a negligible value.

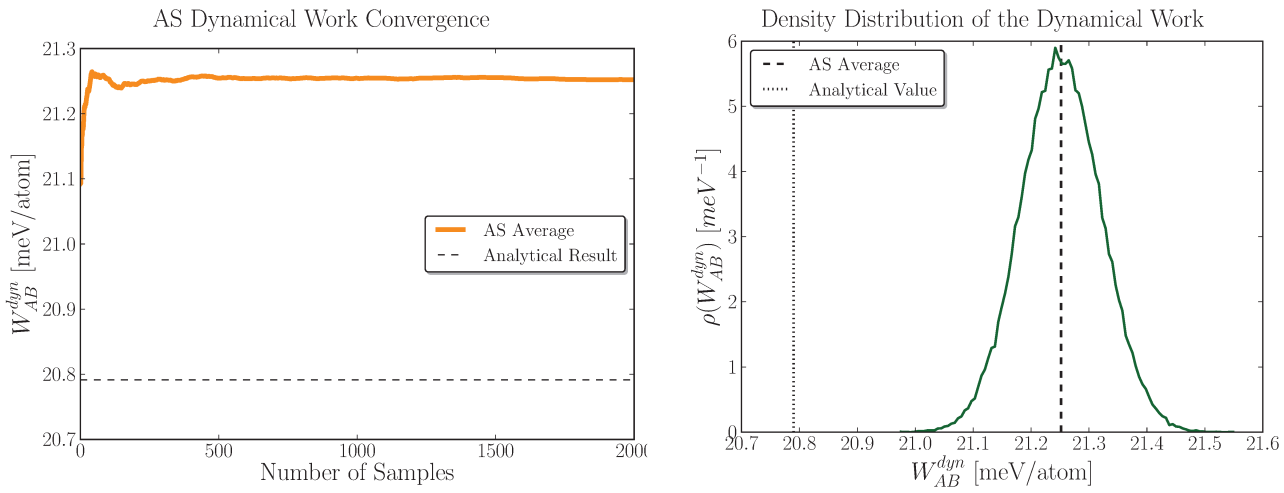

Figure 3.4: **Left:** Convergence of average dynamical work in a AS between two sets of harmonic oscillators. The systematic error persists even after the statistical error is negligible. The dissipative entropy production results in a $Q_{AB} = 0.46 \pm 0.01\, eV/atom$ difference between the exact quasi-static value and the computed dynamical value. **Right:** W_{AB}^{dyn} histogram show the effect of the statistical error (width of the distribution) and the systematic error (displacement of the average value).

It is important to notice that the statistical uncertainty is still present in the computation. If we compute the histogram of W_{AB}^{dyn} we see that the effect of the finite switching time in the AS method is to displace the average value to higher values (due to the systematic error) but there is also a finite width in the distribution of values, fig.3.4 (right), characteristic of statistical errors. In the end, the statistical error may be reduced to any level by increasing the number of samples.

To eliminate the systematic error from W_{AB}^{dyn} we perform the backward simulation and apply the hysteresis procedure of eq.(3.11), to obtain a better estimate for ΔF. In fig.3.5 (left) we compare the estimate for ΔF with the analytical value with increasing switching time. We notice the rapid convergence of the result with the increase of the switching time. Using the exact result provided by eq.(3.14) we can compute the remaining systematic error after the hysteresis procedure as

$$E_{systematic} = W_{AB}^{qs} - 3k_BT \ln\left(\frac{\omega_B}{\omega_A}\right),$$

In fig.3.5 (right) we show how this error vanishes as we increase the switching time.

Both results presented in fig.3.5 are consistent with our interpretation of the AS method as a non-equilibrium process. As we increase the switching time t_{sim} the AS method gets closer and closer to the reversible process of the TI method and therefore our estimate for ΔF should get closer to the quasi-static process and, consequently, $E_{systematic}$ should vanish. These results confirm that the method of AS, eq.(3.8), and the method of TI, (3.7), indeed agree in the limit of $t_{sim} \to \infty$.

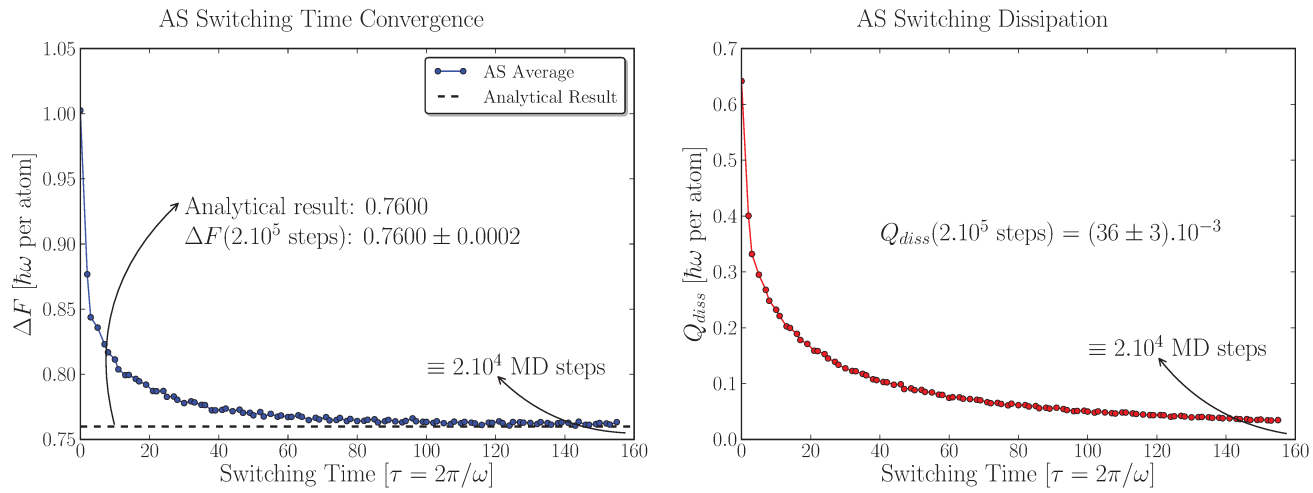

Figure 3.5: **Left**: Convergence of the estimate for the free energy as we increase the switching time t_{sim}. **Right:** Dissipation of the AS process vanishes as we increase the switching time. Error bars are not visible in this scale.

Once we know about the convergence of the AS process we can compute the dependence of the free energy on the temperature. The exact value for the dependence of the reversible work on the temperature has been computed using eq.(3.17). The simulation results are presented in fig.3.6 (left). We have used the hysteresis procedure to eliminate the dissipation and, based on fig.3.5, we chose to perform 10 simulations (forward and backward) of $N_{sim} = 2\times10^5$ steps. The results are shown in fig.3.6 (right). It is interesting to notice that fig.3.6 (right) contains regions of positive and zero derivative at low temperatures, referent to negative and zero entropy. At this limits of low temperature quantum mechanics is necessary to correctly describe the behavior of a crystal.

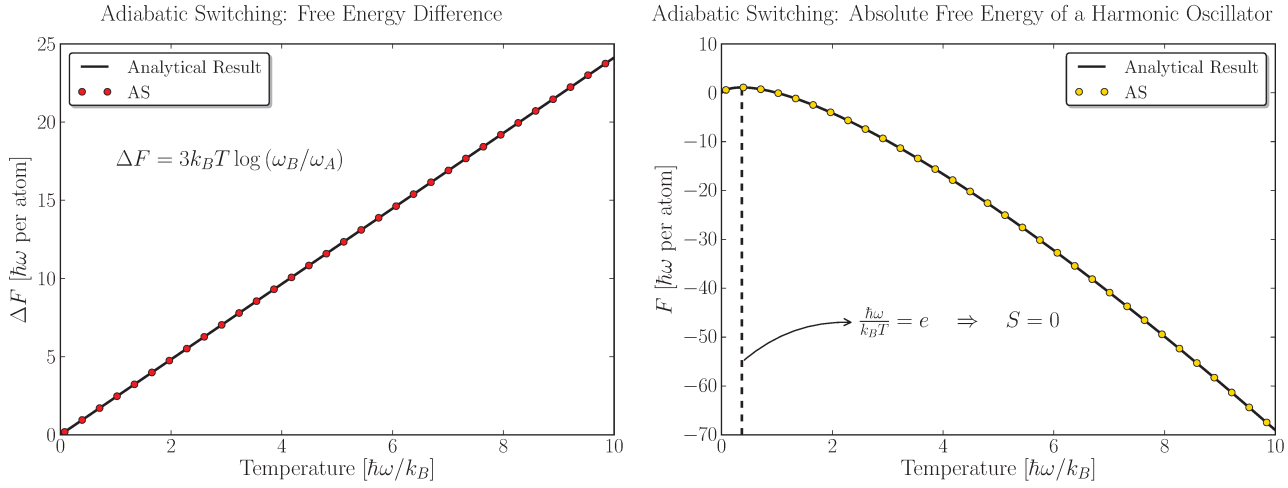

Figure 3.6: **Left**: Free energy difference (or quasi-static work) and **Right:** absolute free energy of the two set of harmonic oscillators. In both cases the error bars are too small to be visible in the graph.

3.6 Reversible-Scaling Method

In fig.3.6 (right) we have computed the temperature dependence of the free energy by running one simulation for each desired temperature. This can be a problem when, for example, we want to define the point where two free-energy curves cross to determine a phase transition temperature. In this section we describe a technique based on the AS method that allows us to compute the entire temperature dependence of the free energy in a certain temperature interval from a single MD simulation, improving the efficiency of the method enormously.

The Reversible-Scaling (RS) (de Koning et al., 1999b) is an intrinsically non-equilibrium method for efficient free-energy calculation. It makes use of the AS procedure to perform a specific quasi-static process where the potential energy of the system is scaled by the parameter λ. By using this procedure we are able to estimate the free energy of the system as a function of the temperature by performing only one constant temperature MD simulation. The significant efficiency improvement of this method when compared to the case where we compute only one free-energy value per MD simulation comes from the fact that in the RS all states along the process represent a physically significant state of the system (namely the system at a different temperature), while in the other cases only the initial and final states have a physical meaning. The intermediate states only have the purpose of linking these two states.

The derivation of the equations for the RS is done in many papers (de Koning et al., 1999b, 2000, 1999a) based only on the microscopic assumptions of statistical mechanics. We present here an alternative but completely analogous derivation of theses equations based partially on thermodynamical considerations.

We start by recalling that the Gibbs free energy is given by

$$G = E - TS + PV \qquad \Rightarrow \qquad dG = -SdT + VdP,$$

computing $d(G/T)$ we obtain

$$\begin{aligned} d\left(\frac{G}{T}\right) &= \frac{dG}{T} - \frac{G}{T^2}dT \\ &= \frac{-SdT + VdP}{T} - \frac{E - TS + PV}{T^2}dT \\ &= \frac{V}{T}dP - \frac{E + PV}{T^2}dT \\ &= \frac{V}{T}dP - \frac{H}{T^2}dT \qquad \Rightarrow \qquad \boxed{\left[\frac{\partial(G/T)}{\partial T}\right]_{N,P} = -\frac{H}{T^2}}, \end{aligned}$$

where we have used that $H = E + PV$ is the enthalpy. This final equation is known as the Gibbs-Helmholtz equation. Here we are going to derive the RS equation for zero pressure, the generalization for other pressures was made by de Koning et al. (2001). If $P = 0$ we have $H = E$ and then we integrate

Gibbs-Helmholtz equations in T to obtain

$$\frac{G(T,P=0,N)}{T} = \frac{G(T_0,P=0,N)}{T_0} - \int_{T_0}^{T} \frac{E(T',P=0,N)}{T'^2} dT'. \tag{3.18}$$

From now on we are going to omit the $P=0$ and N dependency on the notation of the Gibbs free energy and the internal energy. The thermodynamic internal energy E is the average of the total microscopic energy, that is, the sum of the kinetic and the potential energy:

$$E(T') = \left\langle \sum_{i=1}^{N} \frac{p_i^2}{2m} \right\rangle_{T'} + \left\langle U(\mathbf{r}^N) \right\rangle_{T'} = \frac{3}{2} N k_B T' + \left\langle U(\mathbf{r}^N) \right\rangle_{T'}$$

where we have used the equipartition theorem to compute the average value of the kinetic energy. The subscript $\langle \ldots \rangle_{T'}$ indicates that the average is to be taken in the ensemble with temperature T'. Using this equation in eq.(3.18) we have

$$G(T) = \left(\frac{T}{T_0}\right) G(T_0) + \frac{3}{2} N k_B T \ln\left(\frac{T}{T_0}\right) - T \int_{T_0}^{T} \frac{\left\langle U(\mathbf{r}^N) \right\rangle_{T'}}{T'^2} dT'. \tag{3.19}$$

Now to handle the integral in this relation we introduce the variable substitution characteristic of the RS method: $T' = T_0/\lambda'$ and we denote $T = T_0/\lambda$. Thus the integral becomes

$$\begin{aligned} -T \int_{T_0}^{T} \frac{\left\langle U(\mathbf{r}^N) \right\rangle_{T'}}{T'^2} dT' &= -\frac{T_0}{\lambda} \int_1^{\lambda} \frac{\lambda'^2}{T_0^2} \left\langle U(\mathbf{r}^N) \right\rangle_{T'} \left(\frac{T_0}{-\lambda'^2}\right) d\lambda' \\ &= \frac{1}{\lambda} \int_1^{\lambda} \left\langle U(\mathbf{r}^N) \right\rangle_{T'} d\lambda' \end{aligned}$$

and eq.(3.19) results in

$$G(T) = \frac{G(T_0)}{\lambda} + \frac{3}{2} N k_B T_0 \frac{\ln\lambda}{\lambda} + \frac{1}{\lambda} \int_1^{\lambda} \left\langle U(\mathbf{r}^N) \right\rangle_{T'} d\lambda'. \tag{3.20}$$

To obtain the ensemble average of the right-hand side of eq.(3.20) it is necessary to perform MD simulations at temperatures ranging from T_0 to $T = T_0/\lambda$. In order to eliminate this requirement we analyze this average and rewrite it as

$$\left\langle U(\mathbf{r}^N) \right\rangle_{T'} = \int d^{3N}r\, U(\mathbf{r}^N) \exp\left(-U(\mathbf{r}^N)/k_B T'\right) = \int d^{3N}r\, U(\mathbf{r}^N) \exp\left(-\lambda' U(\mathbf{r}^N)/k_B T_0\right) = \left\langle U(\mathbf{r}^N) \right\rangle_{T_0}^{\lambda'}$$

now the ensemble average is done at one constant temperature T_0 but using the scaled potential $\lambda' U(\mathbf{r}^N)$. Finally we obtain the equation characteristic of the RS method

$$G(T) = \frac{G(T_0)}{\lambda} + \frac{3}{2} N k_B T_0 \frac{\ln\lambda}{\lambda} + \frac{1}{\lambda} \int_1^{\lambda} \left\langle U(\mathbf{r}^N) \right\rangle_{T_0}^{\lambda'} d\lambda'. \tag{3.21}$$

Let us understand why it is important to rewrite the average as we have done by means of eq.(3.21). This equation gives us the free energy at any desired temperature T as a sum of three terms. The

first is the free energy at a reference temperature $G(T_0)$, which can be obtained using a single Frenkel-Ladd calculation. The second term is an exact formula and the third is the integral of an average value computed at a constant temperature T_0, exactly like the integrals that can be computed using the AS method, eq.(3.6), but with $H(\lambda) = K + \lambda U(\mathbf{r}^N)$ where K is the kinetic part of the Hamiltonian:

$$W^{qs}(\lambda) = \int_1^\lambda \left\langle U(\mathbf{r}^N)\right\rangle_{T_0}^{\lambda'} d\lambda'. \tag{3.22}$$

Thus we can write the final equation of the RS method using the work computed by the AS method:

$$\boxed{G(T) = \frac{G(T_0)}{\lambda} + \frac{3}{2}Nk_BT_0\frac{\ln\lambda}{\lambda} + \frac{W^{qs}(\lambda)}{\lambda}}. \tag{3.23}$$

We can apply the AS method, eq.(3.8), to compute this integral in one MD simulation and therefore obtain all values of $G(T)$ with the temperature within the range from T_0 (equivalent to $\lambda = 1$) to $T = T_0/\lambda$. The idea to obtain the intermediate values of $G(T)$ is that, once we have performed the MD simulation with λ changing from 1 to the final value λ, we can obtain a specific value of $T' = T_0/\lambda'$ by only recomputing the integral of eq.(3.23) with limits from 1 to λ'.

3.7 Reversible Scaling: Harmonic Oscillators

As a first application of the RS method we compute the free energy an Einstein crystal. Again we take advantage of the exact results available to illustrate how the method works. For the Einstein crystal we have the Hamiltonian of eq.(3.12) and we define the RS Hamiltonian to be the harmonic Hamiltonian of the Einstein crystal with a scaling parameter multiplying the potential energy,

$$H(\lambda) = \sum_{i=1}^N \frac{p_i^2}{2m} + \lambda\sum_{i=1}^N \frac{m\omega^2}{2}(\mathbf{r}_i - \mathbf{r}_i^0)^2.$$

For this choice of Hamiltonian we can compute the quasi-static work of eq.(3.22) exactly

$$\left\langle U(\mathbf{r}^N)\right\rangle_{T_0}^{\lambda'} = \left\langle U(\mathbf{r}^N)\right\rangle_{T'} = \left\langle \sum_{i=1}^N \frac{m\omega^2}{2}(\mathbf{r}_i - \mathbf{r}_i^0)^2 \right\rangle_{T'} = \frac{3}{2}k_BT' = \frac{3}{2}k_B\frac{T_0}{\lambda'},$$

giving

$$W^{qs}(\lambda) = \int_1^\lambda \left\langle U(\mathbf{r}^N)\right\rangle_{T_0}^{\lambda'} = \frac{3}{2}k_BT_0\ln\lambda.$$

To perform the MD simulations we use the same $12\times12\times12$ simple cubic lattice of 1728 tridimensional harmonic oscillators used in the AS method of mass $m = 55.847 g/mol$ and frequency $k = m\omega^2 = 10\, eV/\mathring{A}$. The reference temperature was chosen to be $T_0 = 32K$ and the final value of the parameter is $\lambda = 0.01$. This represents a range of temperatures from approximately 0.1 to 10.0, two order of magnitude of variation. Again the Langevin thermostat was used because of the ergodicity problem found with the Nosé-Hoover thermostat.

We start by checking the convergence of the method. First we compute the work done using AS in both directions, forward and backward. Fig.3.7 (left) shows the results, also illustrating how the hysteresis procedure works, eq.(3.11). By combining the results in both directions we obtain a better estimate for the quasi-static work. This figure also shows the convergence of the method towards the analytical result as we increase the switching time. This result is in agreement with fig.(3.7) (right) which shows that the dissipation of RS vanishes as we increase the switching time.

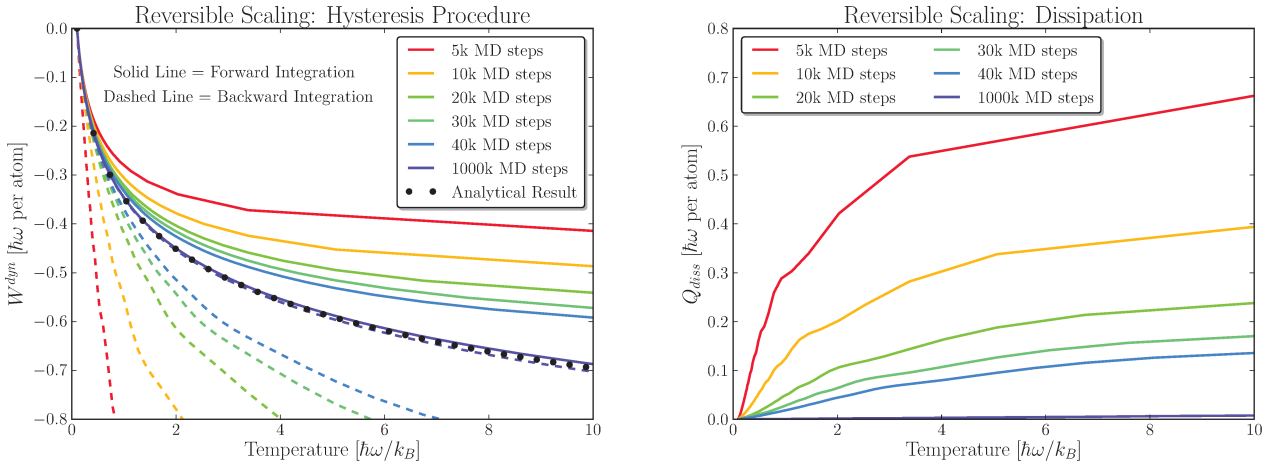

Figure 3.7: **Left**: convergence of the method when the switching time is increased. This graph also illustrates the hysteresis procedure: combining the result of the simulation in both directions results in a better agreement with the exact result. **Right:** dissipation of the RS method vanishes as we increase the switching time.

By combining both curves (forward and backward) of fig.3.7 (left) we build our estimate for the quasi-static work $W^{qs}(\lambda)$, as shown in fig.3.8 (left). This figure also shows the convergence of the method for longer switching times. For 10^6 steps $= 0.5ns$ we have an excellent agreement with the exact result. Notice that this figure includes only the numerical value computed by the simulation, therefore it is free from any functional dependence that could hide any imprecision of the result (as for example the second term of eq.(3.23)). Using eq.(3.23) we can construct the absolute free energy as function of temperature for the entire interval of temperatures of the simulation, fig.3.8 (right).

It is important to analyze the huge efficiency gain of the RS method over methods like the Frenkel-Ladd AS. Using the RS method one is able to compute the entire free-energy dependence on temperature for a certain interval by doing two MD simulations, one to compute the free energy at a reference temperature $G(T_0)$ (using methods like Frenkel-Ladd) and the other is to compute the $W^{qs}(\lambda)$ estimate and obtain the absolute free energy. Thus, with two AS simulations we are able to construct the free-energy curve as a function of the temperature. In the case of the other TI methods one needs to execute one AS simulation

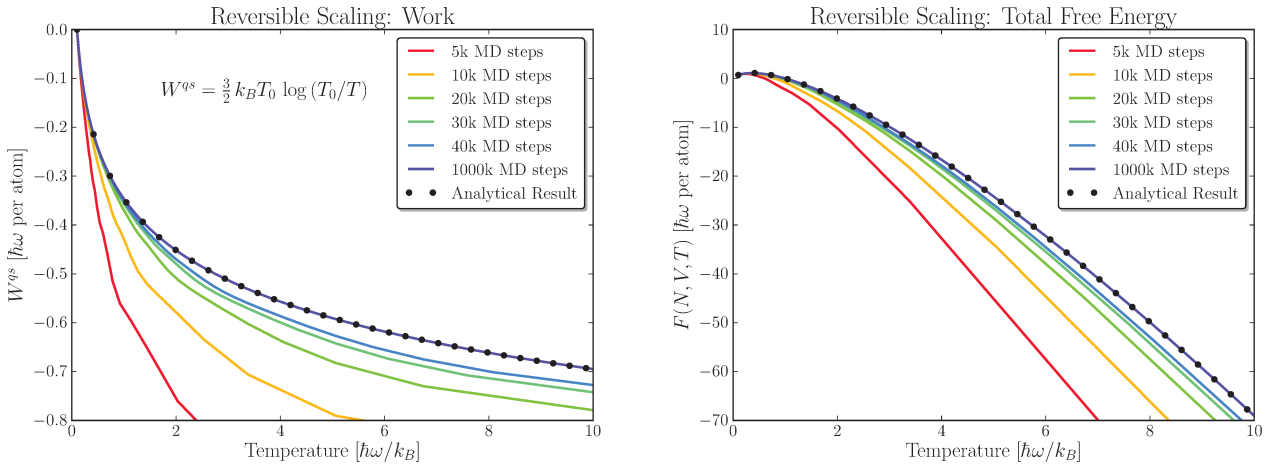

Figure 3.8: **Left**: estimative for the quasi-static work $W^{qs}(\lambda)$ compared to analytical result. **Right:** total free energy as function of the temperature computed using RS.

for each value of temperature, reducing drastically the efficiency. Even then it is not possible to compute the free-energy curve with the same precision as we do with RS. This imposes some limitations on the use of the other TI methods to, for example, study phase transitions as we will see in the next section.

Aside from the reduction in the required number of MD simulations there is also a computational performance gain because the RS method, unlike the other TI methods, does not require the simultaneous simulation of a reference system (*i.e.* harmonic oscillators in the Frenkel-Ladd method). This it also does not require the fine tuning between the system of reference and the system of interest (choosing the spring constant properly in the case of the Frenkel-Ladd method). In the RS method all that is required is a simulation of the system of interest with the scaled potential.

3.8 First Order Phase Transitions and Classical Nucleation Theory

In this section we are going to further develop the ideas about phase stability of section 3.1 to study the thermodynamics of first-order phase transitions. We present the role of the free energy in this type of phase transition and show a few of the characteristics specific to it. In addition, we present simplified model to describe the kinetics of first-order phase transitions, namely the classical nucleation theory. Our goal is to present the background necessary to study Martensitic phase transitions. In section 3.9 we analyze the thermodynamics of this phase transition using the RS method and in section 3.10 we study the kinetics of the phase transition using rare event methods.

In section 3.1 have seen that, given the thermodynamic conditions, we can measure the phase stability of a certain phase of a material by computing its free energy and comparing it with other possible phases.

By changing the thermodynamic conditions we also change the free energy. We have seen this in sections 3.5 and 3.7 where, by changing the temperature of the Einstein crystal, we change its free energy. Consider now a material that has two possible phases of free energy $F_l(T)$ and $F_g(T)$. For instance, it might be water in the liquid and gaseous phase, respectively. At a low temperature $T_- < T_t$ the most stable phase (the one with lowest free energy) is the liquid phase $F_l(T_-) < F_g(T_-)$, now if we start to increase the temperature, the free energy will start to change and it is possible that the rate of change is different for each phase in such a way that at a certain temperature T_t we have $F_l(T_t) = F_g(T_t)$ and both phases are equally stable at this point. This is the coexistence point. At even higher temperatures $T_+ > T_t$ the most stable phase will be the gaseous one $F_l(T_+) > F_g(T_+)$. This inversion of phase stability characterizes a phase transition and it is illustrated in fig.3.9. In this figure we can also see a behavior of the free-energy curve that is very specific to the first-order phase transition: the derivative of the free energy of this material has a discontinuity at the point of the phase transition. This is why we call this phase transition a first-order phase transition. Second-order (or continuous) phase transitions are phase transitions that present a discontinuity for the second derivative of the free energy. The consequences of this discontinuity will appear soon when we analyze the thermodynamical quantities that can be written as a first-order derivative of the free energy (*e.g.* the entropy).

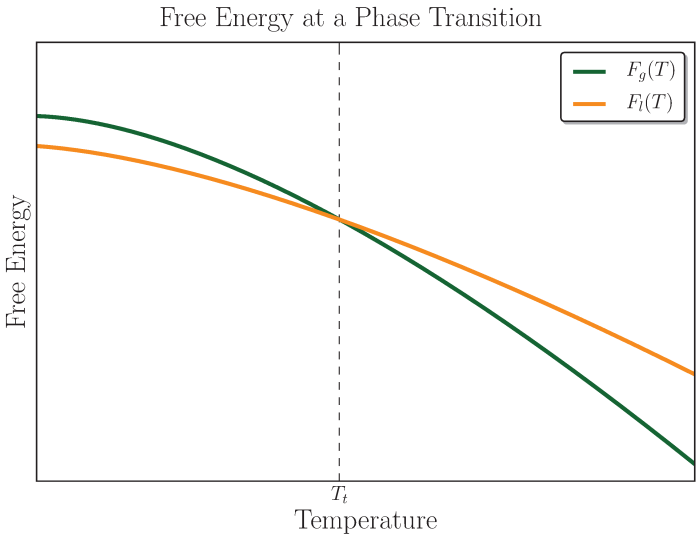

Figure 3.9: Free energy as function of temperature for two different phases of the same material (liquid and gaseous phases of water for example). The phase transition occurs when the two curves cross at the coexistence point.

We can better understand the origin of the behavior of the free energy by just analyzing its definition

$$F(N, V, T) = E - TS.$$

Each phase of the material has a specific function for internal energy and entropy, consider for example: S_{solid}, S_{liquid} and S_{gas}. At low temperatures the term $-TS$ is negligible compared to the internal energy due to the low value of T and therefore low temperatures favor phases of low internal energy E. This simple analysis shows us why at low temperatures the solid is almost always the most stable phase: in solids atoms and molecules are typically more strongly bound than in the liquid or gas phase and therefore have lower internal energy. Now, at sufficiently high temperatures the $-TS$ term becomes important and comparable to the internal energy E. Therefore, phases with higher entropy are more stable at high temperatures. This is why the gas and liquid phases are more stable than the solid phase at high temperatures. We can extend this argument to the Gibbs free energy

$$G = E - TS + PV \tag{3.24}$$

and show that phases with small volume (solid) are more stable at high pressures and phases with high volume (liquid and gas) are more stable at low pressures.

Aside from the temperature, other thermodynamic variables contribute to the phase transition. One variable whose influence is interesting to analyze is the pressure. Consider that we have found a point of coexistence of phases (like in fig.3.9) at a given temperature and pressure. Now we want to change the pressure by a small amount dP and determine how the temperature needs to be adjusted to keep both phases in coexistence. In order to do that we need to use Gibbs free energy because there is a change in pressure involved. From eq.(3.24) we know that

$$G = H - TS \qquad \Rightarrow \qquad dG = -SdT + VdP$$

therefore at the coexistence point if we change the pressure by dP and the temperature by dT the free energy of the liquid and gaseous phases change by

$$dG_l = -S_l dT + V_l dP$$
$$dG_g = -S_g dT + V_g dP.$$

But we want to impose the condition that after this change of pressure and temperature the free energy of both phases are still equal (condition for coexistence), thus

$$\Delta G = dG_l - dG_g = -\Delta S dT + \Delta V dP = 0 \qquad \Rightarrow \qquad \frac{dP}{dT} = \frac{\Delta S}{\Delta V}. \tag{3.25}$$

We can further simplify this equation by considering that under the same conditions

$$G = H - T_t S \qquad \Rightarrow \qquad \Delta G = \Delta H - T_t \Delta S = 0 \qquad \Rightarrow \qquad \Delta S = \frac{\Delta H}{T} = \frac{L}{T_t} \tag{3.26}$$

where we have recognized the latent heat of a phase transition as $\Delta H = L$. This shows us the origin of the latent heat: it is necessary to compensate the entropy difference between phases in a phase transition. Thus eq.(3.25) becomes

$$\frac{dP}{dT} = \frac{L}{T_t \Delta V}, \tag{3.27}$$

this is the so called Clausius-Clapeyron (Callen, 2006) equation. It gives the slope of the coexistence curve of a certain material in a P vs T phase diagram as a function of properties of the material: latent heat, transition temperature and specific volume. This equation is the relation that we were looking for: it gives us the connection between changes in pressure and temperature along the coexistence curve. Notice that this equation is only valid for first-order phase transitions. In its derivation we have assumed that the entropy of the phases are different and this is a direct consequence of the fact that the first order derivatives of the free energy present a discontinuities for first-order phase transitions. Note that the entropy is given by

$$S = -\left(\frac{\partial G}{\partial T}\right)_{P,N}.$$

Given a point of coexistence we can integrate the Clausius-Clapeyron equation, eq.(3.27) to reconstruct the entire coexistence curve of these phases of the material. This procedure can be done computationally using a generalization of the RS method for non-zero pressures (de Koning et al., 2001). What we obtain is the phase diagram of the material, such as shown in fig.3.10 (left) for a simple substance that presents three phases that can coexist at the triple point. In fig.3.10 (right) we have a realistic phase diagram of water that shows the existence of many solid phases. Phase diagrams of real substances can be quite complex, with each of the solid phases presenting different characteristics. For the case of water, for instance, a few of the crystalline phases present a ordered dipole structure (XI, XIII, XIV) while others do not.

Up to this point we have discussed thermodynamic features of a first-order phase transition. Next we analyze the kinetics of such a transition. Consider that the system is in the gaseous phase of fig.3.9 (temperature $T > T_f$). If we slowly decrease the temperature we will notice that the system does not change its phase when the temperature reaches $T = T_f$, it takes a further reduction of the temperature for the phase transition takes place. We can understand why this happens with a simple model known as *classical nucleation theory* (CNT). Although the liquid phase has a lower volumetric free energy $\Delta G = G_g(T) - G_l(T) < 0$ there is a energetic cost associated with the creation of the liquid phase inside the gaseous phase. More specifically, there is a surface tension γ between the interfaces of both phases. To create a nucleus of radius r of the liquid phase inside the gaseous phase there is an associated energetic cost of

$$\Delta G_\gamma = 4\pi r^2 \gamma \tag{3.28}$$

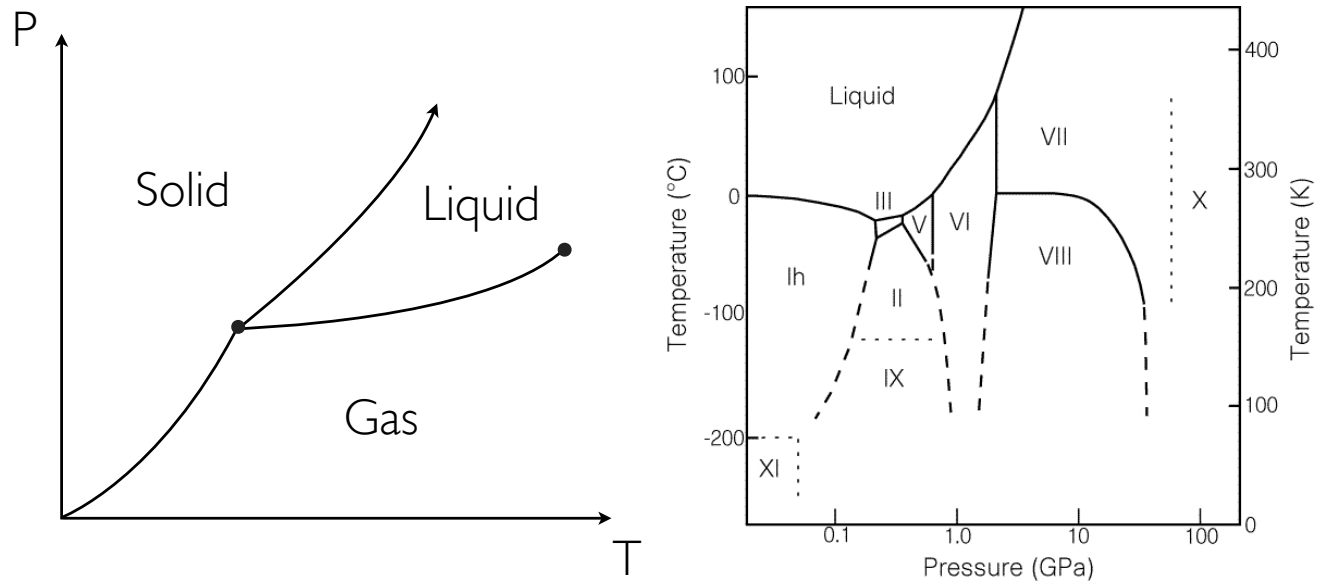

Figure 3.10: Illustration of phase diagrams. **Left:** phase diagram of a simple substance. **Right:** realistic phase diagram of water.

that the system needs to overcome by associated decrease of the bulk free energy

$$\Delta G_{bulk} = \frac{4\pi r^3}{3}\Delta G. \tag{3.29}$$

Considering a small degree of undercooling of the system ($T < T_f$), we have

$$\Delta G = \Delta H - T\Delta S = L - T\frac{L}{T_f} = -\frac{L\Delta T}{T_f}$$

where $\Delta T = T_f - T$ and we have used eq.(3.26). We also assume that the latent heat is independent of the temperature for small undercooling. This is the part of the free energy that contributes to the phase transition to happen and therefore is the *driving force* of the phase transition. Using the bulk free-energy difference, eq.(3.28), and the nucleation energetic cost, eq.(3.29), we can construct the total free energy of nucleation of a spherical nucleus of radius r

$$\Delta G_n(r) = \Delta G_\gamma + \Delta G_{bulk} = 4\pi r^2\gamma - \frac{4\pi r^3}{3}\left(\frac{L\Delta T}{T_f}\right). \tag{3.30}$$

In fig.3.11 we show the curve of $\Delta G_n(r)$ where we can see that there is a free-energy barrier to overcome if we want to grow a nucleus. The phase transition will only be complete when a nucleus of the liquid phase grows until the complete system has becomes liquid. We can compute the critical radius r^*, the maximum of $G_n(r)$, as

$$\frac{dG_n(r)}{dr} = 0 \qquad \Rightarrow \qquad r^* = \frac{2\gamma T_f}{L\Delta T}, \tag{3.31}$$

this is the point after which the nuclei will grow indefinitely and the phase transition will happen. The nucleation energy at this point is the height of the barrier that needs to be overcome

$$\Delta G_n(r^*) = \frac{16\pi}{3}\left(\frac{\gamma T_f}{L\Delta T}\right)^2. \tag{3.32}$$

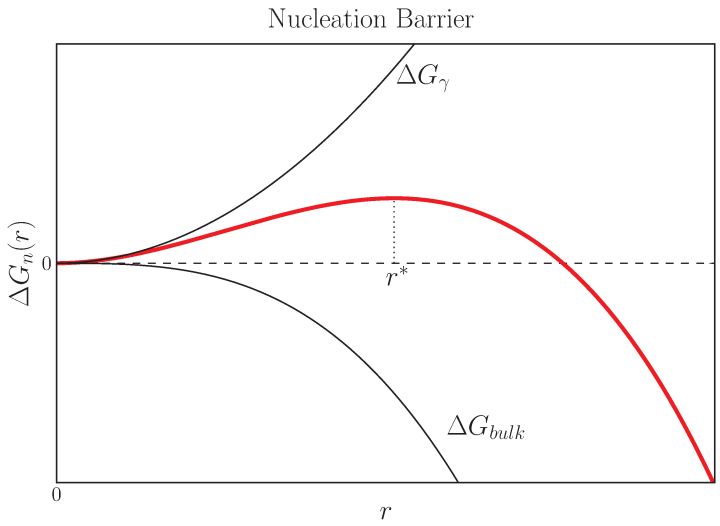

Figure 3.11: Free energy barrier associated with the nucleation phenomena.

By the CNT the kinetics of the transition happens as follows. When $T < T_f$ small droplets of liquid start to appear in the gaseous phase with probability $P(r) \propto \exp\left[-\Delta G_n(r)/k_B T\right]$. Most of them do not attain a radius equal or greater than the critical radius and shrink back until it vanishes. With a probability $P(r^*) \propto \exp\left[-\Delta G_n(r^*)/k_B T\right]$ one of these droplets will be created and reach the critical radius and the phase transition will start to occur. It is interesting to note that the critical radius, eq.(3.31), and the height of the barrier, eq.(3.32), become smaller as we increase the degree of undercooling ΔT , *i.e.* the transition will happen more easily as we undercool the system more and more.

The simple theory of the classical nucleation is capable of predicting many interesting characteristics of the kinetics of first-order phase transitions, in particular it presents the existence of the nucleation phenomena that are the hallmark of the first-order phase transitions. The existence of metastable states (*e.g.* undercooling or overheated states) hamper the determination of the transition temperature T_f because, as we have seen, the actual transition can happen at temperatures below T_f. It is at this point that the determination of the free energy using methods like TI is important because it provides us an accurate method to compute T_f that does not require the actual observation of the transition and therefore is not subject to such hysteresis effects.

Among the many characteristics that the CNT is not capable of predicting we can cite the presence

of magnetic domains in ferromagnetic materials. This is an effect that is intrinsically correlated to the minimization of the magnetic energy through the elimination of the external magnetic field of the magnet. In the case of solidification, there are effects due to the elasticity and tension present in crystals that do not appear in this theory. Furthermore, effects associated with anisotropy of the nuclei are also not taken into account in CNT.

3.9 Thermodynamics of Martensitic Phase Transitions using RS

Martensitic phase transformations belong to a class of first-order phase transitions in which the crystallographic structure of a solid changes. The fundamental characteristic of this phase transition is that it is diffusionless. The change in the crystallographic structure occurs due to small rearrangements of atoms, typically involving displacements smaller than the first-neighbor distance. These phase transitions take place in many economically significant material applications (Porter and Easterling, 1992) such as steel hardening and shape-memory alloys (a class of alloys that when deformed remembers its original shape and can return to it if heated).

Here we focus our attention on a specific Martensitic phase transition that occurs in pure iron. We present the behavior of iron at zero pressure in fig.3.12. At temperatures below 1184K (Bendick and Pepperhoff, 1982) the stable phase of a system of pure iron is the α (BCC) phase. At temperatures above 1184K but below 1665K the most stable phase is γ (FCC) and above 1665K iron is stable in the δ (BCC again) phase until it melts at 1809K (Brook and Brandes, 1983). In this figure we also present an idealized mechanism for this phase transition known as Bain's Path in which the transition happens without any shear.

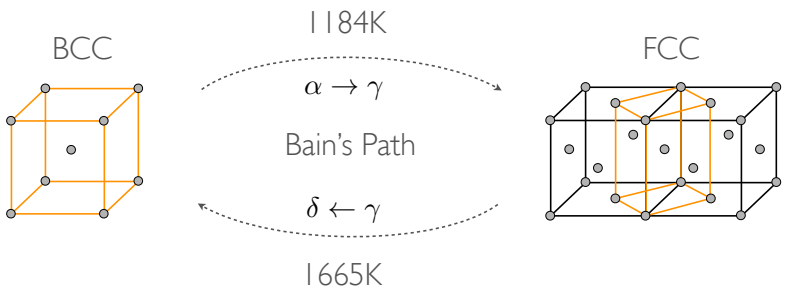

Figure 3.12: Martensitic phase transition in iron.

This phase transition is very important in the process of steel hardening. Steel is an alloy of iron and carbon (but other elements can also be used). A small weight percentage ($\leq 2\%$) of carbon is added to modify the hardness of the material by preventing linear defects known as dislocations to slide

past one another. The process of steel hardening has been known for thousand years. At the α phase for temperatures below 1184K iron presents low solubility of carbon. When heated to the γ phase its solubility increases significantly and carbon can be added to this phase. Then, if the temperature of the material decreases rapidly (a process known as quenching) so that the carbon does not have enough time to diffuse out of the iron, the iron goes back to the low temperature α phase but turning into a supersaturated solution with carbon that presents higher hardness than pure iron.

Aside from its importance in materials science and in industry, this is a very interesting phase transition from the physical point of view. Typically metals have closed-packed structures (FCC or HCP) as the most stable forms. In iron it is the ferromagnetic energy contribution of α phase that stabilize the BCC structure at low temperatures (Hasegawa and Pettifor, 1983) (the magnetism also has a crucial role in many other characteristics of iron, including other phases that not BCC). The spin degrees of freedom have an important contribution to the entropies of both α and γ phases. The Curie temperature of Fe is 1043K and above this temperature the α phase loses its ferromagnetic properties and the excess of magnetic entropy of the γ phase drives the $\alpha \rightarrow \gamma$ phase transition. The transition back to the BCC structure (δ phase) at higher temperatures ($\gamma \rightarrow \delta$) is common to many materials. Often the low temperature FCC structure transforms to the high temperature BCC phase (Lee et al., 2012). In this $\gamma \rightarrow \delta$ phase transition the contribution of the magnetic spins is still important Hasegawa and Pettifor (1983)

We are going to apply the RS method to study the thermodynamic equilibrium and polymorphism of pure iron. We intend to reproduce the experimental phase stability with respect to the temperature at zero pressure. Thus we need to obtain the Gibbs free energy curve as a function of the temperature for the range of temperatures across which the phase transition happens. We are interested in the relative stability of BCC and FCC structures because these are the structures that appear in the phase diagram at zero pressure. In addition, we perform the same calculations for the HCP structure because of the many similarities between this structure and FCC.

The first issue address is the reproducibility of the experimental behavior of iron using classical empirical interatomic potentials. Lee et al. (2012) developed two different MEAM (Baskes, 1992) potentials including the second nearest-neighbor formalism (Lee and Baskes, 2000) to reproduce the behavior of pure iron, one of the conclusions relates to this problem of reproducibility: *"(...) the correct reproductions of the phase stability among three crystal structures of iron with respect to both temperature and pressure are incompatible with each other due to the lack of magnetic effects in this class of empirical interatomic potential models (...)"*. This kind of incompatibility between two desired properties where improving the description of one property results in a deterioration for another appears frequently when one is fitting interatomic potentials. In many cases these difficulties are related to the electronic degrees of freedom

and quantum mechanical effects not present in this type of simulation.

In general, the modeling of magnetic materials remains a true challenge and the highly non-trivial task of including the subtle effects of magnetism in force field simulations has not been solved. The best attempts to reproduce the experimental behavior of iron using empirical potentials is therefore left to complex fitting schemes where the magnetic effects in the stability of phases is mimicked using the lattice energy and the phonon contributions to the free energy. Despite these issues with the experimental reproducibility of the thermodynamic equilibrium a few interatomic potentials have obtained some success in reproducing these phase transitions.

The application of RS in this phase transition is a good example of how free-energy calculation methods can be successfully applied to the realistic case of an interatomic potential. The efficiency of classical simulations like MD and Monte Carlo are an advantage over first-principle simulations that allow us to simulate systems of sizes interesting for materials science applications. We describe now the general algorithm used to compute the free energy of the different phases of iron, making use of the Frenkel-Ladd TI, RS and other general numerical techniques.

We are going to present results for three different potentials that present the $\alpha \rightarrow \gamma$ phase transition, namely the Embedded-Atom Model (EAM) potential of Meyer and Entel (1998), the Analytical Bond Order (ABOP) potential of Müller et al. (2007) and the Modified Embedded-Atom Model (MEAM) for temperature dependence of Lee et al. (2012). From now on we refer to these iron potentials by the name of the class of potentials (EAM, ABOP and MEAM). A few other potentials have also been tested but they do not present this phase transition. For all three potentials we have computed the timestep size by direct verification of the conservation of energy for an isolated system. Fig.3.13 (left) illustrates the result of energy conservation for the MEAM potential. We have then chosen 3fs for MEAM and 1fs for the EAM and the ABOP potentials.

Once again the Nosé-Hoover thermostat has shown problems with the canonical sampling at low temperatures. Notice that this time we are applying the thermostat to a full interatomic potential, with no harmonic approximations. In fig.3.14 we show the result of the canonical sampling for the MEAM crystal at temperature of $1K$. The two graphs on the top show the kinetic and potential energy distribution respectively. Although the distributions have a Gaussian shape they are not the same for different chain lengths and do not agree with the equipartition theorem for the kinetic energy. In the two graphs on the bottom we have shown the density distribution for the velocity and position, comparing the result for the velocity with the exact solution. In all cases we found a behavior that depends on the chain length. For the velocity we can see that none of the results agree with the exact solution. Although the results show that the Nosé-Hoover thermostat does not correctly sample the canonical ensemble for crystal at

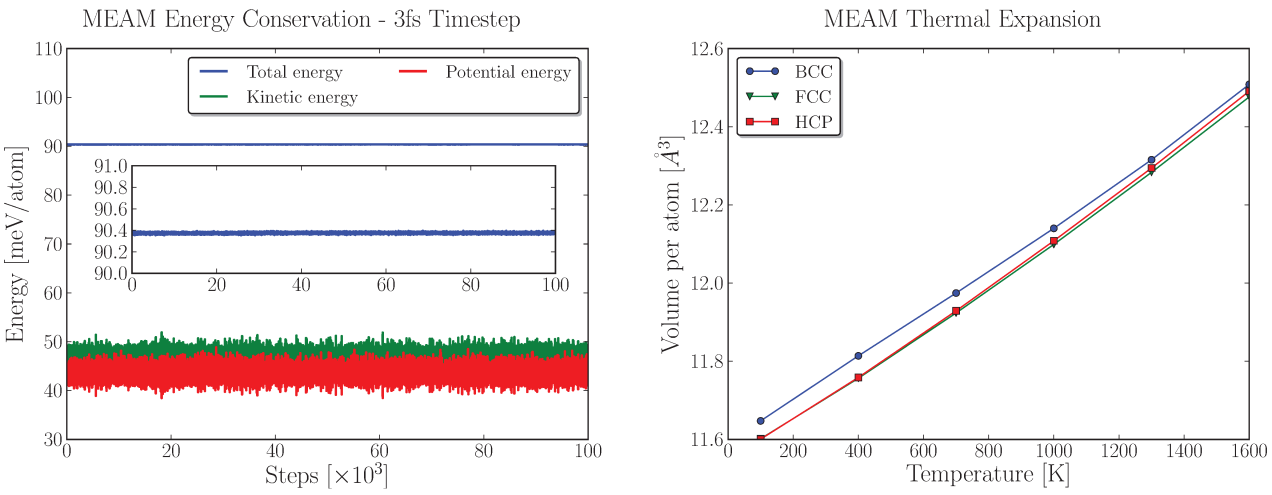

Figure 3.13: Illustration of **Left:** energy conservation and **Right:** thermal expansion for the MEAM potential, a similar approach was taken for all used potentials.

low temperatures it is clear that these results are better than the ones for the harmonic oscillators, figs.2.4 and 2.5. We relate this improvement with the anharmonicity present in the full interatomic potential. It is known (Ashcroft and Mermin, 1976) that the anharmonicity is responsible for the energy exchange between the normal modes of a crystal and therefore leading to a better sampling for the Nosé-Hoover thermostat.

Fig.3.15 shows the results for the canonical sampling of the MEAM potential using the Langevin thermostat at the same 1K temperature. On the top we show the result for the average kinetic and potential energy respectively. The kinetic energy agrees with the equipartition theorem and, as expected, the potential energy does not agree due to the anharmonicity of the potential. We can see that even at low temperatures there is a divergence of the harmonic behavior for the potential energy (recall that the kinetic energy always respects the equipartition theorem). At the bottom we have the density distribution of the velocity and position, the velocity distribution agrees with the exact result.

We now want to compute the free-energy temperature dependence using RS but in order to do so we need to compute the absolute free energy at a reference temperature $G(T_0)$ using the Frenkel-Ladd method. In what follows we explain the procedures to obtain the complete temperature dependence of $G(T)$ using the methods presented earlier in this chapter.

Initially we select the reference temperature T_0 and compute the equilibrium lattice constant of the iron crystal potential at this temperature, $a(T_0)$. In fig.3.13 (right) we show the thermal expansion of the MEAM potential at zero pressure. With this curve we can obtain the equilibrium lattice constant at zero pressure for different temperatures. Using the reference temperature we compute the mean-square displacement of the atoms of the iron crystal at zero pressure and with eq.(3.16) we obtain the frequency

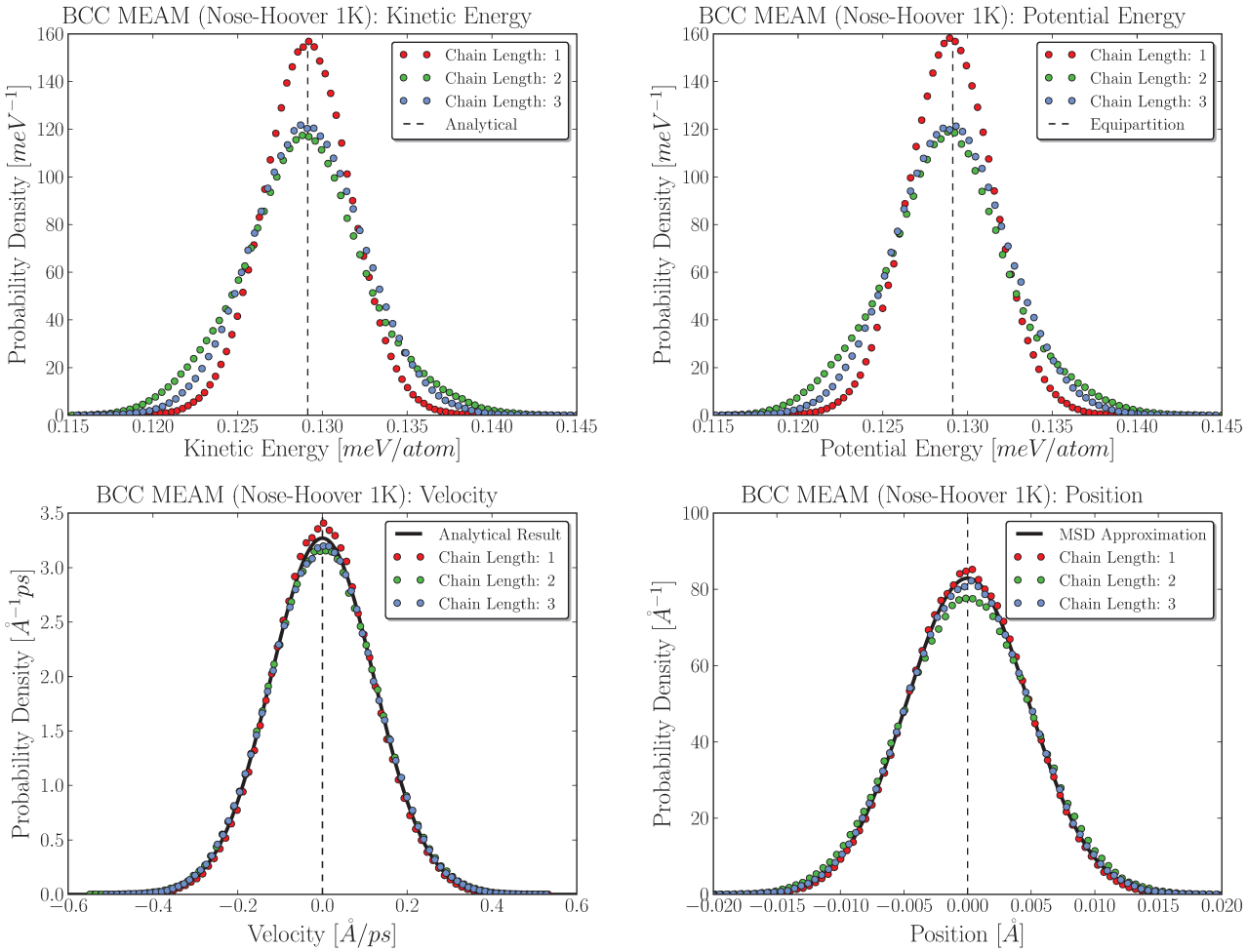

Figure 3.14: Verification of the canonical sampling for the Nosé-Hoover thermostat, **Top:** the kinetic and potential energy have a Gaussian shape that depends on the thermostat length and does not agree with the equipartition theorem. **Bottom:** distribution of velocity and position for one atom of the crystal, the velocity distribution does not agree with the exact solution, the position distribution is compared with the distribution of the harmonic approximation of the crystal.

of the harmonic oscillators to be used in the Einstein crystal of the Frenkel-Ladd method. In figs.3.15 (bottom right) we compare the position distribution of one atom compared with the distribution of a harmonic oscillator with frequency given by eq.(3.16), as we can see this approximation performance is very good at low temperatures (where usually the reference temperature is chose). On the other hand, it is expected that this approximation performs poorly as the temperature approaches to the phase-transition temperature.

At this point we have the equilibrium lattice constant $a(T_0)$ and the frequency of the harmonic approximation of the crystal. We now can use the Frenkel-Ladd method with this lattice constant (compatible with the zero pressure requirement) to obtain $G(T_0)$. We have repeated this procedure for the BCC,

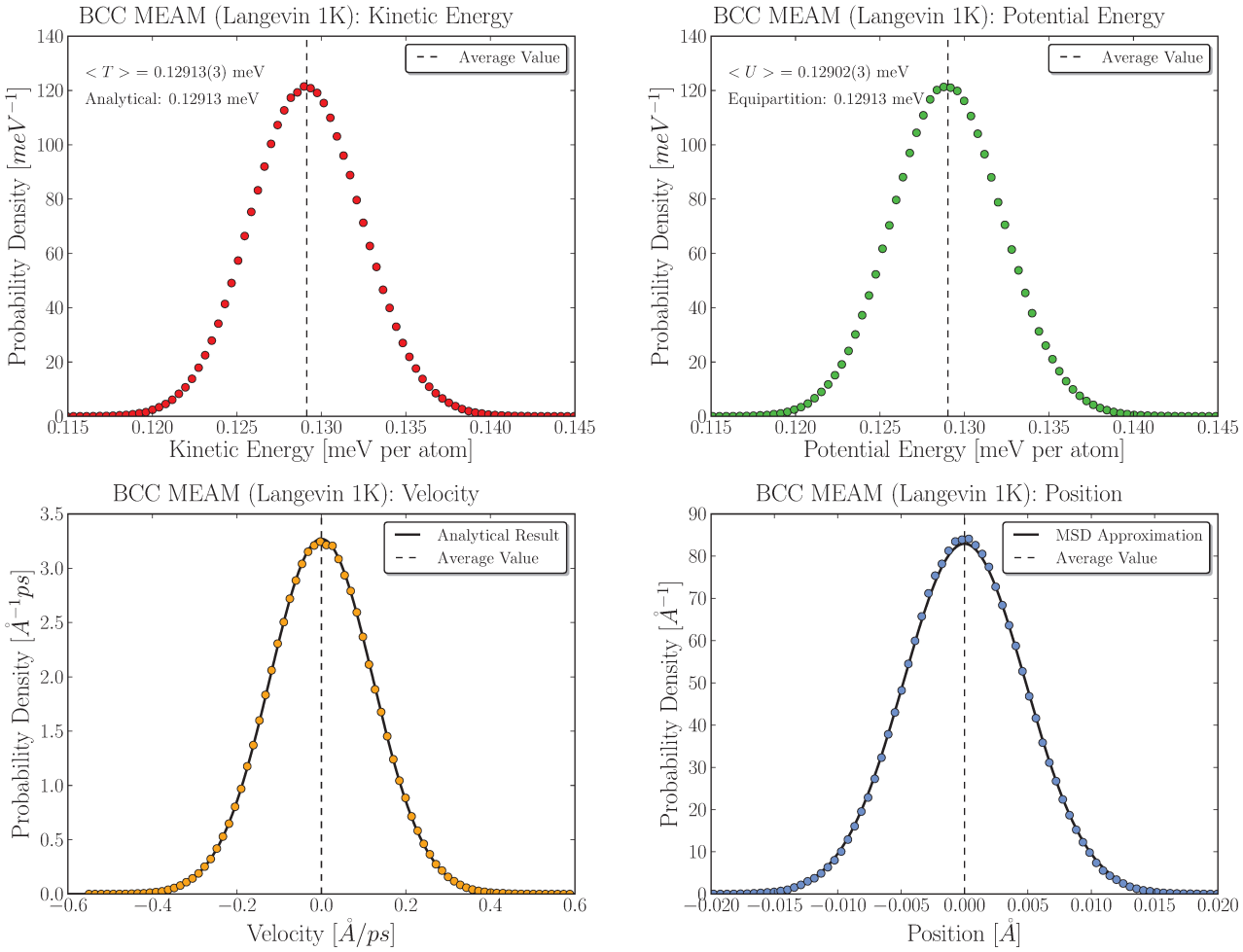

Figure 3.15: Verification of the canonical sampling for the Langevin thermostat, **Top:** the kinetic and potential energy distributions are Gaussian and the kinetic distribution agrees with the equipartition theorem. **Bottom:** distribution of velocity and position for one atom of the crystal. The velocity distribution agrees with the exact solution, the position distribution is compared with the distribution of the harmonic approximation of the crystal.

FCC and HCP structures of all three potentials. The switching time was 1ns and the system size was $18 \times 18 \times 18$ (11,664 atoms) for the BCC structure and $14 \times 14 \times 14$ (10,976 atoms) for FCC and HCP structures respectively. We performed the simulations a number of times to reduce the statistical error. We found that 3 uncorrelated simulations were sufficient due to the reasonably large size of the system (errors decrease approximately as $N^{-1/2}$). All numerical integrations were performed using the Trapezoidal Rule (Press et al., 2007) and all derivatives were computed by first fitting a simple spline to the data and then deriving the resultant curve.

With the obtained values of $G(T_0)$ we performed the RS simulations using the same system size. Once again 3 simulations of 1ns were performed to assure that the statistical errors were sufficiently small. In

order to keep the pressure equal to zero during the simulation we used the Nosé-Hoover barostat (Martyna et al., 1994) with a chain of size 3.

To check the result of the RS simulation we have performed the Frenkel-Ladd method at a certain number of different temperatures and compared the values to the RS results. In addition, we also used three different reference temperatures, 100K, 400K and 700K to verify whether the results depend on the reference temperature. The results for the EAM, ABOP and MEAM potentials are shown, respectively, in figs.3.16, 3.17 and 3.18.

Fig.3.16 shows the results for the EAM potential. From these graphs we see that this potential predicts that the HCP structure is always more stable than the FCC, for the entire temperature range analyzed. The $\alpha \rightarrow \gamma$ transition occurs at a temperature of (480 ± 1)K, almost 2.5 times smaller than the experimental result of 1184K.

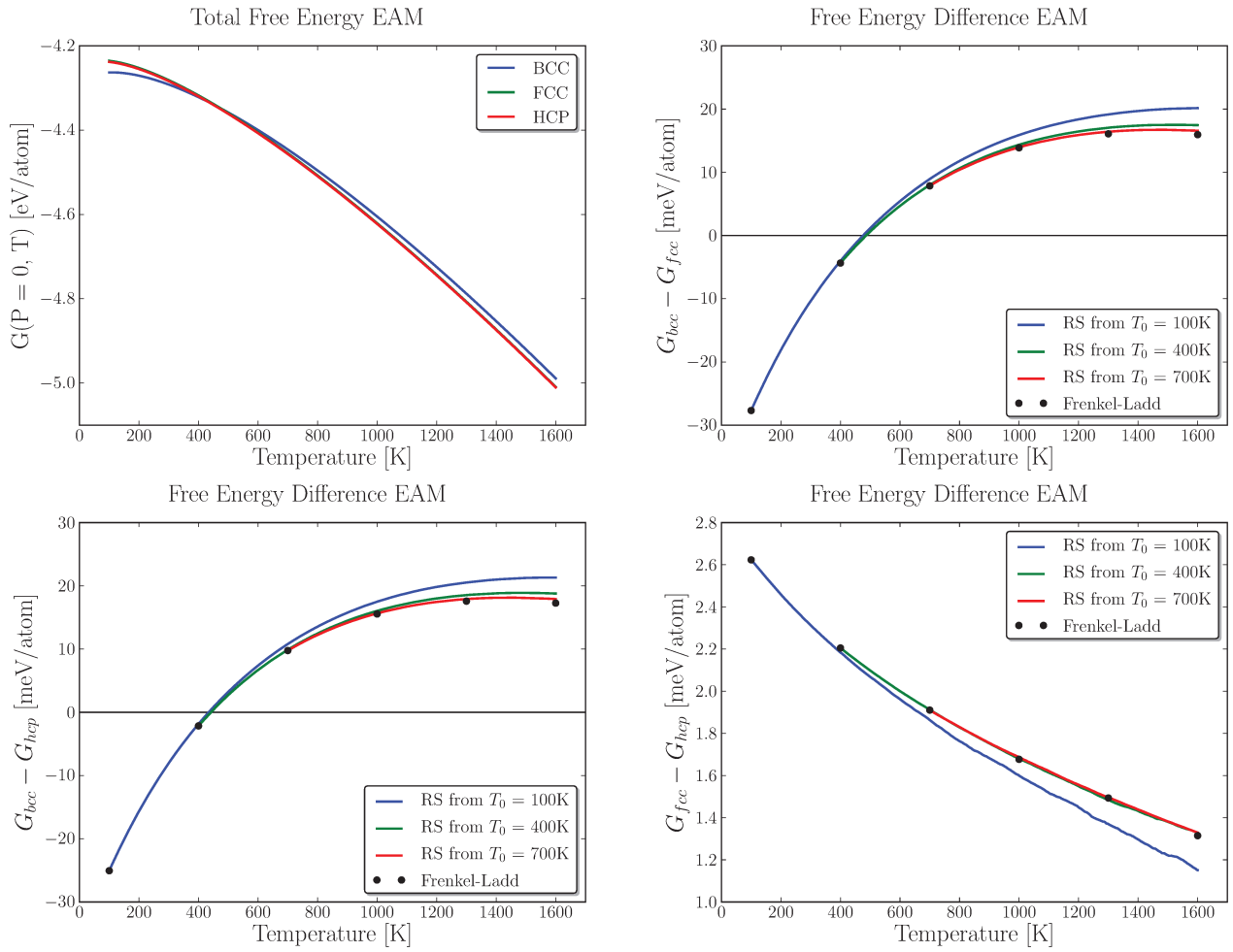

Figure 3.16: Gibbs free energy at zero pressure for different crystallographic structures using the EAM potential.

In fig.3.17 we display the results for the ABOP potential. This potential also predicts the HCP

structure to be more stable than the FCC for the considered range of temperatures. On the other hand, the transition temperature of the $\alpha \rightarrow \gamma$ transformation is (1025±1)K, the best of the three potentials. We have extended the range of temperatures for the BCC-FCC free-energy difference to show an interesting feature of this potential. After approximately 1500K this potential shows a decrease (negative slope) in the free-energy difference, indicating a tendency to stabilize the BCC phase again before melting ($\gamma \rightarrow \delta$ transition). Although we have seen this tendency, the crystal melts at approximately 2400K, before the BCC becomes the more stable phase again. In the FCC-HCP free-energy difference curve we see that the free-energy difference between these phases is very small and, as can be seen by the fluctuations in the graph, difficult to measure. This was a feature included by Müller et al. (2007) to obtain a good phase transition temperature for the $\alpha \rightarrow \gamma$ transformation.

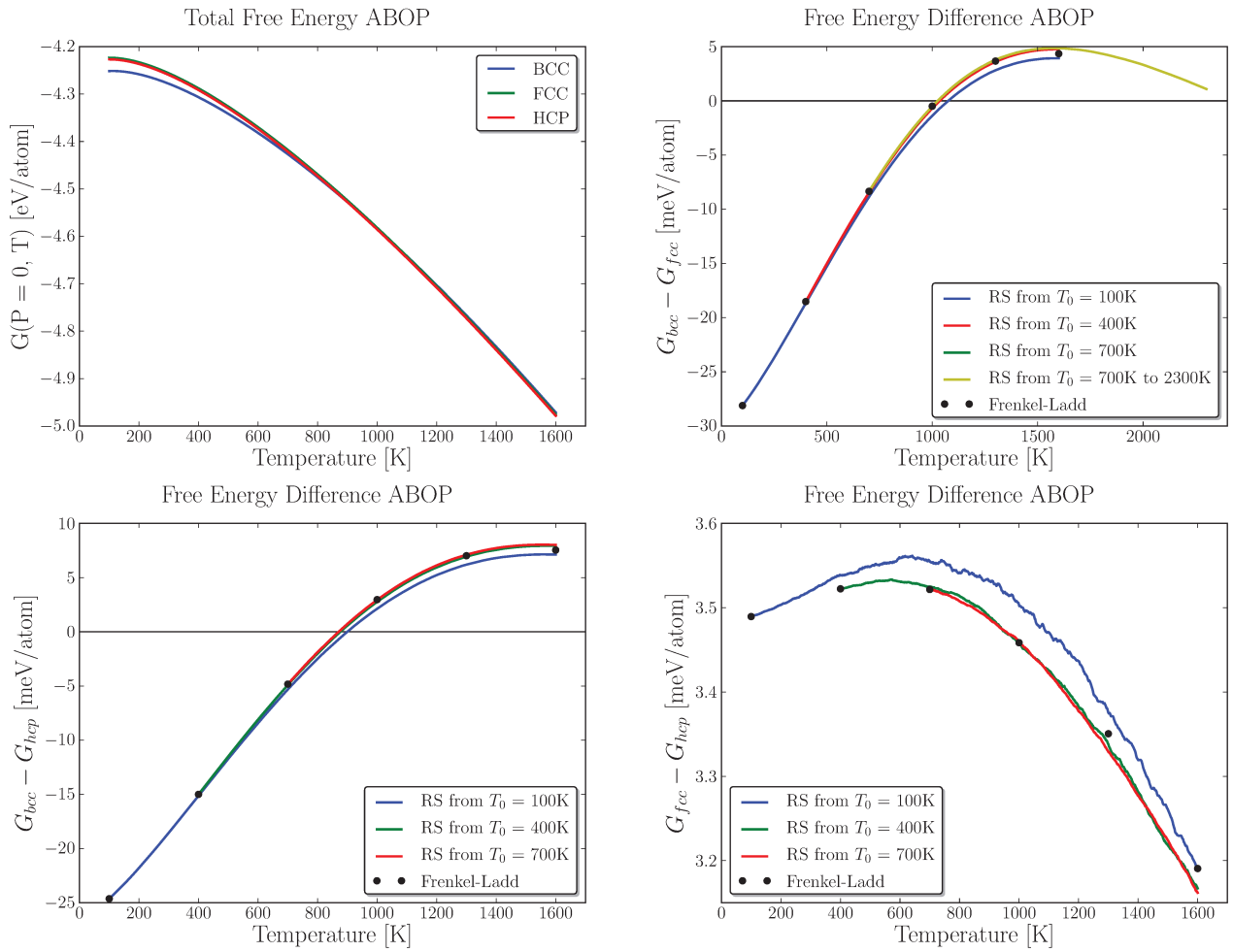

Figure 3.17: Gibbs free energy at zero pressure for different crystallographic structures using the ABOP potential.

The last analyzed potential is the MEAM shown in fig.3.18. This potential correctly predicts the phase stability: the FCC phase is always more stable than the HCP for zero pressure and the computed

temperature range. Another good feature is that in this temperature range the BCC phase is always more stable than the HCP. This is important when we study the kinetics of the phase transition since it avoids the nucleation of the HCP during the transition. The phase transition temperature of the $\alpha \rightarrow \gamma$ transformation is (950 ± 1)K, better than the EAM potential but it is still almost 20% smaller than the experimental value. Because of the correct phase stability order and the reasonably good transition temperature we believe that this is the best potential of all three to study the Martensitic phase transition in pure iron. In terms of efficiency, this potential performs better than the ABOP but is worse than the EAM potential. This is not a real issue however, due to the powerful parallelization of both, the LAMMPS MD code and the free-energy calculation methods.

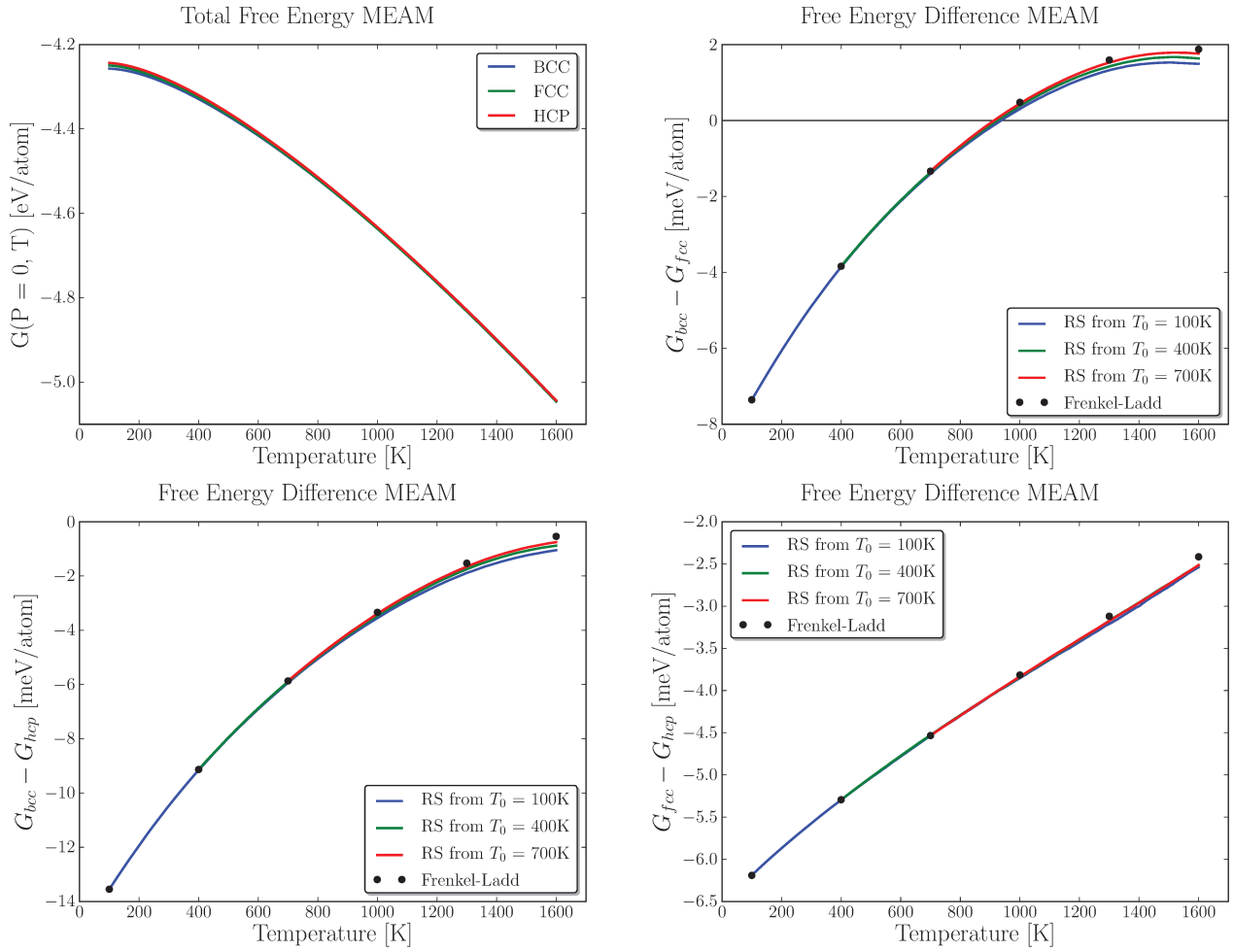

Figure 3.18: Gibbs free energy at zero pressure for different crystallographic structures using the MEAM potential.

For the MEAM potential we show in fig.3.19 the enthalpy $\Delta H = \Delta E + P\Delta V$ and the entropy $-T\Delta S$ contribution for the free-energy difference $\Delta G = \Delta H - T\Delta S$ between the BCC and FCC structures. In this graph we can see how these two terms compete to make this phase transition happens.

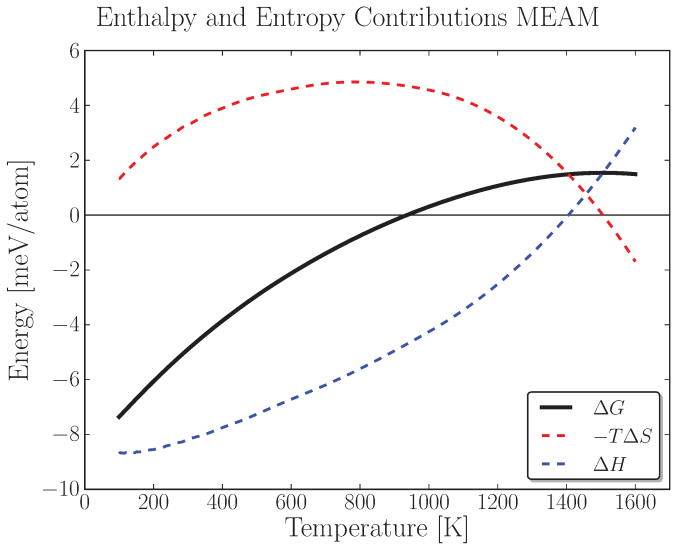

Figure 3.19: Enthalpy and entropy contributions to the Gibbs free energy of MEAM potential.

We now turn to analyze the agreement between the Frenkel-Ladd method and the RS. From figs.3.16, 3.17, 3.18 we notice that at high temperatures (at the end of the temperature range actually) the RS result starts to diverge from the result of the Frenkel-Ladd method. We attribute this behavior to the type of scaling of temperature that is made in the RS $T = T_0/\lambda$ where the $\lambda(t)$ parameter has a linear variation in time. As we have seen, in the RS method each state of the switching has the physical meaning of representing the system of interest at a temperature T. Because of the $1/\lambda$ dependence, the rate of temperature variation is faster at the end of the switching interval and therefore we have less states per temperatures at the end of the temperature range (high temperatures). A possible correction for this problem is to implement the $\lambda(t)$ parameter variation in such a way that the temperature variation is constant during the entire switching process. Another result that agrees with this interpretation is that the divergence between the methods becomes smaller if we choose higher reference temperatures while keeping the final temperature the same. This reduces the temperature interval and therefore includes more states for high temperatures at the end of the switching.

Here we have chosen to compute the entire free-energy curve to illustrate how the method works. Technically this is not necessary. The most efficient way to use RS to compute a transition temperature is described by Ryu and Cai (2008) where the melting temperature for many different metals and semiconductors is computed, the free-energy curves are calculated only close to the transition temperature, reducing the temperature range of the simulation and therefore increasing the precision of the final result. It is interesting to notice in this paper that, due to the reduced size of the system used by Ryu and Cai (2008) they do not obtain a better precision in the transition temperature than we do. Because all the λ-integration methods only depend on averages over all the system, the size of the system can significantly

influence the error due to its $N^{-1/2}$ dependence.

3.10 Kinetics of Martensitic Phase Transitions

We present now our attempt to study the kinetics of the Martensitic phase transition in pure iron using MD. From an experimental point of view the kinetics of this transformation is difficult to analyze due to the fast growth of the new crystal structure inside the system. For this reason not much is known about the mechanisms of this phase transition. In fig.3.12 we show an idealized mechanism known as Bain's Path (Porter and Easterling, 1992) by which one can change from the BCC structure to FCC by expanding the cubic unit cell in the $\hat{\mathbf{z}}$ direction by a factor of $\sqrt{2}$. Notice that there is no shear involved in this mechanism. There are many challenging questions related to the kinetics of this phase transition regarding the role of defects in the transition, the importance of specific crystallographic orientations in the growth of the new phase inside the crystal and many others. From a computational point of view there are even more aspects of the phase transition to be tackled. Here we present our attempt to implement a rare event method using MD to study the kinetics of transformation. The *Forward Flux Sampling* method (FFS) (Allen et al., 2005) is a technique variant of a broad class of rare event simulation methods know as *Transition Path Sampling* (TPS) (Dellago et al., 1998). Typically when studying rare event processes one wishes to know two things: how often the event (the phase transition in our case) happens or the rate constant k_{AB} of the process from a state A to a state B and the free-energy barrier associated with the process. Rare event method like FFS and TPS allow us to compute these quantities from atomistic simulations. We introduce now the rare event problem where the need for FFS-like methods appears.

MD simulations have two severe limitations in its applicability: spatial and temporal constraints due to limited computing power. The origin of the spatial limitation is the natural microscopic nature of matter. The typical atomic distance between two atoms is $\approx \mathcal{O}(1\mathring{A}) = \mathcal{O}(10^{-10}m)$. Thus if we want to simulate a system at a scale of μm we need approximately 10^{12} atoms (a trillion atoms). This limitation has been reasonably overcome over the years due to the rapid development and expansion of high-performance parallel computing clusters. Using the availability of many processors and techniques like spatial decomposition (Plimpton et al., 1995) we have been able to perform MD simulations with trillion atoms (Timothy and Kadau, 2008).

The temporal limitation of MD simulations is more subtle. It arises from the necessity of correctly integrating the vibrational motion of atoms. Typically the frequency of oscillation of atoms in solids is $\mathcal{O}(10^{13}Hz)$, which imposes a limitation on the timestep of approximately $\Delta t \approx 1$fs. Therefore, for a simulation of 1ns of real time, we need to compute 10^6 steps and this is currently the approximate limit of the time length of a simulation. Due to the causality of classical mechanics we cannot use an approach

like the one used in the spatial limitation, something like "time decomposition" will not work.

It is the severe temporal limitation of MD simulations that creates the need for rare-event methods. For example, in a first order phase transition the metastable states can exist for a long period of time compared to the nanoseconds of duration of an MD simulation. The event of a phase transition is driven by fluctuations inside the system and if the undercooling of a phase is small, the necessary fluctuation to make the transition happen can be quite rare. One example already cited here where this happens is diamond. Rare-event methods serve to try to remedy this situation and facilitate the observation of these rare fluctuations.

In FFS the definition of an order parameter α capable of differentiating between two states A and B is of fundamental importance, where A and B are stable states. Each of these states is associated with a typical value of the order parameter, α_A and α_B. Between these values we define a series of $n+1$ intermediate interfaces with order parameter $\alpha_0 = \alpha_A, \alpha_1, \alpha_2, \ldots, \alpha_{n-1}, \alpha_n = \alpha_B$. This order parameter is going to be monitored during a simulation. Fig.3.20 shows a scheme of the algorithm of this method. We start the simulation in state A defined as $\alpha < \alpha_A$ and monitor α during a certain period of time. During this time we store M configurations of the system in which $\alpha = \alpha_A$. After that, we randomly select one of them and continue the simulation until the system reaches α_1 or returns to $\alpha < \alpha_A$. If the system reaches α_1 we store that configuration, if it went back to $\alpha < \alpha_A$ we discard the final configuration. Then we start again from the previous α_A configuration and repeat the process, until we store M configurations. After this we randomly select one of the configurations with $\alpha = \alpha_1$ and start the process again, until we obtain M configurations for each interface and reach $\alpha = \alpha_B$. The final result is that the system is driven in a ratchet-like manner from state A to the final state B without any imposition on the microscopic dynamics.

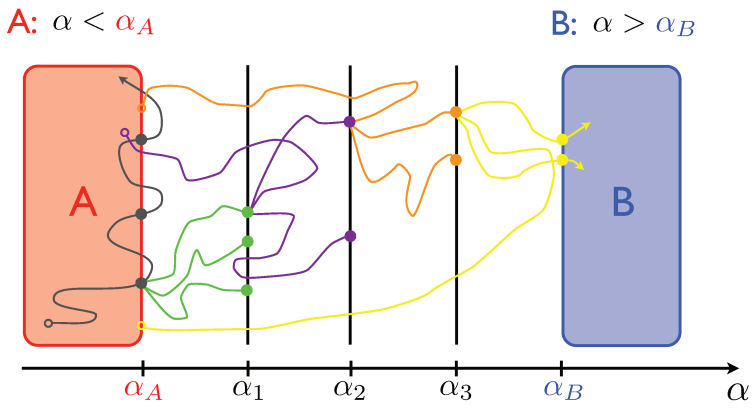

Figure 3.20: Scheme of the FFS method algorithm. The trajectories with same color have the same initial state, different colors represent trajectories of different interfaces.

Now, we have outlined the general features of the FFS method, there are many points that need to be clarified. The first is that the dynamics between each interface has to contain an element of stochasticity. Otherwise the evolution of the system is deterministic and we will always obtain the same trajectory (for example, the NVE ensemble or the Nosé-Hoover chain thermostat are deterministic dynamics). Frequently, the FFS method is implemented using Monte Carlo due to its stochastic nature. The first implementation of FFS using MD was in the study of bubble nucleation in a Lennard-Jones fluid by Wang et al. (2008). One of the possible approaches to this problem of stochasticity in MD simulations is to use the Langevin thermostat or to introduce random small perturbations (*e.g.* modification of the velocity of one particle) in the system. Another interesting point about FFS is its flexibility in terms of the choice of the random configurations, the quantity of configurations and how to evolve the system from a specific interface to another. Allen et al. (2009) present three possible variants: Direct FFS, Branched growth and Rosenbluth-like FFS. These variants allow us to adjust the method to the system to be simulated so as to and improve its efficiency (Allen et al., 2006).

To compute the rate constant k_{AB} we first define it in terms of FFS variables according to

$$k_{AB} \equiv \phi_{A,B}.$$

Here $\phi_{A,B}$ is the steady-state flux of trajectories leaving state A and reaching state B. We can write it as

$$\phi_{A,B} = \phi_{A,0}\, P(\alpha_B|\alpha_0)$$

where $\phi_{A,0}$ is the steady-state flux of trajectories leaving A and crossing α_0 interface multiplied by the conditional probability that a trajectory that crosses α_0 coming from A will reach B before going back to A. We can easily compute the flux $\phi_{A,0}$ since the crossing of α_0 from a trajectory initiated in A occurs frequently. On the other hand, the probability $P(\alpha_B|\alpha_0)$ is still very small to be computed using direct MD simulations. To remedy this problem we write

$$P(\alpha_A|\alpha_0) = \prod_{i=0}^{n-1} P(\alpha_{i+1}|\alpha_i)$$

where the product is over all interfaces and $P(\alpha_{i+1}|\alpha_i)$ is the conditional probability of a trajectory initiated at the α_i interface reaching the α_{i+1} interface. Now even if $P(\alpha_A|\alpha_0)$ is small, we have broken it into many factors of probabilities $P(\alpha_{i+1}|\alpha_i)$ that, if the order parameter was chosen wisely, will not be numbers so small. Thus the final equation for the rate constant is

$$k_{AB} = \phi_{A,0} \prod_{i=0}^{n-1} P(\alpha_{i+1}|\alpha_i). \tag{3.33}$$

It remains to be shown how to compute these values from the FFS simulation. If the first interface α_0 is chosen correctly, the flux $\phi_{A,0}$ can be computed by brute force MD, since the probability of crossing A

is not too small. In fig.3.20 this corresponds to the gray trajectory. Notice how the stored configurations are those coming from inside A directed at the next interface. This is important since the configurations in the opposite direction will always return to A. The flux $\phi_{A,0}$ is then computed as the number of stored configurations divided by the simulation time. The probabilities $P(\alpha_{i+1}|\alpha_i)$ are estimated as the number of trajectories initiated in α_i that reached α_{i+1} divided by the total number of trajectories shot.

Using the same trajectories obtained to compute k_{AB} we can compute the free-energy barrier by using the Umbrella Sampling (Frenkel and Smit, 2001) method that works quite naturally with FFS (Valeriani et al., 2007; Allen et al., 2009; Borrero and Escobedo, 2009). All that is necessary is to define the windows used in the Umbrella Sampling as the interfaces interval of FFS. If the order parameter used is chosen to be the same for both methods the match between the methods is statistically better than if the order parameters are different. Asides from the transition rate k_{AB} and the free-energy barrier the FFS method also allows us to obtain samples of transition trajectories that can be used to better understand the mechanism of the transition.

Now we describe our attempts to apply the FFS method to study the kinetics of the martensitic phase transition. The initial and final states A and B are chosen according to fig.3.12 as the BCC and FCC structures, respectively. The Langevin thermostat was used to guarantee the stochasticity of the dynamics between the interfaces. We have chosen to use the MEAM potential of Lee et al. (2012) because it was the only potential to show the correct phase stability order, with FCC being more stable than HCP. The main problem we faced was the choice of the order parameter. Because FFS relies strongly on the definition of the order parameter α, a good choice will increase the efficiency of the method while a poor one can lead to wasted efforts and even wrong results (Allen et al., 2009). In the case of the Martensitic phase transition we need an order parameter that differentiates between different crystal structures even under conditions of thermal agitation. We have used the *Steinhardt order parameter* introduced by Steinhardt et al. (1983). To each atom i we assign a complex vector Q_{lm} defined as

$$Q_{lm}(i) = \frac{1}{N_b(i)} \sum_{j=1}^{N_b(i)} Y_{lm}(\mathbf{r}_{ij})$$

where $N_b(i)$ is the number of nearest neighbors of particle i, the sum is over all nearest neighbors, $Y_{lm}(\mathbf{r}_{ij})$ are the spherical harmonics and $\mathbf{r}_{ij}$ is the distance vector from particle i to particle j. Because of the crystal symmetries we need an order parameter that is rotationally invariant. Therefore we define the rotationally invariant combination

$$q_l(i) = \sqrt{\frac{4\pi}{2l+1} \sum_{m=-l}^{l} |Q_{lm}(i)|^2} \tag{3.34}$$

as the *Steinhardt order parameter* of atom i. This order parameter is going to be used to create an order parameter for the FFS simulation. In Bravais lattices the position of all atoms are equivalent and therefore all of them have the same configuration of nearest neighbors. This implies that the Steinhardt order parameter is the same for all atoms in the structure. According to Steinhardt et al. (1983) a good choice of the l number to differentiate between crystalline structures is $l = 4$, for which we obtain the following values for the perfect crystals (zero temperature)

$$q_4^{BCC} = 0.50918 \qquad q_4^{BCC-14} = 0.03637$$
$$q_4^{FCC} = 0.19094 \qquad q_4^{HCP} = 0.09722$$
$$q_4^{SC} = 0.76376.$$

We define the Global Steinhardt (GS) order parameter as the average of eq.(3.34) over all atoms of the system. To check how does this order parameter behaves when we add temperature to the crystal we computed its average for different crystal structures using the MEAM potential at 1000K. The results are shown in fig.3.21 (left). We see that the GS order parameter has very narrow distributions around well defined values (solid lines) and that the average value of each distribution is shifted from the average value of the perfect crystal. The BCC-14 curve is the BCC structure in which we have included the second shell of neighbors in the computation.

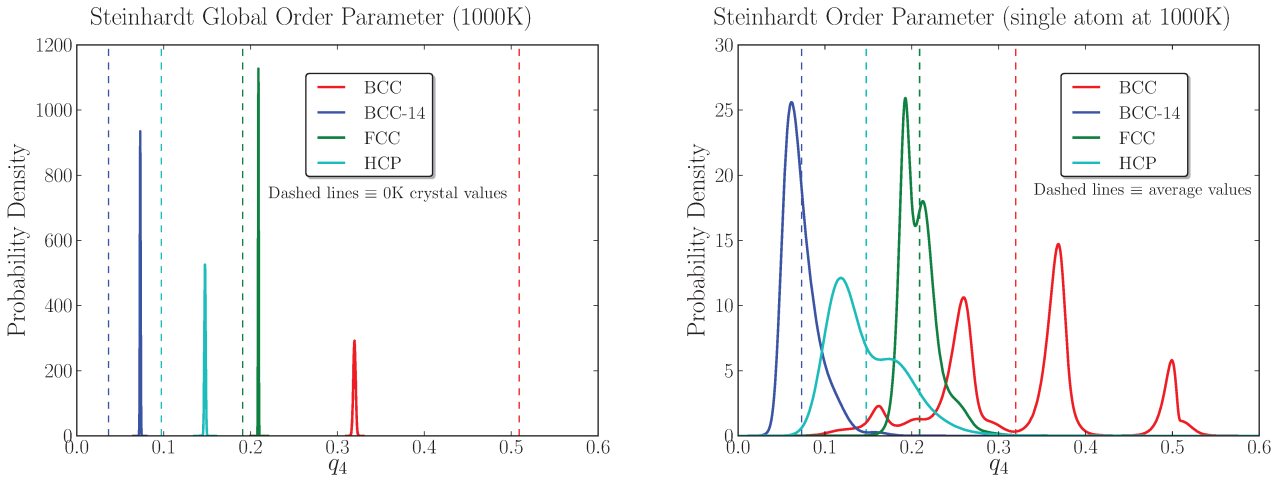

Figure 3.21: **Left:** Global and **Right:** Local Steinhardt order parameter average value for a crystal at 1000K.

Thus, using the GS order parameter we can clearly differentiate between two crystal structures, even when including the effect of temperature on the system. We then performed a FFS simulation using 2000 atoms and the MEAM potential. To facilitate the transition to occur we overheated the system at temperatures up to 1800K. Although the FFS method does work (the crystal changes its structure) it

seems that this GS order parameter is too flexible to conduct the crystal to the correct structure. Because we are only measuring the average over many atoms it is possible that we are giving too much freedom for the atoms to choose the value of this order parameter and the final result is an amorphous structure where atoms assume values of the order parameter over a large range of values, some of them does not even representing any know crystalline structure. An example of the final structure after a FFS is shown in fig.3.22, the initial structure was an equilibrated BCC structure at 1800K.

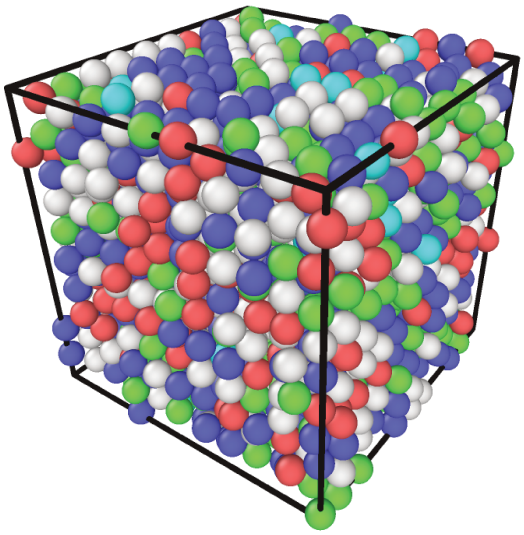

Figure 3.22: Example of the final structure obtained after an FFS simulation using the GS or the LS order parameter. The different colors mean that the structure around an atom is closer to a specific symmetry. Green represents FCC, red is HCP, purple is BCC and blue is an icosahedral structure. The white color is reserved for all values of the Steinhardt order parameter, eq.(3.34), without a respective lattice geometry associated to it.

To better understand why the GS order parameter do not work lets analyze the Steinhardt order parameter distribution of a single atom during a simulation at 1000K, shown in fig.3.21 (right). We now see that this distribution is not as narrow and not even centered around its average value (dashed lines), as for example in the case of the BCC structure where we have obtain three different and separated peaks in the distribution. In this graph we notice that the BCC-14 and the FCC curves have almost no overlap, not even at temperatures close to the phase transition temperature.

Our next step is to try to reduce the freedom for the atoms to choose the value of the order parameter. Instead of using the GS order parameter our idea now is to use the Steinhardt order parameter of each atom, eq.(3.34) or fig.3.21 (right), to identify the crystalline structure around this atom. For example, we defined an atom as in the BCC structure if its Steinhardt order parameter lies between 0.3 and 0.6.

Thus we are able to count the number of atom in each structure and then to use the number of atoms in the new phase as the order parameter for the FFS. To differentiate this order parameter from the GS order parameter we shall refer to it as *Local Steinhardt* (LS) order parameter. When we perform the FFS simulation the result was similar to the one found using the GS order parameter, with the FFS leading our system to an amorphous phase. Therefore it seems that even the LS order parameter gives too much freedom to the system.

Finally we discuss some final ideas and possible solutions to this difficult problem. Lechner and Dellago (2008) have shown how the Steinhardt order parameter can fail to determine the crystal structure because of overlaps in its distribution for different structures. They also suggest an *averaged local bond order parameter* that does solve some problems of the Steinhardt order parameter and narrow the distribution of fig.3.21 (right). This is certainly more appropriate than the Steinhardt order parameter, given that narrower distributions and less overlaps facilitate the determination of the structure around one atom. Another possible solution that has shown to be promising is to assume Classical Nucleation Theory to be valid and to use the size of the largest cluster of the new phase (FCC in our case) as order parameter. Ryu and Cai (2010) have implemented this approach in an bidimensional Ising model system and many others (Borrero and Escobedo, 2009; Russo and Tanaka, 2012; ten Wolde et al., 1996) have used it to study liquid-solid phase transitions.

Chapter 4

Pauling's Model of Ice

We turn now to a different application of molecular simulation. In this chapter we present a new algorithm to generate disordered ice structures in accordance with the Bernal-Fowler ice rules. In section 4.1 we introduce the characteristics of ice Ih and show how we can study Pauling's model of ice from disordered ice structures created according to the Bernal-Fowles ice rules. Sections 4.2 and 4.3 contain the details about the ice network generator algorithm and its implementation. The remainder of the chapter is devoted to the analysis of the algorithm and comparison with results presented in the literature.

4.1 Ice Ih and Pauling's Model

Water is one of the most studied substances and this did not happen by chance. Approximately 70% of Earth's surface is covered by ice and it is known that the water cycle is of fundamental importance to the maintenance of life on Earth. Besides its importance from the biological standpoint, water is also important for other physical sciences, namely physics and chemistry.

The water molecule is one of the most simple molecules found in nature, but it still presents many interesting and curious phenomena. A single molecule is composed of an oxygen and two hydrogen atoms, fig.4.1 (left), summing up 10 electrons. Its geometry is such that for isolated molecules the oxygen-hydrogen bond has equilibrium length of $r_0 \approx 0.957\mathring{A}$ and angle $\alpha \approx 104.52^\circ$ (Petrenko and Whitworth, 1999). The oxygen atom is bonded to each hydrogen atom by a covalent bond. Most of the negative charge of the molecule is concentrated around the oxygen because its elevated electronegativity. Therefore, the molecule has a natural electric dipole of $p \approx 6.186 \times 10^{-30}\ Cm \approx 1.855\ D$.

Another important characteristic of the condensed phases of water is the presence of hydrogen bond. This bond is between the oxygen of a molecule and a hydrogen from another molecule, fig.4.1 (right). Each water molecule can have up to four hydrogen bonds linking it to other molecules. This bond affects

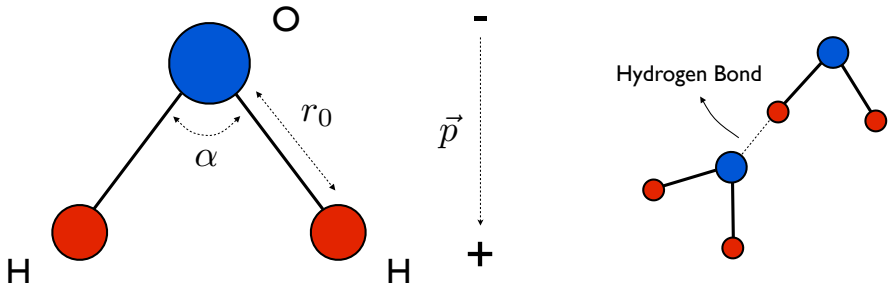

Figure 4.1: **Left**: water molecule. For the isolated molecule the oxygen-hydrogen covalent bond has length of $r_0 \approx 0.957\mathring{A}$ and angle $\alpha \approx 104.52°$. There is also an electric dipole of $p \approx 1.855D$ associated to the concentration of negative charge around the oxygen (Petrenko and Whitworth, 1999). **Right**: hydrogen bond in a water dimer.

many properties of water such as the high boiling temperature and melting point and surface tension as well as properties of the crystalline structures of ice.

Besides its liquid and gaseous phases water is present in 13 different crystalline phases, a few of them shown in the phase diagram of fig.3.10. In this chapter we will be concerned with the hexagonal proton-disordered phase of ice, known as ice Ih. This is the most common phase found on Earth due to its localization at low pressures in the phase diagram. The ice Ih crystal structure is obtained by putting each water molecule on a site of a wurtzite lattice (two interpenetrating HCP lattices) as shown in fig.4.2, such that each molecule has coordination four (four first neighbors). The unit cell of the wurtzite lattice has 8 atoms inside of it.

In addition to the position of each molecule we still have to establish its orientation. Because of the tetrahedral coordination of ice Ih, each water molecule can have six different orientations such that it has exactly four hydrogen bonds with its first neighbors. When choosing from these six possible orientations there are two rules that need to be obeyed. These are the Bernal and Fowler (1933) ice rules:

1. Each oxygen is covalently bonded to two hydrogen atoms.

2. The oxygen atom of each molecule forms two hydrogen bonds so that there is precisely one hydrogen atom between each pair of oxygens.

An ice Ih crystal that obeys these two rules is a perfect crystal. Any deviation from the rules is considered a defect, *e.g.* a disoriented molecule such that it has two hydrogen between a pair of oxygen atoms.

There is one more important characteristic of ice Ih that needs to be considered. There is no ferro-electricity in this phase of ice. This means that the dipole moment present in each water molecule does not have a preferential orientation, *i.e.* the total electric dipole moment of an ice Ih crystal is zero. In

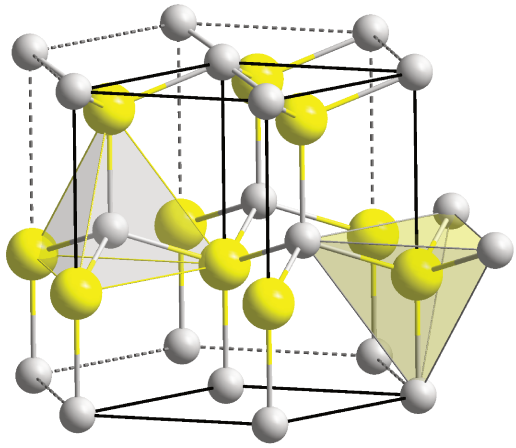

Figure 4.2: Wurtzite (ZnS) crystal structure. The ice Ih structure is obtained by putting one water molecule on each site of this lattice. The unit cell is composed of 8 atoms and the geometry around each atom is tetrahedral.

order to include this characteristic in his calculations Pauling (1935) created a model which has as the essential feature the absence of long-range order in the molecules orientations. In Pauling's model of ice all hydrogen bond configurations satisfying Bernal-Fowler ice rules are assumed to have the same statistical significance. The idea behind this model is that the energy of all these configurations is nearly equal so that no particular configuration will be stabilized at any temperature.

4.2 Ice Network Generator: Algorithm

The ice network generator is an algorithm designed and optimized to create ice lattices in accordance with the Bernal-Fowler ice rules. It makes use of a (pseudo) random number generator to ensure that the only correlation between the hydrogen bonds are those necessary to obey the ice rules. Because of the stochastic character of the algorithm the disordered ice structures created can be used to study the Pauling model of ice, which assumes that the statistical significance of all possible structures that satisfy the Bernal-Fowler rules is the same.

First, we are going to map the problem of creation of an ice lattice that obeys the ice rules into a problem of the creation of a directed graph (Rahman and Stillinger, 1972). In this graph each oxygen of the ice lattice is represented by a vertex. We associate to each vertex four neighbor vertices, because each water molecule has four first neighbors in the ice Ih. Between each neighbor vertices we have an undirected edge. We can organize this network into a 2D square array like in fig.4.3. Each hydrogen bond

is going to be represented by a directed edge. We define that each vertex of this graph needs to have two directed edges "entering" the vertex and two directed edges "leaving" the vertex. Notice that this is equivalent to the ice rules where each molecule forms two hydrogen bonds and receives two hydrogen bonds from a neighbor molecule. For simplicity we apply periodic boundary conditions to the ice crystal and, consequently, to its graph representation.

Now, the problem of creating an ice Ih crystal in accordance with the ice rules is equivalent to the problem of creating a directed graph that follows the rules just stated. Thus all we need to do is, starting from a completely undirected graph, determine one by one the directions of each edge. Because of the absence of long-range order in ice we want to determine the edge's direction in a random manner. It is easy to see that if we do not develop a good strategy we will soon find ourselves in a situation were the final graph cannot satisfy the stated rules. We describe now our algorithm to solve this problem.

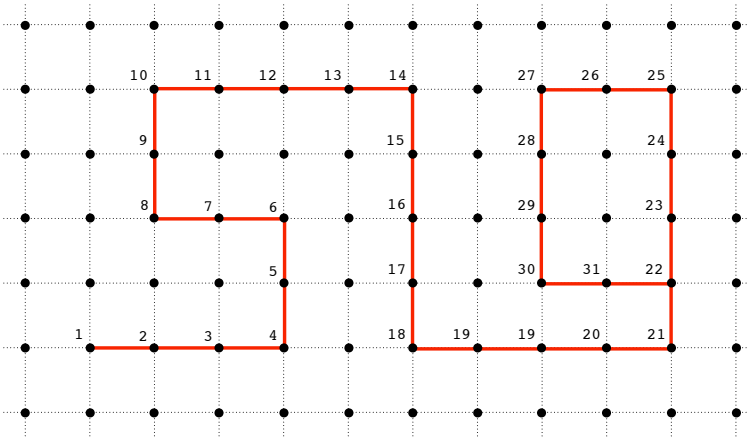

Figure 4.3: Ice network generation algorithm. The random walker stops only when the reaches a vertex that has been visited before. In this case the walker starts at vertex 1 and stops at the step 32 when he visits vertex 22 for the second time.

We start by randomly choosing a vertex. Starting from this vertex we perform a random walk though the graph keeping track of the path traveled by our walker, fig.4.3. The walker only stops when it reaches a vertex that has been visited before. In fig.4.3 we labelled the vertices visited by the walker by numbers. The walk starts at the vertex 1 and stops when vertex 22 is visited by the second time at step number 32. Once the walker stops it means that it has found a cycle. In fig.4.4 we shown this cycle in blue, it is composed of the vertices 22 through 32. Then the edges of this cycle are directed in the direction traveled by the walker. Once an edge is directed the walker cannot pass through that edge again, although we can (and will) pass through each vertex twice.

An important quantity in the algorithm is L_{path}, which is defined as the length of the walker's path

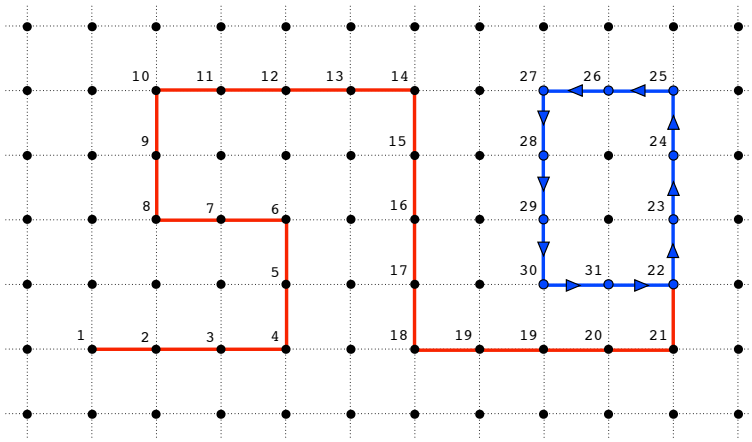

Figure 4.4: Ice network generation algorithm. Once a cycle is found we direct its edges according to the direction that the walker traveled through it. A directed edge cannot be traveled by a walker again.

(not including the cycle) that we will be stored for the next iteration. For example, in fig.4.4 if $L_{path} = 10$ we would erase the path from vertex 10 to vertex 22. Then we would put the walker at vertex 10 and continue the random walk from there. If the remaining path is shorter than L_{path} then the walk continues from the vertex immediately before the cycle, *e.g.* vertex 22 on fig.4.4. There are two important limits for this quantity. When $L_{path} = 0$ we do not store any data, we erase the entire path and start the random walk at a random vertex (that has not been crossed twice). The other limit is $L_{path} = \infty$, in which case we always store the entire path and continue the walk from the vertex immediately before the cycle.

By iterating over this procedure we to obtain a set of cycles that completely fill the graph according to the stated rules. We name this procedure "cyclic decomposition" of the undirected graph. The ice lattice can be created from this filled graph by choosing the position of the hydrogen according to the directed edges between the vertices.

From the structure of the directed graph we see that the total dipole moment of the cycles are zero. It will be different from zero only if the chain crosses the boundary of the crystal. Chains with zero dipole moment are the *cycles* and the chains with non-zero dipole are refered as *loops*. In the case where the final structure contains loops it is possible that the total dipole moment of the cell is different from zero. If this happens, we need to eliminate the total dipole moment of the cell. To do that we notice that, if we invert the direction of all edges of a cycle, the entire cell continues to obey the ice rules. If the cycle has dipole moment zero then nothing changes, if it has a nonzero dipole moment then by inverting the direction of all edges of the cycle we invert its dipole moment direction. We name the procedure of inverting a cycle's edges direction "flipping" of the cycle. The procedure to try to zero the dipole moment of a cell is to flip the cycles with nonzero dipole moment in such a way that the combination of its dipole

moments are zero. If we have N cycles with nonzero dipole then there are 2^N possible combinations.

4.3 Ice Network Generator: Technical Details

The ice network generator algorithm was implemented in a $\sim$ 3000 lines C++ code making full use of the object oriented capabilities of this language. The calculations implemented in the code include the cyclic decomposition of the graph, zeroing of the total dipole moment by combining the flipping of cycles, calculation of correlation functions (geometrical and topological) and output of the final structure in formats compatible with the MD code LAMMPS and the electronic structure code VASP. The calculations performed in the following sections make use of MPI parallelism to allow the verification of a wide interval of parameters.

Other minor features implemented in the code include a full double linked list to deal efficiently with the memory allocation, template classes to allow different data structure on nodes of the lists, ordering algorithms using linked lists, decimal to binary conversion, neighbor and cell list features to accelerate the crystal structure creation and different crystal lattices (ice Ih, VI and 2D square).

To make the code versatile all the features are compiled into a `libnG.a` library and easily included in any C++ program. Expansion and modification of the code is facilitated by the object oriented modulation.

Our goal is to use the ice network generator algorithm to generate ice Ih lattices and study the Pauling's model. We compare our results to those obtained by Rahman and Stillinger (1972), Hayward and Reimers (1997) and Aragones et al. (2010). We are specially concerned with finite size effects since this is the first algorithm reported capable of creating large ice structures in a reasonable amount of time. Using our algorithm we were able to construct cells as large as $\sim 10^6$ atoms while the literature reports cells of a few thousand atoms ($\sim 10^3$) at most.

4.4 L_{path} effects

Regarding the implementation of the algorithm we want to determine the effects of the remainder path L_{path} in the results, *i.e.*: after our random walker finds a cycle should we keep or discard the non-cyclic part of the path? From the point of view of efficiency it is clear that it is very profitable to keep at least one vertex of the remainder path. It avoids the reconstruction of the non-directed edges table after each cycle is found, this results in an overall better performance. Fig.4.5 (left) shows the performance for different values of L_{path}.

It is quite clear that the size of the remainder path affects the result of the algorithm. We can check

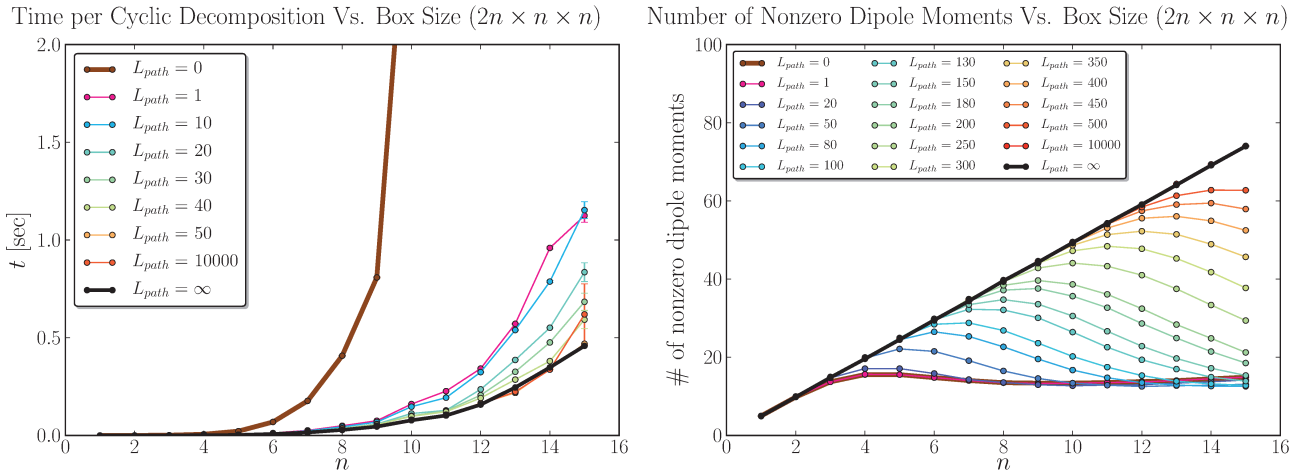

Figure 4.5: **Left**: algorithm performance. The numbers in the legend are the length of the remaining path after a cycle is found, ∞ means that nothing is discarded, 0 means that the whole path is discarded and 1 means that only one vertex (the last one, just before the cycle) is kept. **Right**: number of nonzero dipole moments for systems of different sizes, it is interesting that the number of nonzero dipoles is stable (≈ 18) after a certain size for sorter values of L_{path} while it scales linearly for L_{path}

in fig.4.5 (right) that the number of nonzero dipole moments scales linearly with the size of the system if we do not discard any vertex of the path ($L_{path} = \infty$). If we delete the whole path (or keep only part of it) then the number of nonzero dipole moments stabilizes at ≈ 18.

In fig.4.6 we show the probability density distribution of cycle lengths. On the left we have a system with the same dimensions as in Rahman and Stillinger (1972) and on the right we have a system with larger dimensions (approximately a cube). There are a few points to mention in this figure:

1. The average value of the cycle length has an apparent dependency on the box size.

2. Results for keeping one vertex or zero vertices are in agreement (inside the error bar) but the average value of the cycle length is greater in the case where we keep all the remainder path ($L_{path} = \infty$).

3. Although the result is qualitatively the same as in Rahman and Stillinger (1972) we notice that quantitatively the average value of the cycle length is greater than $\langle l \rangle = 10.24$, the result reported by Rahman and Stillinger (1972) (no error bars were reported).

Item 1. is expected from any finite size simulation. To confirm this dependency we computed the average cycle length dependency on the simulation box size. In fig.4.7 we see that this dependency is real and not considered in the literature. We see that the convergence of the result is achieved with sizes larger than the one used in Rahman and Stillinger (1972) or any other result in the literature.

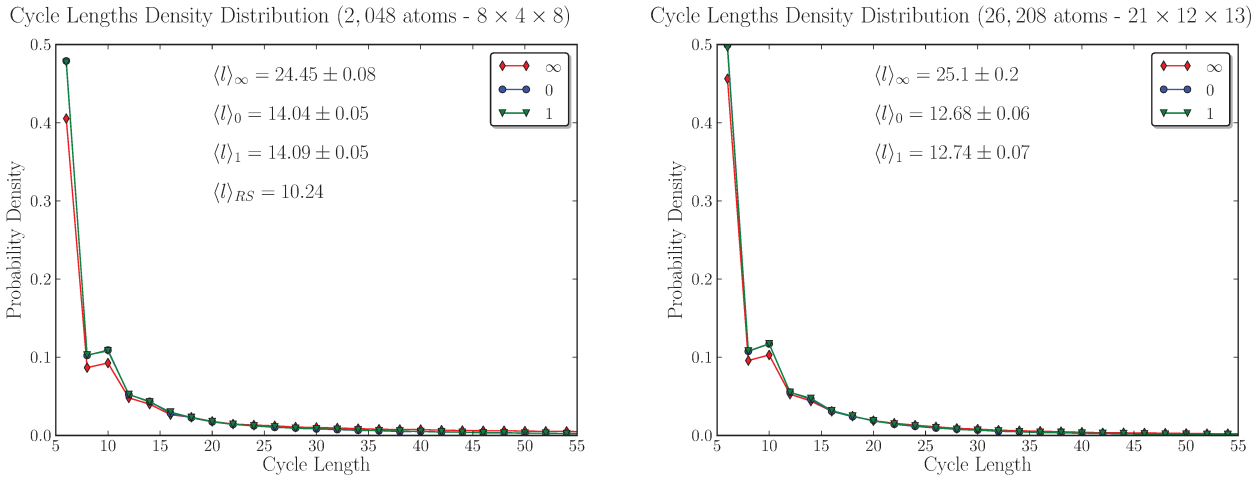

Figure 4.6: Cycle lengths probability density, on the **right** we used a large system (lattice is approximately a cube) and on the **left** we used the same system as Rahman and Stillinger (1972), their reported result is $\langle l \rangle = 10.24$, no error bar.

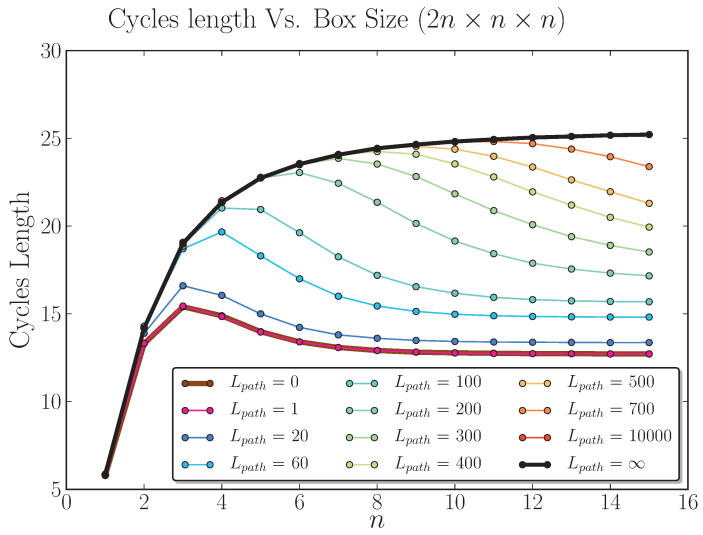

Figure 4.7: Average cycle length dependency on the box size.

Item 2. is also expected, being a natural consequence of keeping the remaining path. We allow for larger cycles to exist and become more likely. Also, the agreement between $L_{path} = 0$ and $L_{path} = 1$ is expected: keeping only one vertex should not result in larger cycles because the smallest possible cycle has size 6. Therefore, we should not expect to see any difference if we keep 5 or less vertices.

We can suggest a possible explanation for item 3. Rahman and Stillinger (1972) do not allow cycles to cross the boundary an odd number of times since these result in a nonzero total dipole moment for the system. This is not the case here, allowing all cycles to exist in the box. As we noticed the $L_{path} = \infty$

algorithm has two implications: greater number of cycles with nonzero dipole moment and greater average value of the cycle length. If we assume that the greater value for the cycles length comes from the cycles with nonzero dipole (that are more numerous in the $L_{path} = \infty$ structure) then it is reasonable that the suppression of these nonzero dipole moment cycles will result in an underestimated value of $\langle l \rangle$, just as obtained in Rahman and Stillinger (1972).

4.5 Dipole-Dipole Correlations

In order to further analyze our algorithm and compare it with the results of the literature we define a number of useful quantities to be computed. The dipole-dipole pair correlation function is defined as

$$\phi_n = \frac{\sum_{i=1}^{N} \sum_{j=1}^{i} \mathbf{p}_i \cdot \mathbf{p}_j \, \delta(R_{ij} - r_n)}{\sum_{i=1}^{N} \sum_{j=1}^{i} \delta(R_{ij} - r_n)} = \frac{1}{N} \sum_{i=1}^{N} \mathbf{p}_i \cdot \langle \mathbf{p} \rangle_{i,n}$$

where R_{ij} is the distance between the nearest images of the oxygen atoms of molecules i and j, r_n is the radius of the coordination shell n, $\mathbf{p}_i$ is the direction (unit vector) of the dipole of the molecule i and $\langle \mathbf{p} \rangle_{i,n}$ is the mean value of the dipole moment of atoms in the nth coordination shell of the molecule i. The Kirkwood correlation factor (Hayward and Reimers, 1997) is then defined as:

$$g = \sum_{n=0}^{\infty} C_n \, \phi_n$$

where C_n is the shell coordination number (number of molecules inside that shell).

For the subsequent analysis of ϕ_n and g we to refer to Hayward and Reimers (1997) instead of Rahman and Stillinger (1972) because the former includes and amplifies the results obtained in the latter. Hayward and Reimers (1997) discuss the implementation of a recursive algorithm to generate ice structures. Subsequent to the creation of the lattice they make use of simulated annealing combined with certain constraints to create a lattice with zero dipole moment. They have strict criteria to assure that the generated lattice is as random as possible and are in agreement with the results of Rahman and Stillinger (1972). The largest cell that they were able to create has 768 molecules . We are going to compare the results of this $6 \times 4 \times 4$ (768 atoms) cell and the $8 \times 4 \times 8$ (2,048 atoms) cell from Rahman and Stillinger (1972) with our results for the same cells and we also include a larger one of $21 \times 12 \times 13$ (26,209 atoms) to verify size effects in the simulation.

It is possible to compute ϕ_1 analytically for a random ensemble of water dimers in any orientation, the result is $\phi_1 = 1/3$. This is therefore a good indicative of how random our lattice is. It is cited in Hayward and Reimers (1997) that the value of 0.310 obtained in Rahman and Stillinger (1972) differs from 1/3 due to constraints associated with the ring formation. In addition we believe that the elimination of cycles that cross the boundary may also contribute to a value smaller than 1/3 as well.

First of all we computed the correlation function and the Kirkwood parameter for the large $21\times12\times13$ (26, 208 atoms) cell using the three different algorithm options ($L_{path} = 0, 1, \infty$). The result is shown in fig.4.8 (error bars are too small to appear). The ϕ_1 correlation parameter indicates that the algorithm that generates the network with minimum correlation is the one in which we keep the entire remaining path ($L_{path} = \infty$). We can also see that the $L_{path} = 0$ and 1 options have the same results (inside de error bar). We computed the correlation function for the same system but without the flipping procedure to obtain the network with zero dipole moment. The result is the same within the error bar.

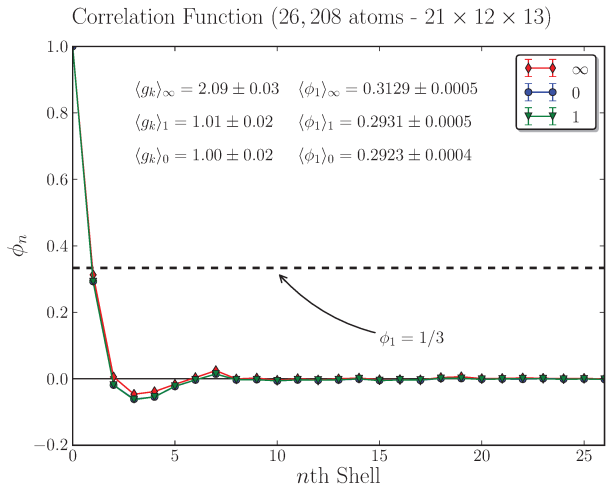

Figure 4.8: Correlation function and Kirkwood parameter for a large ($21\times12\times13$ (26, 208 atoms) system. The option of keeping the remainder path results in a network with minimum correlation (ϕ_1 closer to 1/3). Error bars are too small to appear.

In fig.4.9 we present the results for the same cells used by Rahman and Stillinger (1972) (left) and Hayward and Reimers (1997) (right). Here we also obtain the $L_{path} = \infty$ option as the one with minimum correlation, although we notice that ϕ_1 is considerably smaller than for the larger cell used in fig.4.8. The Kirkwood parameter of the $8 \times 4 \times 8$ (2, 048 atoms) system is close to the one obtained in Rahman and Stillinger (1972). The $6 \times 4 \times 4$ (768 atoms) cell presented a parameter reasonably large when compared to Hayward and Reimers (1997). Due to the fact that those papers do not present error bars it is difficult to say if our results are compatible or not. During the simulations we have noticed that the value of g for these small cells varies considerably. Therefore the error of the values reported in the papers can be large. Just to give an idea of the fluctuations of g in the small system we would like to point out that for the small system we obtained 10^3 independent structures to compute g and for the large system we used only 10, nevertheless the error bar is about the same in both cases.

The most striking feature of figs. 4.8 and 4.9 is the difference between the obtained value for g and ϕ_1 for the small cells and the values obtained for the large cell. In fig.4.10 we analyse the convergence of the

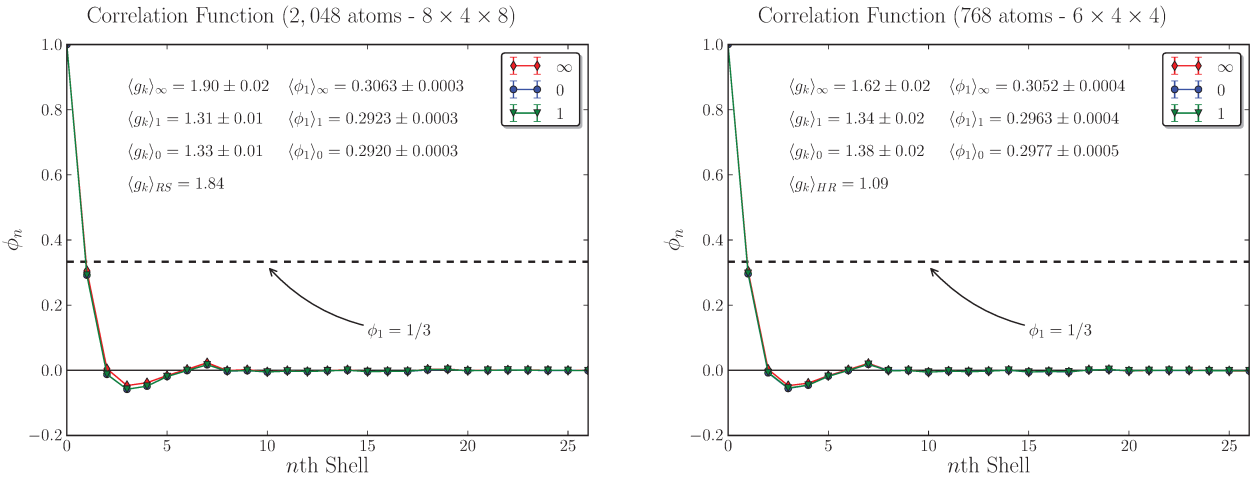

Figure 4.9: Correlation function and Kirkwood parameter for systems with size equal to those found in Rahman and Stillinger (1972) (**left**) and Hayward and Reimers (1997) (**right**). The option of keeping all the remainder path ($L_{path} = \infty$) results in a network with minimum correlation (ϕ_1 closer to 1/3). Error bars are too small to appear.

ϕ_1 (and consequently g) with the box size for different values of L_{path}. From this figure it becomes clear that finite size effects are present for the box sizes used by Rahman and Stillinger (1972) and Hayward and Reimers (1997). The convergence for $L_{path} = 0$ does not occur for sizes smaller than $16 \times 8 \times 8$ (8,192 atoms). For $L_{path} \neq 0$ finite size effects are present even for larger systems.

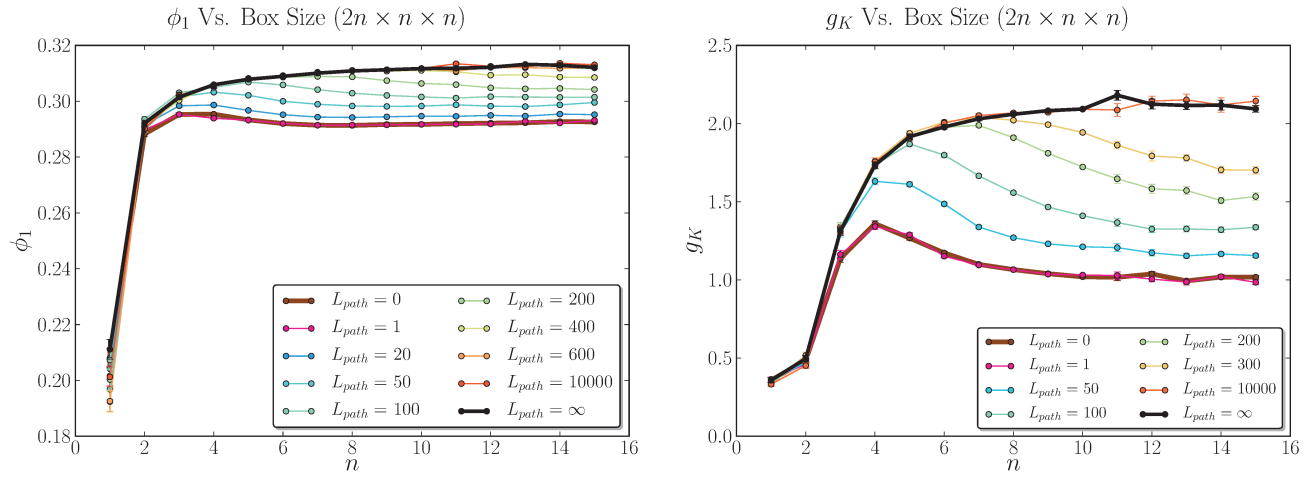

Figure 4.10: Analysis of finite size effects on (**left**) ϕ_1 and (**right**) g.

4.6 Exact Results for the Square Ice

Now that we have analyzed the effects of the remaining path on the results of the algorithm we are going to compare our algorithm with exact results available for a two dimensional square structure. In this section we are considering a $n \times n$ square lattice with $N = n^2$ atoms. The net polarization, $\mathbf{P}$, of a lattice is defined as

$$\mathbf{P} = \sum_{i=1}^{N} \boldsymbol{\mu}_i,$$

where $\boldsymbol{\mu}_i$ is the electric dipole of the molecule i. For *isotropic systems* Yanagawa and Nagle (1979) and Nagle (1979) defined the Kirkwood correlation factor g as

$$g \equiv \lim_{\Omega\to\infty} \lim_{V\to\infty} \frac{1}{\mu^2} \sum_{j \text{ in } \Omega} \left\langle \boldsymbol{\mu}_0 . \boldsymbol{\mu}_j \right\rangle, \tag{4.1}$$

where μ is the magnitude of the dipole moment. The summation is over a sphere Ω which becomes large, but only after the volume V of the system becomes infinitely large. This definition of the Kirkwood parameter is equivalent to the one given in a previous section but it has the advantage of being easy to generalize in the case of an anisotropic system. Notice that the self-correlation function $g^{(0)}$ is just the $j = 0$ term in eq.(4.1). In the same paper the authors define the polarization factor G for an isotropic system as

$$G \equiv \lim_{V\to\infty} \frac{1}{\mu^2} \sum_{j \text{ in } V} \left\langle \boldsymbol{\mu}_0 . \boldsymbol{\mu}_j \right\rangle, \tag{4.2}$$

where the summation extends over all correlations in the system.

We are going to use the correlation functions just presented to compare the results of our algorithm, fig.4.11, against exact results and previous simulations. Sutherland et al. (1967) have compute the exact value of the polarization factor for the square ice:

$$G = \frac{9}{\pi} = 2.8647\ldots.$$

Domb and Green (1972) obtained

$$g^{(0)} = 0.930$$

and Yanagawa and Nagle (1979) suggest that

$$g = 1.5 \pm 0.3.$$

In order to compare the results of our algorithm with the exact results of the square ice we need to consider the anisotropic characteristic of this lattice. Yanagawa and Nagle (1979) explain that eqs.(4.1)

and (4.2) are valid for isotropic systems, for systems of lower symmetry correlation functions of the type $\sum_j \langle \boldsymbol{\mu}_0.\boldsymbol{\mu}_j \rangle$ must be replaced by the more fundamental form

$$\sum_j 3(\boldsymbol{\mu}_0.\hat{\mathbf{e}}_E)(\boldsymbol{\mu}_j.\hat{\mathbf{e}}_E),$$

where $\hat{\mathbf{u}}_E$ is the unit vector along the electric field $\mathbf{E}$ (*i.e.* the direction in which we want to compute the correlations).

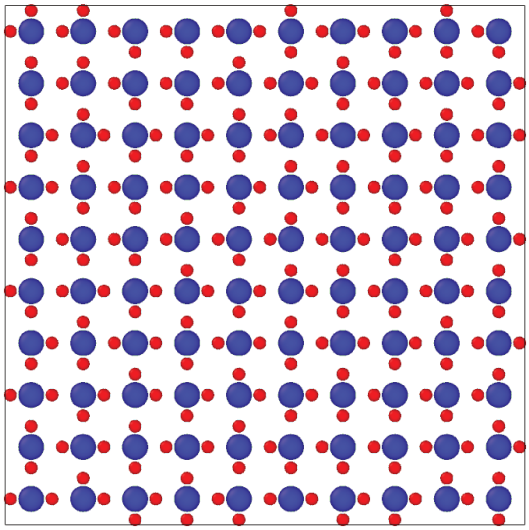

Figure 4.11: Example of a square ice lattice created using the ice network generator algorithm. The blue atoms are the oxygen and the red ones are the hydrogens.

One feature introduced by this asymmetry of the two dimensional square ice is that the six different water molecule configurations do no have the same probability. An exact calculation (Domb and Green, 1972) shows that configurations with zero dipole moment have occurrence probability of 19% while the other four have 15.5%.

4.7 Simulations for the Square Ice

We now start to compare the results of our algorithm with the results obtained by Yanagawa and Nagle (1979) and our own Monte Carlo simulations that reproduces their results with better precision. To differentiate between the results we refer to our algorithm as NG (Network Generator, the name of the code we developed), YN (Yanagawa and Nagle (1979) results) and MC (our Monte Carlo implementation).

Because of the square symmetry of the lattice the correlation functions for E_x and E_y directions must be the same, we are going to use this condition to check the sampling efficiency of the code: only when

both directions result in the same value for the correlation functions (within the errors) we consider that the simulation has converged.

Yanagawa and Nagle (1979) used a Monte Carlo algorithm to compute correlation functions for the square ice. They have proved that their method is ergodic. In their algorithm they use a previous obtained square ice lattice to create new states of the system by creating and flipping cycles and loops. They discard the tail of the generated paths and we are going to do the same to try to "match" the results, *i.e.* we are using $L_{path} = 0$.

In their paper Yanagawa and Nagle (1979) introduce the definition of a **cycle** as a closed chain of dipoles that has total dipole moment equal to zero, **loops** are closed chains of dipoles that have total dipole moment different from zero. Therefore, when loops are inverted they change the net dipole **P** of the system. For a square lattice the components of the dipole moment of loops are multiples of $n(\mu/\sqrt{2})$. Also, there are no states with dipole moment equal to zero for n odd.

We start by checking the frequency of the six possible molecular configuration, fig.4.12. Our first observation is that the MC simulations are always closer to the exact result than the NG algorithm, although any of the lattice sizes resulted on the exact values.

Table 1: Frequency of Molecular Configurations

Lattice size	Config. 1	Config. 2	Config. 3	Config. 4	Config. 5	Config. 6
Exact	15.50	15.50	15.50	15.50	19.00	19.00
8x8 (NG)	15.42(6)	15.39(6)	15.62(7)	15.44(6)	19.07(4)	19.07(4)
8x8 (MC)	15.80(7)	15.73(7)	15.69(7)	15.66(7)	18.56(3)	18.56(3)
12x12 (NG)	15.01(4)	14.96(4)	15.00(4)	14.99(4)	20.01(2)	20.01(2)
12x12 (MC)	15.57(4)	15.66(4)	15.54(4)	15.65(4)	18.79(2)	18.79(2)
16x16 (NG)	14.80(3)	14.75(3)	14.82(3)	14.78(3)	20.42(2)	20.42(2)
16x16 (MC)	15.54(3)	15.54(3)	15.53(3)	15.56(3)	18.91(2)	18.91(2)

Figure 4.12: Frequency of molecular configuration compared with the exact results are of (Domb and Green, 1972).

Now we analyze statistic about the chains. In fig.4.13 we confirm that in both algorithms (Monte Carlo and NG) the percentage of loops drops as we increase the lattice size. This is a reasonably result since as we increase the lattice size the minimum size of a loop increases and therefore it becomes more difficult to obtain a chain of such size.

The increase of the minimum size of a loop with the increase of the lattice size can be seen by the drastic increase of the average length of loops in fig.4.13 while, in the same figure, the average length of the cycles does not increase as much. In fig.4.14 we analyze again the percentage of loops (left) and

Table 2: Distribution of Cycles and Loops Length			
Lattice size	**% of loops**	**Average loop length**	**Average cycle length**
8x8 (NG)	16.6	16.27(3)	5.48(1)
8x8 (MC)	14.0	15.288(4)	5.409(1)
8x8 (YN)	14.1	15.33	5.42
12x12 (NG)	5.4	28.3(1)	5.71(1)
12x12 (MC)	2.9	23.93(1)	5.518(1)
12x12 (YN)	3.0	23.83	5.53
16x16 (NG)	2.3	42.97(1)	5.86(1)
16x16 (MC)	0.6	32.32(3)	5.546(1)
16x16 (YN)	0.5	32.62	5.53

Figure 4.13: Statistics about the chains length, we compare our results with those of Yanagawa and Nagle (1979).

the average loop length (right) but now for a larger range of lattice sizes not available for Yanagawa and Nagle (1979). We confirm that the percentage of loops decreases rapidly with the lattice size and also that the average loop length increases drastically with the lattice size. It is interesting to observe that the MC and the NG algorithm have different dependencies on the average loop length with the size of the lattice. Also we can notice that for the MC algorithm the probability of having loops decreases much faster than for the NG algorithm, in such a way that for lattices with edge larger than 46 atoms we could not obtain any loop and therefore there is not statistics available for the average loop length.

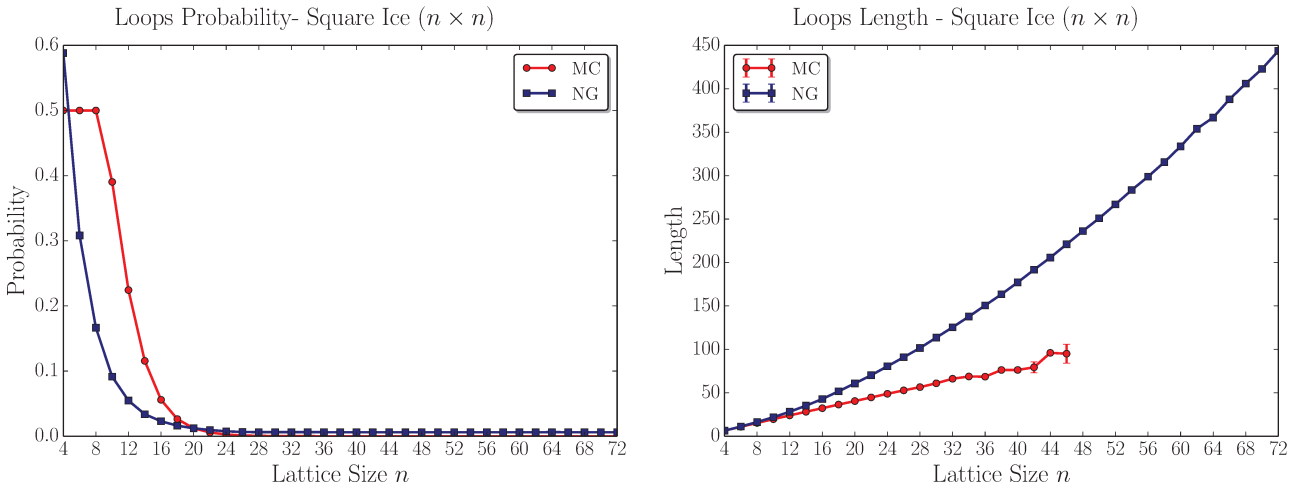

Figure 4.14: (**Left**) Percentage and (**right**) average length of loops for a larger range of lattices values.

The difference between the average loop length for both algorithms (fig.4.14) is interesting and make us think about the correctness of sampling of both algorithms. Fig.4.15 shows that the difference between the average length of the cycles is also different for both algorithms. The MC algorithm clearly shows a

plateau at a lower value than the NG algorithm. In fig.4.16 (left) we show the probability distribution of cycles and loops lengths for both algorithms, in this figure we can clearly see that the algorithms sample different distributions. Fig.4.16 (right) also shows that we can expect different values for the correlation

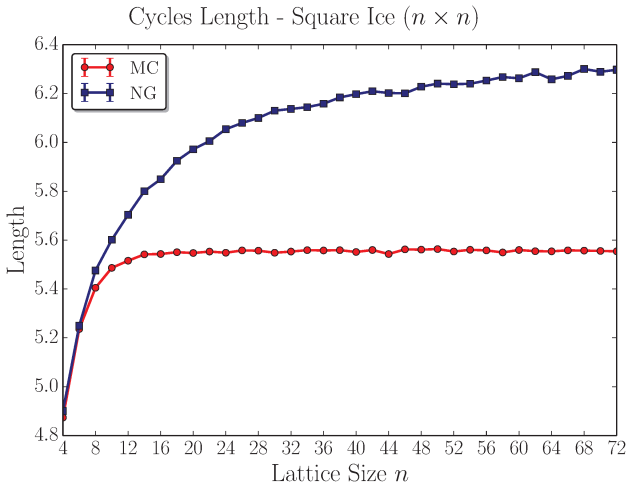

Figure 4.15: Average length of cycles for a large range of lattices values.

functions since the distribution of the dipole moment of the lattices is also different. This figure also illustrates the convergence test used, notice that the values of the dipole moment in the x and y direction are the same (as they should be by symmetry), this indicates the convergence of the results.

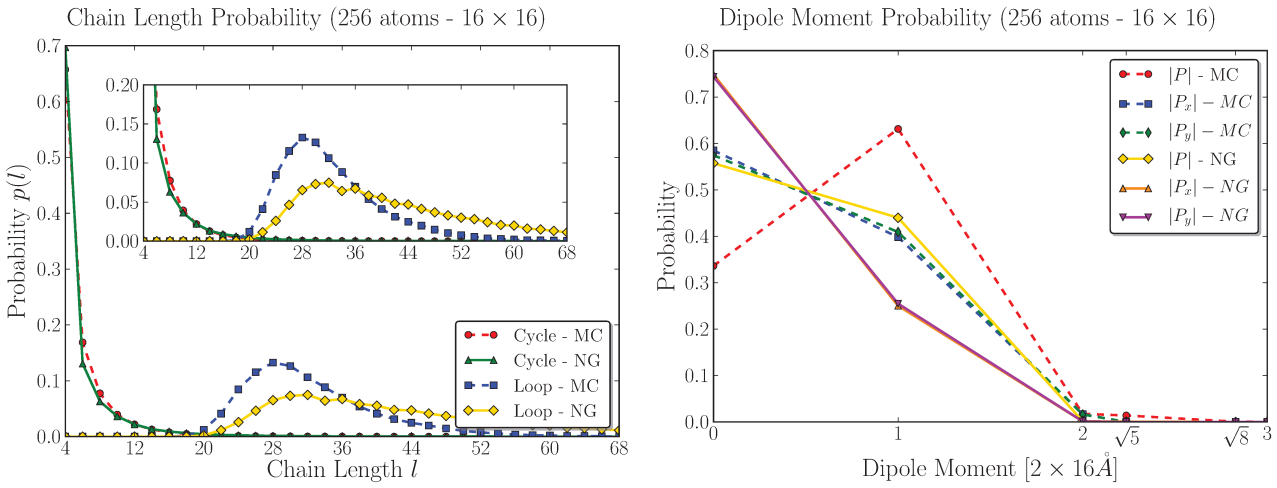

Figure 4.16: (**Left** Chain length probability distribution for loops and cycles. (**Right**) Dipole moment probability distribution for both algorithms.

To decide which algorithm correctly samples the Pauling's model of ice we computed the correlation functions presented in last section. In fig.4.17 we compare our results with the literature (Yanagawa and Nagle, 1979), we can see that the MC algorithm gives the correct values of the correlation functions while

the NG algorithm does not agree with the exact values. In this same figure we can see the origin of this difference, the number of states with zero polarization (n_0) and non-zero polarization (n_p) is approximately constant (0.33) for the Monte Carlo algorithm while it varies for the NG algorithm.

Table 3: Polarization Factor			
Lattice size	**n_0/n_p**	**G**	**$g^{(0)}$**
8x8 (NG)	0.37	2.60(4)	0.928(1)
8x8 (MC)	0.33	2.86(4)	0.943(1)
8x8 (YN)	0.33	2.88(4)	0.942(3)
12x12 (NG)	0.47	2.01(3)	0.900(1)
12x12 (MC)	0.33	2.84(4)	0.936(1)
12x12 (YN)	0.35	2.78(6)	0.937(1)
16x16 (NG)	0.56	1.56(3)	0.887(1)
16x16 (MC)	0.34	2.84(4)	0.933(1)
16x16 (YN)	0.33	2.86(11)	0.933(1)

Figure 4.17: Polarization factor for systems of different size. We compare our results with those of Yanagawa and Nagle (1979) and the exact values of $G = 9/\pi = 2.8647\ldots$ and $g^{(0)} = 0.930$.

Fig.4.18 shows the dependency of the correlation functions with the lattice size. We can see that both functions G and $g^{(0)}$ converge to values different from the exact result for the NG algorithm. The MC algorithm present the correct value of these functions but we can notice that the small probability of having loops for large lattices decreases the convergence of the statistics for the polarization factor. This result is expected once the convergence of the statistics of G depends on the sampling of lattices with different total dipole moment. Because it is difficult to obtain a loop for large lattices it becomes difficult to sample lattices with different dipole moments.

4.8 Ice Ih Structure and Polarization Factor

The results of last section shown that the NG algorithm does not generate ice structures that correctly sample the Pauling's model of ice. Despite this unfortunate result the NG algorithm still a powerful method to create new ice structures. Using this algorithm we can obtain statistically uncorrelated ice structures and by applying a few Monte Carlo steps to these structures we can recover structures that are uncorrelated and sample the Pauling's model of ice. Because the results of last section for the NG algorithm does not seem to improve with the use of L_{path} different from zero we can boost our algorithm performance by speeding the structure creation with the $L_{path} = \infty$ option and then use the (cheap) Monte Carlo flips to obtain the correct sampling. Therefore the NG algorithm still useful to efficiently

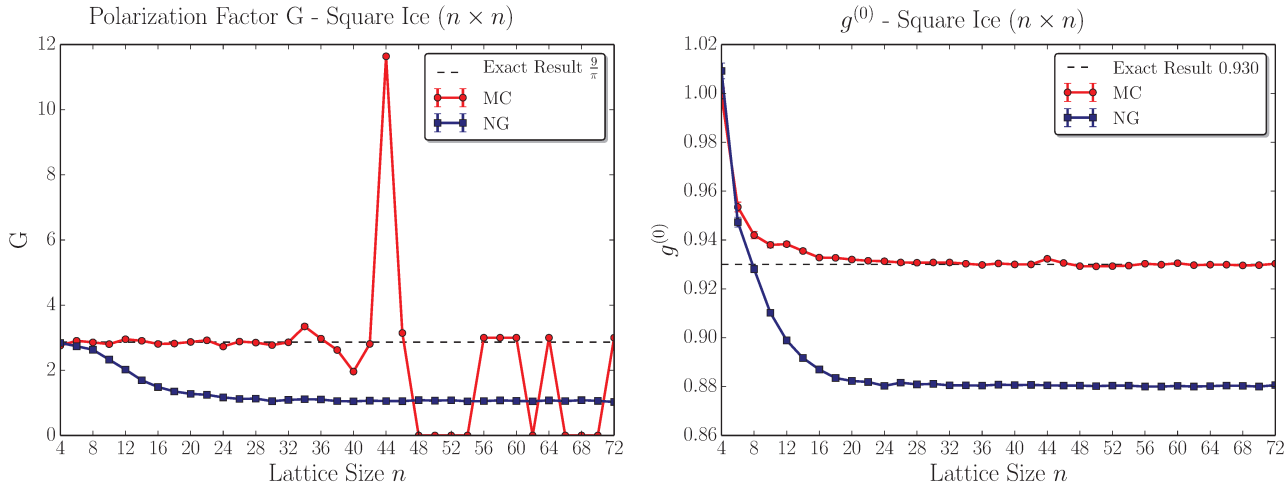

Figure 4.18: (**Left**) Polarization factor and (**right**) self-correlation function convergence with the lattice size.

create ice structures.

The last application of this algorithm that we are going to make is to compute the polarization factor G for the ice Ih using the method just explained to guarantee uncorrelated structures. There are no exact results for this structure of ice, although Aragones et al. (2010) have shown that $G = 3.02(4)$ with Monte Carlo simulations using a small lattice of $5 \times 3 \times 3$ (360 atoms). In fig.4.19 we confirm the result that $G = 3$ within the error bars for lattices of size up to $14 \times 7 \times 7$ (5488 atoms), for larger lattices the convergence is not good due to the small probability of obtaining loops in the Monte Carlo procedure.

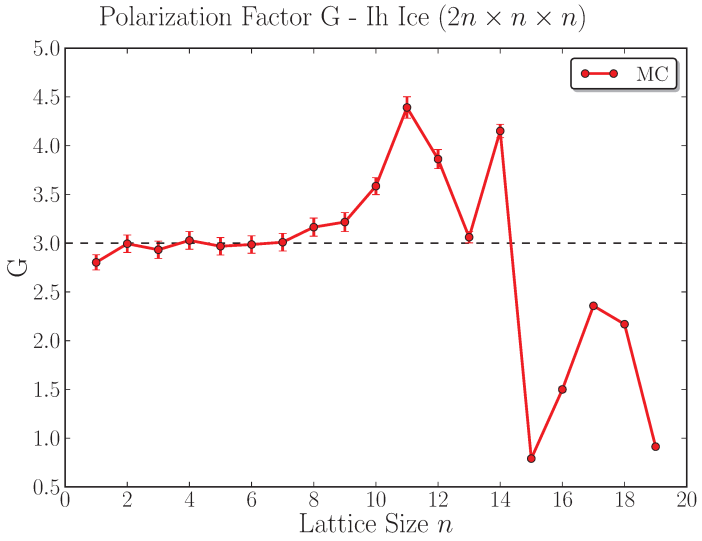

Figure 4.19: (**Left**) Polarization factor and (**right**) self-correlation function convergence with the lattice size.

Chapter 5

Conclusions and Outlook

5.1 Molecular Dynamics

We have presented the atomistic simulation technique of Molecular Dynamics and shown how we can use it to perform simulations controlling different thermodynamic variables of the system, such as temperature and pressure. Emphasis was put on the physical aspect of the methods and how to assure that the simulation has physical meaning. Particularly, the energy equipartition theorem was a very important criterion to verify the correct canonical sampling of the thermostats. We have discarded the use of the Nosé-Hoover chain thermostat due to its incorrect sampling for stiff systems like harmonic oscillators and the harmonic approximation of a crystal. The Langevin thermostat was used instead.

More advanced applications of Molecular Dynamics were used to study the first-order phase transition known as Martensitic phase transformation. A rigorous development of new features in the LAMMPS code was made to allow free-energy calculations. The methods of Frenkel-Ladd and the Reversible Scaling were implemented and successfully tested against the exact results for harmonic oscillators. Our final goal was to develop a systematic sequence of procedures that allowed the use of both methods to compute the temperature dependence of free energy accurately and efficiently. The Reversible Scaling allowed us to compute thus curve using only one simulation.

In the study of the thermodynamics of the Martensitic transformation we computed the free energy curves for the BCC, FCC and HCP phases of three different potentials (EAM, MEAM and ABOP) that presented the phase transformation. We conclude that the only potential that correctly reproduces the stability of phases was the MEAM potential. The other two describe the HCP phase to be more stable than FCC.

For the kinetics of the Martensitic transformation we implemented the rare-event method of Forward Flux Sampling. We were not able to reproduce this phase transformation using the method. Our main

conclusion is that the order parameter has an important role in this method. We studied the Steinhardt order parameter and its different variations as the order parameter but it seems that this particular order parameter gives the atoms too much freedom and the transition results in an amorphous solid.

5.2 Ice Network Generator

We have successfully implemented a new algorithm for the creation of disordered ice structures. Our focus was on the Ih phase of ice, the most abundant on Earth. To better understand the algorithm it was useful to map it to the problem of creating a directed graph were the ice rules are equivalent to the condition of two edges entering and two edges leaving each vertex. In the development of the algorithm and in the calculations our main concern was to not include any long range order on the structure. We have also developed a method to assure that the total dipole moment of the cell was zero by combining cycles with nonzero dipole moments in the correct manner.

Focus was given on the study of the finite size effects since all the results presented in the literature consider only small cells. Using our algorithm we were able to construct cells as large as $\sim 10^6$ atoms while the literature reports cells of a few thousand atoms ($\sim 10^3$) at most. We have found a strong size dependent effect for all quantities computed in the regime of cell size present in the literature (Rahman and Stillinger, 1972; Hayward and Reimers, 1997).

The parameter L_{path}, which is the length of the remaining path stored after a cycle is found, has a strong influence on the structure generated and on the finite size effects. We have indications that structures with $L_{path} = \infty$ are the ones with less correlation. Its ϕ_1 value is closer to a random structure than for any other value of L_{path}.

In order too assert which value of this parameter better represents the Pauling's model of ice we compared the results of our algorithm with the exact values for the two dimensional square ice lattice. Our final result is that although the algorithm does not correctly sample the Pauling's model of ice we can efficiently use it with to create ice structures. With the aid of a few Monte Carlo moves according to algorithms already know in the literature we can rapidly recover the correct sampling of Pauling's model of ice using our algorithm.

Appendix A

Switching Functions

In this appendix we briefly discuss the different options for the Thermodynamic Integration switching function that are included in commands implemented in LAMMPS.

A.1 Reversible Scaling

In the Reversible Scaling method we compute the dynamical work as

$$W^{dyn} = \int_0^{t_s} \frac{d\lambda}{dt}\, U(\mathbf{r}^N)\, dt,$$

where $\lambda(t)$ is the switching function with $\lambda(t=0) = \lambda_i$ and $\lambda(t=t_s) = \lambda_f$. The switching time is t_s. We implemented three different switching functions:

$$\begin{aligned} \lambda_1(\tau) &= \lambda_i + \tau(\lambda_f - \lambda_i), \\ \lambda_2(\tau) &= \frac{\lambda_i}{1 + \tau\left(\frac{\lambda_i}{\lambda_f} - 1\right)} \text{ and} \\ \lambda_3(\tau) &= \frac{\lambda_i}{1 + \log_2(1+\tau)\left(\frac{\lambda_i}{\lambda_f} - 1\right)} \end{aligned} \tag{A.1}$$

where $\tau = t/t_s$. All three of them respect the boundary conditions, *i.e.* $\lambda_i(\tau=0) = \lambda_i$ and $\lambda_i(\tau=1) = \lambda_f$ for $i = 1, 2$, or 3. The switching functions variation with time are given by

$$\begin{aligned} \frac{d\lambda_1}{dt} &= \frac{\lambda_f - \lambda_i}{t_s}, \\ \frac{d\lambda_2}{dt} &= \frac{\lambda_2(\tau)^2}{t_s}\left(\frac{1}{\lambda_i} - \frac{1}{\lambda_f}\right) \text{ and} \\ \frac{d\lambda_3}{dt} &= \frac{\lambda_3(\tau)^2}{t_s}\left(\frac{1}{\lambda_i} - \frac{1}{\lambda_f}\right)\frac{1}{(1+\tau)\ln 2}. \end{aligned} \tag{A.2}$$

Using these switching functions the temperature variation during a RS simulations is given by

$$T(t) = \frac{T_0}{\lambda(t)} \qquad \Rightarrow \qquad \frac{dT}{dt} = -\frac{T_0}{\lambda^2(t)}\frac{d\lambda}{dt}$$

where T_0 is reference temperature at which the simulation is performed. With these equations we can compute the temperature variation during the simulation:

$$\begin{aligned}
\frac{dT_1}{dt} &= \frac{T_0}{\left[\lambda_i + \tau(\lambda_f - \lambda_i)\right]^2}\frac{\lambda_i - \lambda_f}{t_s}, \\
\frac{dT_2}{dt} &= \frac{T_0}{t_s}\left(\frac{1}{\lambda_f} - \frac{1}{\lambda_i}\right) = cte \text{ and} \\
\frac{dT_3}{dt} &= \frac{T_0}{t_s}\left(\frac{1}{\lambda_f} - \frac{1}{\lambda_i}\right)\frac{1}{(1+\tau)\ln 2}.
\end{aligned} \tag{A.3}$$

As an example a short RS simulations were run using an Einstein crystal. The simulation temperature was $T_0 = 100K$ and the λ boundaries were $\lambda_i = 1.0$ and $\lambda_f = 0.1$. These parameters result in a final temperature of $T_f = 1000K$ after $t_s = 1000$ switching steps. The values of λ for each switching function, eq.(A.1), and its derivative, eq.(A.2) are shown in fig.A.1. The temperature $T(\tau)$ and its derivatives, eq.(A.3), are shown in fig.A.2.

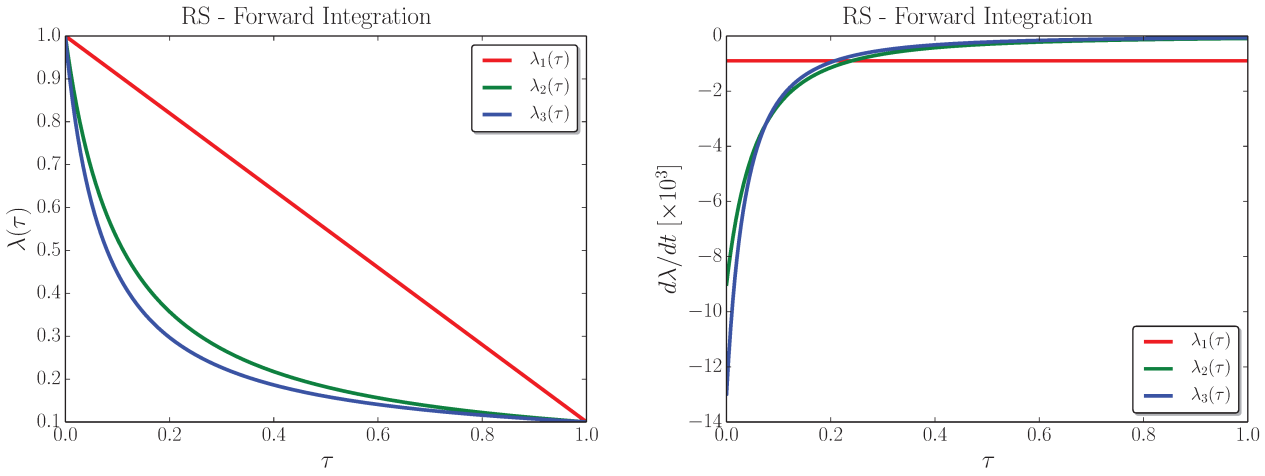

Figure A.1: Values of λ (**left**) and its time derivative (**right**) for each of the three proposed switching functions during a short ($t_s = 1000$ steps) RS simulation.

A.2 Frenkel-Ladd

In the Frenkel-Ladd method we compute the dynamical work

$$W^{dyn} = \int_0^{t_s} \frac{d\lambda}{dt}\ \left[U(\mathbf{r}^N) - U_{harm}(\mathbf{r}^N)\right]\ dt,$$

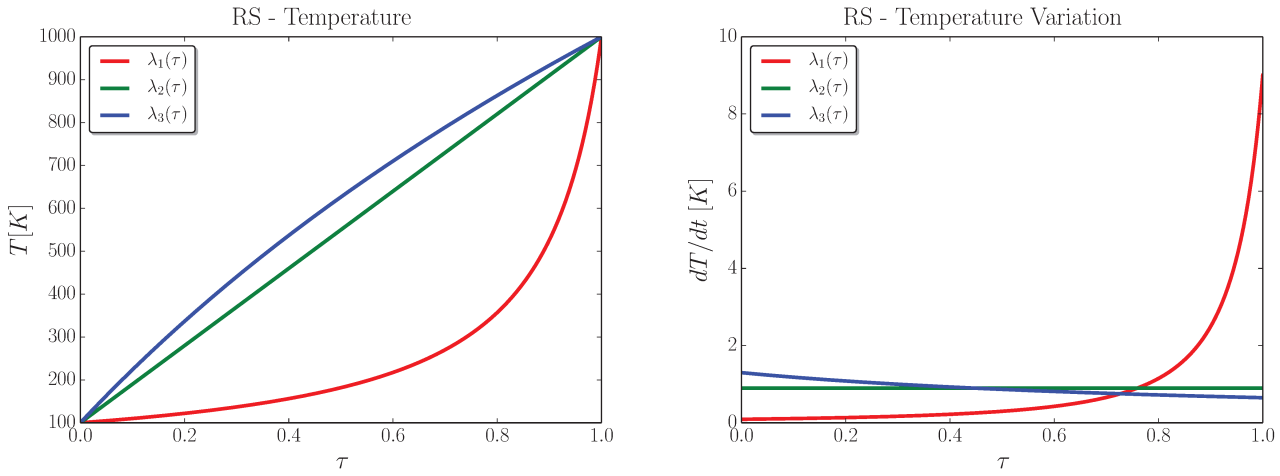

Figure A.2: Values of the temperature (**left**) and its time derivative (**right**) for each of the three proposed switching functions during a short ($t_s = 1000$ steps) RS simulation.

where $\lambda(t)$ is the switching function with $\lambda(t = 0) = 0$ and $\lambda(t = t_s) = 1$. The switching time is t_s. We implemented here two different switching functions:

$$\begin{aligned} \lambda_1(\tau) &= \tau \qquad \text{and} \\ \lambda_2(\tau) &= \tau^5(70\tau^4 - 315\tau^3 + 540\tau^2 - 420\tau + 126) \end{aligned} \tag{A.4}$$

where $\tau = t/t_s$. Both of them respect the boundary conditions $\lambda_i(\tau = 0) = 0$ and $\lambda_i(\tau = 1) = 1$ for $i = 1$ or 2. The switching functions variation with time are given by

$$\begin{aligned} \frac{d\lambda_1}{dt} &= \frac{1}{t_s} \qquad \text{and} \\ \frac{d\lambda_2}{dt} &= \frac{\tau^4}{t_s}(630\tau^4 - 2520\tau^3 + 3780\tau^2 - 2520\tau + 630) \end{aligned} \tag{A.5}$$

As example we ran short simulations using an Einstein crystal. The values of λ for each switching function, eq.(A.4), and its derivative, eq.(A.5) are shown in fig.A.3.

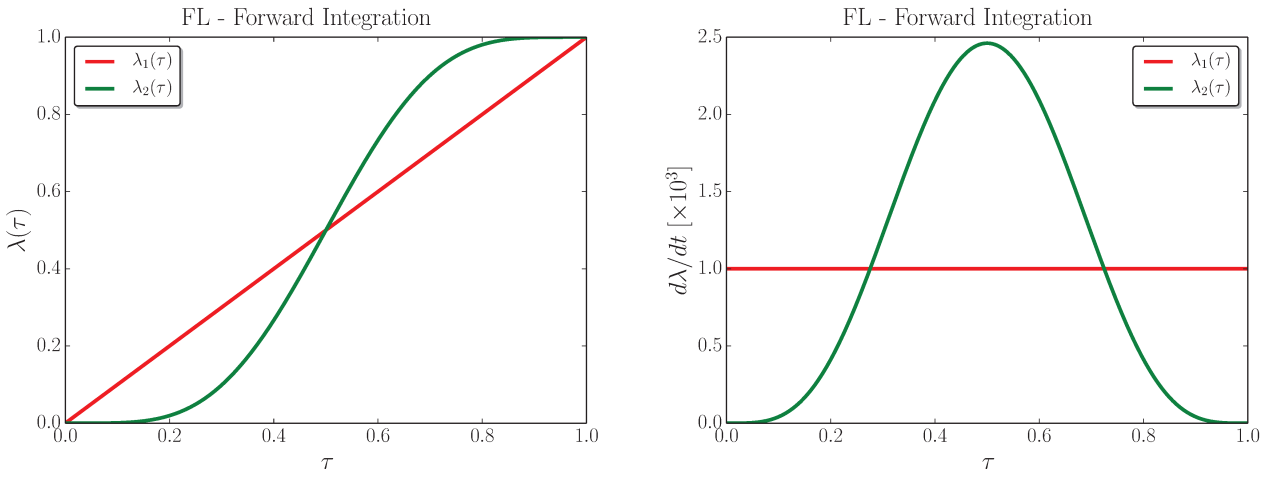

Figure A.3: Values of λ (**left**) and its time derivative (**right**) for each of the two proposed switching functions during a short ($t_s = 1000$ steps) FL simulation.

Bibliography

G. J. Ackland. Mechanical properties: Overcoming old barriers. *Nature Materials*, 11(10):837–838, 2012.

D. Adams. *The Hitchhiker's Guide to the Galaxy*. 1979-1992.

B. J. Alder and T. E. Wainwright. Phase transition for a hard sphere system. *The Journal of Chemical Physics*, 27(5):1208–1209, 1957.

B. J. Alder and T. E. Wainwright. Studies in molecular dynamics. i. general method. *The Journal of Chemical Physics*, 31(2):459–466, 1959.

M. P. Allen and D. J. Tildesley. *Computer simulation of liquids*. Oxford university press, 1989.

R. J. Allen, P. B. Warren, and P. R. Ten Wolde. Sampling rare switching events in biochemical networks. *Physical Review Letters*, 94(1):018104, 2005.

R. J. Allen, D. Frenkel, and P. R. Ten Wolde. Forward flux sampling-type schemes for simulating rare events: Efficiency analysis. *The Journal of Chemical Physics*, 124:194111, 2006.

R. J. Allen, C. Valeriani, and P. R. ten Wolde. Forward flux sampling for rare event simulations. *Journal of Physics: Condensed Matter*, 21(46):463102, 2009.

H. C. Andersen. Molecular dynamics simulations at constant pressure and/or temperature. *The Journal of Chemical Physics*, 72(4):2384, 1980.

P. W. Anderson. More is different. *Science*, 177(4047):393–396, 1972.

J. L. Aragones, L. G. MacDowell, and C. Vega. Dielectric constant of ices and water: a lesson about water interactions. *The Journal of Physical Chemistry A*, 115(23):5745–5758, 2010.

N. W. Ashcroft and N. D. Mermin. *Solid state physics*. Cengage Learning, 1976.

M. I. Baskes. Modified embedded-atom potentials for cubic materials and impurities. *Physical Review B*, 46(5):2727, 1992.

W. Bendick and W. Pepperhoff. On the α/γ phase stability of iron. *Acta Metallurgica*, 30(3):679–684, 1982.

J. D. Bernal and R. H. Fowler. A theory of water and ionic solution, with particular reference to hydrogen and hydroxyl ions. *J. Chemical Physics*, 1(8):515–548, 1933.

M. Born and R. Oppenheimer. Zur quantentheorie der molekeln. *Annalen der Physik*, 389(20):457–484, 1927.

E. E. Borrero and F. A. Escobedo. Simulating the kinetics and thermodynamics of transitions via forward flux/umbrella sampling. *The Journal of Physical Chemistry B*, 113(18):6434–6445, 2009.

G. B. Brook and E. A. Brandes. *Smithells Metals Reference Book*. Butterworth-Heinemann, 1983.

W. Cai. http://micro.stanford.edu/~caiwei/me346/, 2007.

H. B. Callen. *Thermodynamics & an Introduction to Thermostatistics*. John Wiley & Sons, 2006.

M. de Koning and A. Antonelli. Einstein crystal as a reference system in free-energy estimation using adiabatic switching. *Physical Review E*, 53(1):465, 1996.

M. de Koning and A. Antonelli. Adiabatic switching applied to realistic crystalline solids: Vacancy-formation free energy in copper. *Physical Review B*, 55(2):735, 1997.

M. de Koning, A. Antonelli, and S. Yip. Reversible scaling: Optimized free-energy determination using atomistic simulation techniques. *Journal of computer-aided materials design*, 6(2-3):349–353, 1999a.

M. de Koning, A. Antonelli, and S. Yip. Optimized free-energy evaluation using a single reversible-scaling simulation. *Physical Review Letters*, 83(20):3973–3977, 1999b.

M. de Koning, W. Cai, A. Antonelli, and S. Yip. Efficient free-energy calculations by the simulation of nonequilibrium processes. *Computing in Science & Engineering*, 2(3):88–96, 2000.

M. de Koning, A. Antonelli, and S. Yip. Single-simulation determination of phase boundaries: A dynamic clausius–clapeyron integration method. *The Journal of Chemical Physics*, 115:11025, 2001.

C. Dellago, P. G. Bolhuis, F. S. Csajka, and D. Chandler. Transition path sampling and the calculation of rate constants. *The Journal of Chemical Physics*, 108:1964, 1998.

C. Domb and M. S. Green. *Phase Transitions and Critical Phenomena*. Academic Press, London, 1972.

E. Fermi, J. Pasta, and S. Ulam. Studies of nonlinear problems. Technical report, I, Los Alamos Scientific Laboratory Report No. LA-1940, 1955.

R. P. Feynman. Forces in molecules. *Physical Review*, 56(4):340, 1939.

D. Frenkel. Simulations: the dark side. *The European Physical Journal Plus*, 128(1):1–21, 2013.

D. Frenkel and A. J. Ladd. New monte carlo method to compute the free energy of arbitrary solids. applicaton to the fcc and hcp phases of hard spheres. *Journal of Chemical Physics*, 1987.

D. Frenkel and B. Smit. *Understanding molecular simulation: from algorithms to applications*. Academic press, 2001.

N. J. Giordano. *Computational Physics*. Prentice Hall PTR, 1996.

H. Goldstein. *Classical mechanics*. Addison-Wesley Pub. Co., 1980.

H. Hasegawa and D. G. Pettifor. Microscopic theory of the temperature-pressure phase diagram of iron. *Physical Review Letters*, 50(2):130–133, 1983.

J. A. Hayward and J. R. Reimers. Unit cells for the simulation of hexagonal ice. *Journal of Chemical Physics*, 106(4):1518–1529, 1997.

P. Hohenberg and W. Kohn. Inhomogeneous electron gas. *Physical Review*, 136(3B):B864, 1964.

W. G. Hoover. Canonical dynamics: Equilibrium phase-space distributions. *Physical Review A*, 31(3): 1695, 1985.

W. Kohn, L. J. Sham, et al. *Self-consistent equations including exchange and correlation effects*. APS, 1965.

W. Krauth. *Statistical mechanics: algorithms and computations*, volume 13. OUP Oxford, 2006.

LAMMPS. http://lammps.sandia.gov/.

L. D. Landau. *Mechanics*. Butterworth-Heinemann, 1972.

W. Lechner and C. Dellago. Accurate determination of crystal structures based on averaged local bond order parameters. *The Journal of chemical physics*, 129:114707, 2008.

B.-J. Lee and M. I. Baskes. Second nearest-neighbor modified embedded-atom-method potential. *Physical Review B*, 62(13):8564, 2000.

T. Lee, M. I. Baskes, S. M. Valone, and J. D. Doll. Atomistic modeling of thermodynamic equilibrium and polymorphism of iron. *Journal of Physics: Condensed Matter*, 24(22):225404, 2012.

G. J. Martyna, M. L. Klein, and M. E. Tuckerman. Nosé–hoover chains: the canonical ensemble via continuous dynamics. *The Journal of Chemical Physics*, 97:2635, 1992.

G. J. Martyna, D. J. Tobias, and M. L. Klein. Constant pressure molecular dynamics algorithms. *The Journal of Chemical Physics*, 101:4177, 1994.

MD++. http://micro.stanford.edu/MDpp/.

R. Meyer and P. Entel. Martensite-austenite transition and phonon dispersion curves of fe_{1-x} ni_x studied by molecular-dynamics simulations. *Physical Review B*, 57(9):5140, 1998.

G. E. Moore et al. Cramming more components onto integrated circuits, 1965.

M. Müller, P. Erhart, and K. Albe. Analytic bond-order potential for bcc and fcc iron—comparison with established embedded-atom method potentials. *Journal of Physics: Condensed Matter*, 19(32):326220, 2007.

J. F. Nagle. Theory of the dielectric constant of ice. *Chemical Physics*, 43(3):317–328, 1979.

S. Nosé. A molecular dynamics method for simulations in the canonical ensemble. *Molecular Physics*, 52 (2):255–268, 1984.

L. Pauling. The structure and entropy of ice and of other crystals with some randomness of atomic arrangement. *Journal of the American Chemical Society*, 57(12):2680–2684, 1935.

V. F. Petrenko and R. W. Whitworth. *Physics of Ice*. Clarendon Press, 1999.

S. Plimpton et al. Fast parallel algorithms for short-range molecular dynamics. *Journal of Computational Physics*, 117(1):1–19, 1995.

J. M. Polson, E. Trizac, S. Pronk, and D. Frenkel. Finite-size corrections to the free energies of crystalline solids. *The Journal of Chemical Physics*, 112:5339, 2000.

D. A. Porter and K. E. Easterling. *Phase transformations in metals and alloys*. CRC PressI Llc, 1992.

W. H. Press, S. A. Teukolsky, W. T. Vetterling, and B. P. Flannery. *Numerical recipes 3rd edition: The art of scientific computing*. Cambridge university press, 2007.

L. Proville, D. Rodney, and M.-C. Marinica. Quantum effect on thermally activated glide of dislocations. *Nature Materials*, 2012.

A. Rahman. Correlations in the motion of atoms in liquid argon. *Physical Review*, 136(2A):405–411, 1964.

A. Rahman and F. H. Stillinger. Proton distribution in ice and the kirkwood correlation factor. *The Journal of Chemical Physics*, 57:4009, 1972.

J. Russo and H. Tanaka. The microscopic pathway to crystallization in supercooled liquids. *Scientific reports*, 2, 2012.

S. Ryu and W. Cai. Comparison of thermal properties predicted by interatomic potential models. *Modelling and Simulation in Materials Science and Engineering*, 16(8):085005, 2008.

S. Ryu and W. Cai. Validity of classical nucleation theory for ising models. *Physical Review E*, 81(3): 030601, 2010.

P. J. Steinhardt, D. R. Nelson, and M. Ronchetti. Bond-orientational order in liquids and glasses. *Physical Review B*, 28(2):784, 1983.

F. H. Stillinger and A. Rahman. Improved simulation of liquid water by molecular dynamics. *The Journal of Chemical Physics*, 60:1545, 1974.

A. Stukowski. Visualization and analysis of atomistic simulation data with ovito–the open visualization tool. *Modelling and Simulation in Materials Science and Engineering*, 18(1):015012, 2010.

B. Sutherland, C. N. Yang, and C. P. Yang. Exact solution of a model of two-dimensional ferroelectrics in an arbitrary external electric field. *Physical Review Letters*, 19(10):588, 1967.

P. R. ten Wolde, M. J. Ruiz-Montero, and D. Frenkel. Numerical calculation of the rate of crystal nucleation in a lennard-jones system at moderate undercooling. *The Journal of Chemical Physics*, 104: 9932, 1996.

C. G. Timothy and K. Kadau. Trillion-atom molecular dynamics becomes a reality. *International Journal of Modern Physics C*, 19(09):1315–1319, 2008.

M. Tuckerman, B. J. Berne, and G. J. Martyna. Reversible multiple time scale molecular dynamics. *The Journal of Chemical Physics*, 97(3):1990, 1992.

M. E. Tuckerman. *Statistical Mechanics: Theory and Molecular Simulation*. Oxford Graduate Texts, 2010.

C. Valeriani, R. J. Allen, M. J. Morelli, D. Frenkel, and P. R. ten Wolde. Computing stationary distributions in equilibrium and nonequilibrium systems with forward flux sampling. *The Journal of Chemical Physics*, 127:114109, 2007.

VASP. http://www.vasp.at/.

L. Verlet. Computer "experiments" on classical fluids. i. thermodynamical properties of lennard-jones molecules. *Physical Review*, 159(1):98, 1967.

Z.-J. Wang, C. Valeriani, and D. Frenkel. Homogeneous bubble nucleation driven by local hot spots: A molecular dynamics study. *The Journal of Physical Chemistry B*, 113(12):3776–3784, 2008.

M. Watanabe and W. P. Reinhardt. Direct dynamical calculation of entropy and free energy by adiabatic switching. *Physical Review Letters*, 65(26):3301–3304, 1990.

A. Yanagawa and J. F. Nagle. Calculations of correlation functions for two-dimensional square ice. *Chemical Physics*, 43(3):329–339, 1979.

S. Yip. Synergistic science. *Nature Materials*, 2(1):3–5, 2003.

N. J. Zabusky. Fermi–pasta–ulam, solitons and the fabric of nonlinear and computational science: History, synergetics, and visiometrics. *Chaos: An Interdisciplinary Journal of Nonlinear Science*, 15(1):015102–015102, 2005.

N. J. Zabusky and M. D. Kruskal. Interaction of "solitons" in a collisionless plasma and the recurrence of initial states. *Physical Review Letters*, 15(6):240–243, 1965.